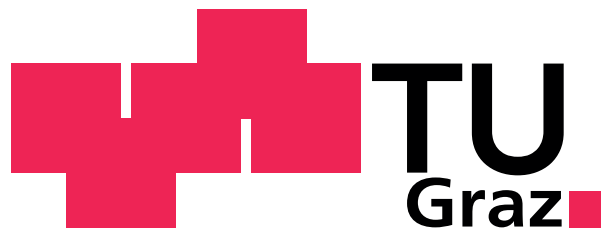


Stefan Spann

Structural connectivity in the human brain: Analysis of network measures

Master Thesis



Institute of Medical Engineering
Technical University of Graz Kronesgasse 5/II
A-8010 Graz

Head of the Institute: Univ.-Prof. Dr.techn. Dipl.-Ing. Rudolf Stollberger

Adviser: Dipl.-Ing. Dr.techn. Christian Langkammer
Reviewer: Univ.-Prof. Dr.techn. Dipl.-Ing. Rudolf Stollberger

Graz, (15th June 2015)

Contents

1. Introduction	1
2. Background	4
2.1. Diffusion weighted MRI	4
2.1.1. Introduction	4
2.1.2. Diffusion	4
2.1.3. Diffusion weighted MRI	6
2.1.4. Diffusion Tensor	8
2.1.5. Orientation Distribution Function - ODF	9
2.2. Main white matter pathways in the human brain	11
2.2.1. Association fibers	11
2.2.1.1. Long Association fiber: Superior Longitudinal Fasciculus (SLF)	12
2.2.1.2. Long Association fiber: Uncinate Fasciculus (UF)	12
2.2.1.3. Long Association fiber: Inferior Fronto-occipital Fasciculus (IFOF)	12
2.2.1.4. Long Association fiber: Inferior Longitudinal Fasciculus (ILF)	13
2.2.1.5. Long Association fiber: Middle Longitudinal Fasciculus (ML)	13
2.2.1.6. Short Association fibers	13
2.2.2. Projection fibers	14
2.2.2.1. Fornix	14
2.2.2.2. Mammillo-thalamic tract	14
2.2.3. Commissural fibers	15
2.2.3.1. Corpus Callosum	15
2.3. Structural Connectome	15
2.3.1. Creating the structural human Connectome with Diffusion MRI	16
2.3.2. Overview of existing Structural Connectome pipelines	18
3. Materials and Methods	19
3.1. Data acquisition	19
3.2. Creating the structural Connectome	19
3.3. Morphological Stream	21
3.3.1. Segmentation	21
3.3.2. Parcellation	26
3.3.3. Registration	27
3.4. Diffusion Stage	29
3.4.1. Preprocessing	29
3.4.1.1. Motion correction	29

3.4.1.2.	Eddy current correction	30
3.4.2.	Estimation of the diffusion direction in each voxel	31
3.4.2.1.	Estimation of the diffusion tensor	31
3.4.2.2.	Estimating the fiber orientation distribution function	33
3.4.3.	White matter tractography	38
3.4.3.1.	Fiber Assignment by Continuous Tracking	39
3.4.3.2.	Streamline Propagation using Euler's method	40
3.4.3.3.	Streamline Propagation using Newton-Raphson method	42
3.4.4.	Tractography Postprocessing and Parameters	44
3.5.	Connectome Stage	44
3.6.	Connectome Comparison	45
3.6.1.	Pearson Correlation	45
3.6.2.	Network measures of brain connectivity	46
3.6.3.	Weighted average node degree	46
3.6.4.	Weighted characteristic path length	47
3.6.5.	Weighted global efficiency	48
3.6.6.	Network density	48
3.7.	Evaluation of the structural connectivity matrix	49
4.	Results and Discussion	51
4.1.	Pipeline Results	51
4.1.1.	Results of the morphological Stream	51
4.1.2.	Results of the Diffusion Stream	53
4.1.3.	Results of the Connectome Stream	54
4.2.	Streamline Statistics	56
4.3.	Network Measures	59
4.3.1.	Network Density	59
4.3.2.	Nodal Degree	68
4.3.3.	Characteristic Path Length	72
4.3.4.	Global Efficiency	76
4.4.	Robustness	79
4.4.1.	Intra-subject variability	79
4.4.1.1.	Same scans processed twice	79
4.4.1.2.	Same subject scanned twice	82
4.4.2.	Inter-subject variability	84
4.5.	Anatomic Validation	88
4.5.1.	Valid anatomic connections	89
4.5.2.	False positive connections	93
5.	Conclusion	98
	Appendices	107

**A. White matter pathways and the corresponding cortical areas in
Freesurfer 107**

Statutory Declaration

I declare that I have authored this thesis independently, that I have not used other than the declared sources / resources, and that I have explicitly marked all material which has been quoted either literally or by content from the used sources.

Eidesstattliche Erklärung

Ich erkläre an Eides statt, dass ich die vorliegende Arbeit selbstständig verfasst, andere als die angegebenen Quellen/Hilfsmittel nicht benutzt und die den benutzten Quellen wörtlich und inhaltlich entnommene Stellen als solche kenntlich gemacht habe.

Ort

Datum

Unterschrift

Acknowledgements

“To my beloved mother and father, for creating my genome and molding my connectome”[67]

First of all, I would like to thank my parents, Gabriele and Helmut, who have always supported me throughout my life and opened the door for me to study. I also want to thank my older sister Claudia, who has also always supported me, and especially for the support during writing and thanks to my younger sister Julia for clearing my mind when everything got on top of me.

Special thanks to my student colleagues and good friends Aspi, Isi and Sölli, with whom it has been a pleasure to study together.

Furthermore I would like to thank my friends Carina, Gege, Obi and Pete, for always having an open ear for me in difficult and stressful times.

Special thanks to my adviser Christian, who introduced me to the exciting topic Connectomics and has supported me during my thesis. Thank you also for the inspirational conversations.

I would like to thank Professor Stollberger, for enabling me to do the thesis at the Neuroimaging Research Unit in Graz and for taking the time to read this thesis and providing useful suggestions.

Abstract

The brain is the most complex system in the human body and understanding its function and structure is of high scientific interest as reflected by several ongoing multinational scientific efforts. “Connectomics”, based on diffusion MRI, assesses the structure of the brain as a network graph and provides new insights of the topological organisation of healthy and pathological brains. However, network reconstruction involves several steps, such as segmentation, parcellation, registration, fiber orientation estimation, and fiber tracing - all of them with a high degree of parametrization. This thesis investigated the impact of different combinations of state-of-the-art tractography algorithms, diffusion weighted acquisition and parcellation schemes on structural connectivity and derived network measures. Additionally, the intra- and inter-subject variability was tested and the meaningfulness of the structural connectivity map validated by 8 major white matter bundles. This work showed that at least 100,000 fibers have to be generated to obtain a connected structural connectivity network which is reliable for further analysis. A high intra-subject but a moderate inter-subject reproducibility was found and group-wise studies are only meaningful with parcellation scales of 83 and 129 brain regions. In general, the selection of the number of nodes had the most substantial impact on the network measures, but also the tracing algorithm. In conclusion, measures of structural connectivity are highly dependent on acquisition and processing and therefore not comparable between studies.

High-resolution diffusion MRI in combination with a probabilistic multi fiber orientation model yields most connections but comes at the cost of increased scan as well as calculation time.

In contrast, conventional DTI acquisition with FACT fiber tracing is fast and has the least false positive connections, which is preferable for clinical structural connectivity studies.

Kurzfassung

Das Gehirn ist das komplexeste System im menschlichen Körper und das Verständnis über seine Funktion und Struktur ist von großem wissenschaftlichen Interesse, was auch durch verschiedene laufende multinationale wissenschaftliche Versuche verdeutlicht wird. “Connectomics”, basierend auf Diffusions-MRI, beschreibt die Struktur des Gehirns als einen Netzwerkgraphen und liefert somit neue Einblicke in die topologische Organisation von gesunden und pathologischen Gehirnen. In die Rekonstruktion eines Netzwerks sind jedoch zahlreiche Schritte involviert wie Segmentierung, Parzellierung, Registrierung, Schätzung der Faserrichtungen und “Fiber-Tracking” - allesamt mit einem hohen Grad der Parametrisierung. In dieser Arbeit wurden die Einflüsse verschiedener Kombinationen von state-of-the-art Tractographie-Algorithmen, diffusionsgewichteten Datenakquirierungen und Parzellierungsschemata auf die strukturelle Konnektivität und die daraus abgeleiteten Netzwerkmaße untersucht. Zusätzlich wurde die intersubjektive und intrasubjektive Variabilität getestet und die Sinnhaftigkeit der strukturellen Konnektivitätskarten anhand von 8 bekannten Faserbündeln validiert. Diese Arbeit zeigte, dass mindestens 100 000 Fasern rekonstruiert werden müssen, um ein vollständig verbundenes strukturelles Netzwerk zu erhalten, welches Voraussetzung für weitere Analysen ist. Eine hohe intrasubjektive und eine moderate intersubjektive Reproduzierbarkeit wurde festgestellt und es zeigte sich, dass Gruppenstudien nur mit einer Parzellierungsskalierung von 83 oder 128 Hirnarealen sinnvoll sind. Im Allgemeinen hat die Anzahl der Knoten den wesentlichsten Einfluss auf die Netzwerkmaße, aber auch der Tractographie-Algorithmus beeinflusst diese. Abschließend kann gesagt werden, dass die Maße der strukturellen Konnektivität sehr stark vom Akquirierungsschema und von der Verarbeitung abhängen und daher ein Vergleich zwischen einzelnen Studien nicht möglich ist. Die hochauflösten Diffusions-MRIs in Kombination mit probabilistischen Mehrfaser-Orientierungsmodellen führten zu den meisten Verbindungen, sie

gehen jedoch mit einer Erhöhung der Scanzeit sowie der Berechnungszeit einher. Im Gegensatz dazu ist die gewöhnliche DTI-Datenakquirierung in Kombination mit dem FACT-Fiber Tracking Algorithmus sehr schnell und weist zudem die geringste Anzahl an falsch positiven Verbindungen auf. Daher ist diese für klinische Studien vorzuziehen.

1. Introduction

The brain is the most complex organ in the human body. It contains more than 100 billion neurons linked together with about 10^{15} connections. It is like a majestic forest in which no road, no trail can penetrate and no sunbeam can find a path through it [67]. It is not surprising that scientists designate the brain not only as the most complex organ, they designate it as the most complex object in the universe. Astonishing that this majestic forest fits in a container with a capacity less than one and a half litre and even more astonishing that this forest makes us what we are: how we think, how we behave and how we act. At present, the function of the human brain as well as the organisation of the white matter bundles (connections) is poorly understood. The main knowledge of neuronal connections is based on post-mortem fiber dissection studies. In 2005 Patrick Hagmann and Olaf Sporns had the idea to describe the complex human brain as a network with nodes and edges and considered this as Connectome [59][57]. A new research area was born, Connectomics. This research area opened new doors to gain new insights in the organisation, structure and function of the brain as well as to understand and early detect diseases of the nervous system such as amyotrophic lateral sclerosis (ALS) or multiple sclerosis (MS). Since then, several research projects have been founded all over the world like “Developing Human Connectome Project (DHCP)” in Europe or “Human Connectome Project” in America.

In the course of these projects three different approaches were established for describing the human brain as a network. In the first approach, the functional connectivity, the activity of the brain is mapped to detect functional clusters. This is done with EEG or functional MRI. The second approach, the molecular connectivity, maps the molecular connection between neurons. Mapping the structural connectivity is the third approach. This method maps the structural white matter pathways connecting the different cortical areas of the brain. A link established by these three approaches will enable a increased understanding of the function of the human brain.

In the last approach, also known as structural Connectome, diffusion weighted MRI has become increasingly important. At present, this technology is the only one allowing the in-vivo study of structural neuronal connections in the human brain. The whole process for mapping the structural connectivity is complex. A T1w MRI is necessary for parcellation of the brain in known anatomical areas, which serve as nodes in the network. Furthermore dwMRI is necessary for reconstructing the white matter bundles, which serve as edges in the graph and connect the segmented cortical areas. One fundamental problem is that a gold standard in the neuroscience community for mapping the structural connectome is missing. For each single processing step several different approaches exist. Different combinations of these methods influence the accuracy of the resulting structural connectome. Several works investigate these influences. For instance, the effects of gray matter parcellation [1], tractography algorithm [49] and reproducibility of the structural connectome itself [58] and corresponding network measures [58][25] were investigated. However, most of the studies found in literature investigate the impacts on thresholded or binarized structural connectivity matrices. At present it is not clear which connections in the generated structural connectivity matrix do also exist in the human brain and which are artificial generated from the used methods. Therefore, in contrast to previous studies the connectivity matrices in this thesis are not thresholded or binarized. The aim of this thesis is to investigate the impact of every step on the raw connectivity matrices as well as on the corresponding network measures. Therefore, four questions will be answered. (1) How do different acquisition schemes influence the structural connectivity and network measures? (2) How does the number of nodes influence the results of structural connectivity? (3) Has the fiber tracing algorithm and the number of reconstructed fibers an impact on the structural connectivity and on network measures? (4) Which combinations of the used methods are most robust and reproducible?

In order to answer these questions different MRI datasets from two healthy subjects regarding spatial resolution, number of gradient directions and different b-values are acquired. The influence of number of nodes on network measures is investigated using 5 different scales from 83 up to 1015 brain regions (LOUSANNE - atlas). Three different tractography algorithms (fiber assignment by continuous tracing [65], euler's method [15] and a deterministic approach based on constrained spherical deconvolution [34]) are used for evaluation and the number of reconstructed fibers are changed from 25 000 up to 650 000. The intra-subject as well as the inter-subject variability is tested for all different combinations to analyse the robustness and variability. In a last step the information

differences contained in the resulting structural connectivity matrices are evaluated for 8 well known white matter pathways using a manually defined structural connectivity matrix.

2. Background

2.1. Diffusion weighted MRI

2.1.1. Introduction

Diffusion weighted MRI is a magnetic resonance imaging technique that provides macroscopic information of water diffusion in tissue. This imaging technique is based on the quantification of the arbitrary motion of water molecules. The measured water diffusion contains information of axonal orientation and local microstructures of the tissue. This information can be voxelwise reconstructed using methods such as diffusion tensor or constrained spherical deconvolution. Following the main orientations of the axonal orientations from one voxel to the other an axon bundle, also called fiber tract, can be reconstructed. These fiber tracts are represented as trajectories and make it possible to study white matter pathways and the structural connectivity of the human brain.

2.1.2. Diffusion

In diffusion weighted MRI the intrinsic diffusion of water is measured. The diffusion of each water molecule is driven by thermal fluctuations of the substance of interest and follows a random walk (figure 1). This process is known as Brownian motion [30].

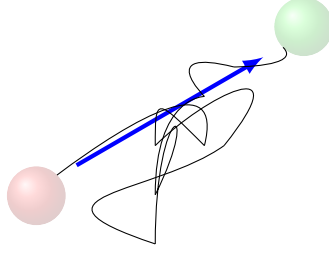


Figure 1: Brownian motion of a single water molecule. The black line illustrates the random walk of the molecule from the red to the green location. The blue arrow illustrates the mean displacement.

A mathematical description of the Brownian motion was derived by Albert Einstein in 1905. He found out that particles always cover the same mean squared displacement in a given time period and asserted this as the basic quantity (equation 1) [60].

$$D = \frac{\langle \Delta r^2 \rangle}{2n\Delta t} \quad (1)$$

where D is the diffusion coefficient, n is the number of dimensions, $\langle \Delta r^2 \rangle$ is the mean squared displacement and Δt the diffusion time.

Several years later Jean Perrin verified Einstein's relation and additionally he figured out that the particle displacement exactly followed random laws. On this account the statistical distribution of particle displacement in one direction can be described by a Gaussian distribution [60].

$$P(\Delta r, \Delta t) = \frac{1}{\sqrt{(2\pi D\Delta t)^3}} \exp\left(\frac{-\Delta r^2}{4D\Delta t}\right) \quad (2)$$

where Δt is the diffusion time, Δr is the particle displacement and D is a diffusion coefficient.

As previously described, the reasons for diffusion of water molecules are thermal fluctuation in the substance of interest. A constant random motion of molecules in all directions is known as isotropic diffusion. This is, for example, the case for water molecules in regions of the cerebral spinal fluid (CSF).

In white matter myelinated axons highly hinder the diffusion of water molecules in the perpendicular direction whereas it is nearly free in the parallel direction. In this case the water molecule has a preferred diffusion direction which is parallel to the myelinated

axons. This is known as anisotropic diffusion and quantitatively characterized by the apparent diffusion coefficient ADC. In diffusion MRI the ADC is measured in the human brain to characterize the structure and orientation of the axon bundles [21][2].

2.1.3. Diffusion weighted MRI

The most common utilized diffusion weighted MRI sequence is the Stejskal-Tanner sequence (figure 2).

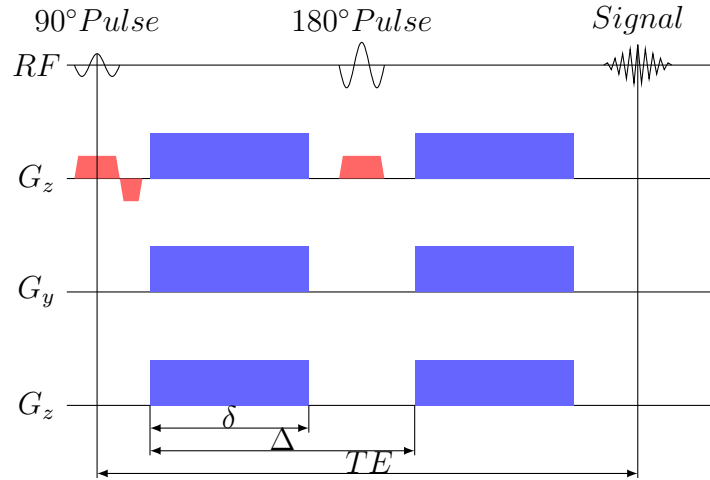


Figure 2: Stejskal Tanner sequence

The idea behind this sequence is to control the diffusion weighting by using two gradient pulses (blue gradients in figure 2). Along an applied gradient, spins precess with different frequencies. This leads to a local phase shift of all spins and therefore to a dephasing of the magnetization across the sample. The local phase shift is inverted by the 180° RF-pulse. A second gradient pulse inverts this local phase shift and the magnetization in the sample rephases. In stationary spins the induced phase shift cancels out completely and no signal attenuation occurs. In case of diffusion, the spins change their location owing to Brownian motion. As a result of this location change, the spins experience different gradient strengths. This leads to a different phase shift and the spins in the sample do not rephase completely and cause a signal attenuation [2] [10]. In an isotropic environment the signal attenuation due to diffusion can be described by

$$S = S_0 e^{-bD} \quad (3)$$

where S_0 is the signal of the baseline image acquired without diffusion sensitizing gradient, D is the constant diffusion coefficient and b is the diffusion weighting factor.

The diffusion weighting factor allows to control the signal attenuation. A larger diffusion weighting factor leads to a higher signal attenuation and therefore a larger diffusion weighting. This coefficient depends on several factors and will be modified for different DWI images:

$$b = \gamma^2 \delta^2 G^2 \left(\Delta - \frac{\delta}{3} \right) \quad (4)$$

where γ is the gyromagnetic ratio ($42,576 \text{ MHz T}^{-1}$ for protons), G is the magnitude of the diffusion gradient, Δ is the time difference between the two diffusion sensitizing gradient pulses and δ is the duration of the diffusion sensitizing gradient pulses [10].

In case of anisotropic diffusion the diffusion coefficient has to be replaced by the apparent diffusion coefficient \mathbf{D} and therefore equation 3 has to be re-written [42].

$$S = S_0 e^{-b\mathbf{g}^T \mathbf{D} \mathbf{g}} \quad (5)$$

where \mathbf{g} is the normalized diffusion sensitizing gradient vector.

2.1.4. Diffusion Tensor

The diffusion tensor \mathbf{D} is a common method for describing the local Gaussian water diffusion in three dimensions. It is a 3x3 symmetrical ($D_{ij} = D_{ji}$) covariance matrix (equation 6). The diagonal terms of the diffusion tensor describe the diffusion variances along the physical axes x,y,z and the off-diagonal terms the covariances. The physical axes are defined by the orientation of the MRI scanner [55].

$$\mathbf{D} = \begin{bmatrix} D_{xx} & D_{xy} & D_{xz} \\ D_{yx} & D_{yy} & D_{yz} \\ D_{zx} & D_{zy} & D_{zz} \end{bmatrix} \quad (6)$$

The direction of the water diffusion in a voxel can be determined by calculating the eigenvectors (e_1, e_2, e_3) of the diffusion tensor. The eigenvalues ($\lambda_1, \lambda_2, \lambda_3$) of \mathbf{D} describe the strength of the diffusion in the direction of the corresponding eigenvector [2].

The CSF of the human brain is an isotropic environment and therefore the diffusion of water molecules is free in all directions. In this case the diffusion is equal in all directions and the diffusion tensor \mathbf{D} consists of only diagonal terms with equal magnitude ($\lambda_1 = \lambda_2 = \lambda_3$). The diffusion ellipsoid is spherically shaped with a diameter of size D (figure 3(a)).

The white matter of the human brain is a highly anisotropic environment. Thus, water molecules diffuse in a preferred orientation, described by the major eigenvector of the diffusion tensor. In this case the diffusion ellipsoid is elliptically shaped and the diffusion tensor consists of nine non zero elements (figure 3(c)). The direction of the eigenvectors can be aligned with the physical axes x,y,z using a rotation matrix and therefore the diffusion tensor has only diagonal elements which are the eigenvalues (figure 3(b)) [55].

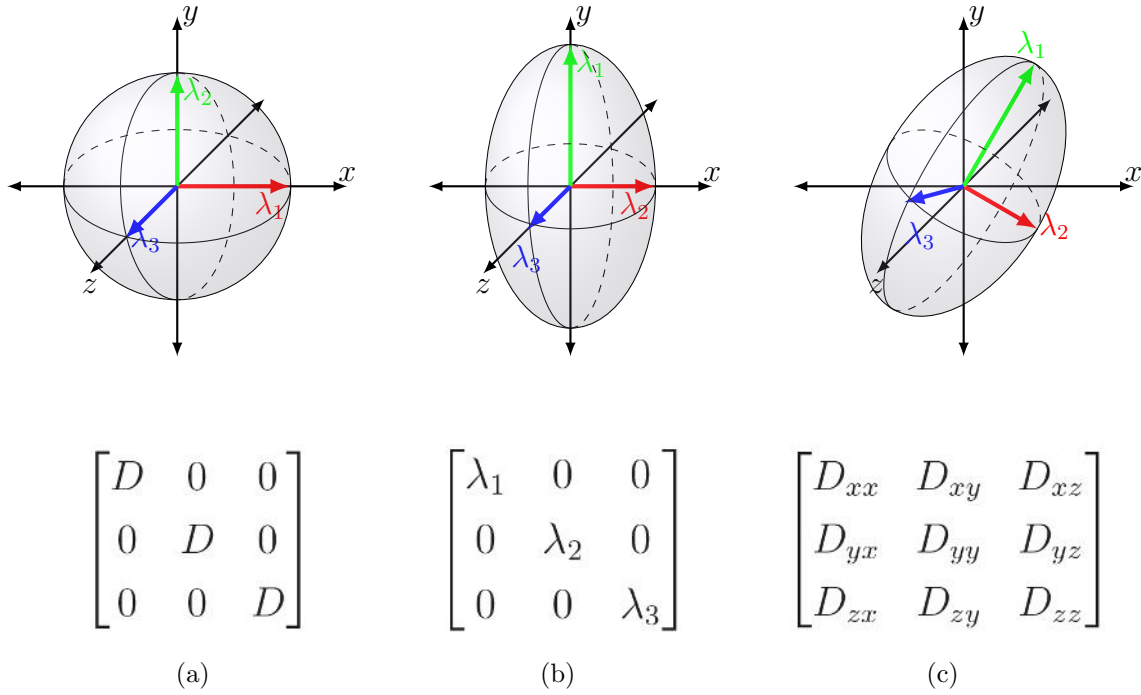


Figure 3: Relationship between diffusion ellipsoid and Diffusion Tensor in case of isotropic (a) and anisotropic (b) (c) environment.

2.1.5. Orientation Distribution Function - ODF

The previously described diffusion tensor model estimates the orientation of axons very well if they are aligned homogeneously within a voxel. A recent study show that more than 90% of the measured voxels in the human brain contain kissing, crossing or merging fibers [39]. This leads to heterogeneities which are not accounted by the simple diffusion tensor model. The diffusion tensor approach leads to inadequate and unreliable fiber orientation estimation (figure 4) [39][16]. Therefore, more complex models such as the Orientation Distribution Function are necessary. This is a probabilistic model which describes the orientation of fibers present in a voxel with a continuous function of the unit sphere, the so-called fiber orientation distribution function (ODF). More precisely, the ODF, mathematically represented as $F(\theta, \phi)$ in spherical coordinates, contains two types of information. First the orientation (θ, ϕ) of the fibers within a voxel and second the corresponding volume fraction. The volume fraction indicates the number of fibers aligned with the distinct orientation of the fibers related to the maximum number of fibers within a voxel. For the case that two orientational fiber populations are present within a voxel (figure 4(g)) the ODF is simply the sum of two dirac delta functions aligned

with the distinct fiber orientation (θ, ϕ) and weighted with the volume fraction. The ODF is typically represented in the basis of spherical harmonics (the reader is referred to section 3.4.2.2 for further details on Spherical Harmonics (SH) and calculating the ODF) [40][36].

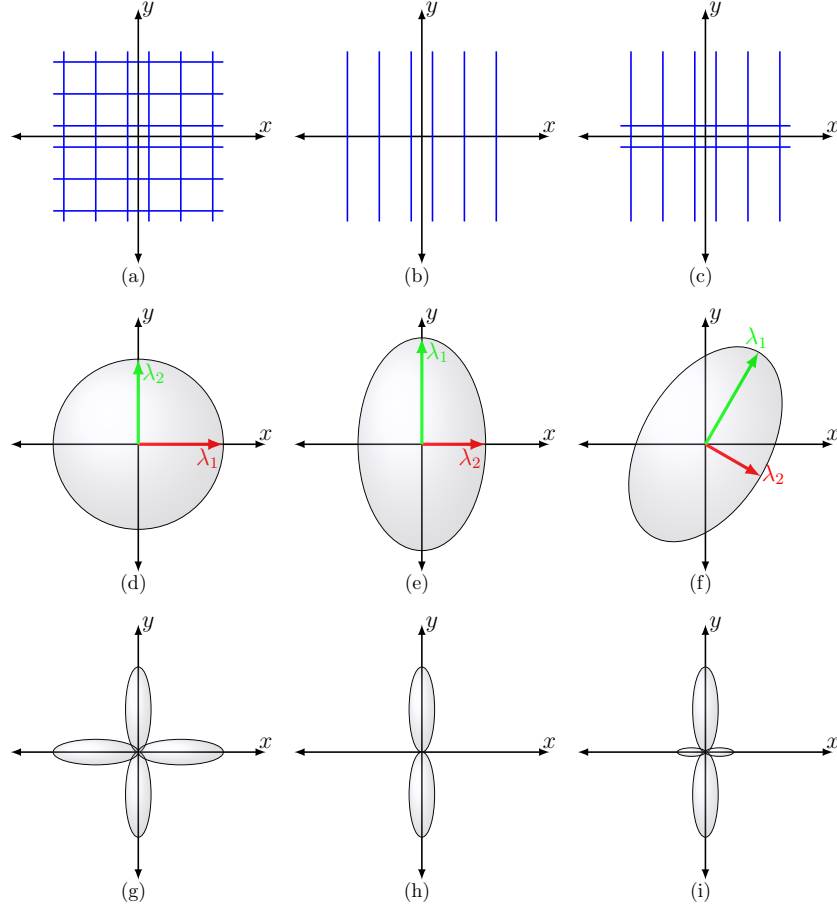


Figure 4: DTI compared to ODF within a voxel. Figures (a) to (c) show the original fibers within the voxel. Figures (d) to (f) illustrate the estimated diffusion tensor and figures (g) to (i) show the fiber orientation distribution function. Only in figure (e) the diffusion tensor describes the underlying fiber direction correctly whereas the ODF estimates the true fiber direction correctly. In figure (h) the volume fraction is identical whereas in figure (g) the volume fraction is $1/4$ in x direction $F_1(\theta_1, \phi_1)$ and $3/4$ in y direction $F_2(\theta_2, \phi_2)$ resulting in an ODF $F(\theta, \phi) = 1/4F_1(\theta_1, \phi_1) + 3/4F_2(\theta_2, \phi_2)$.

2.2. Main white matter pathways in the human brain

About 50% of the human brain consist of white matter and is underlying the outer cortex of gray matter (see figure 5) and consists mainly of myelinated axons bundled into fascicles or fiber tracts [5]. The fascicles form a complex network linking different areas of the cerebral matter allowing to carry nerve impulses between neurons of this region for communication [53].

The white matter pathways or fascicles are classified into association, projection and commissural fibers (figure 5) [13]. The important fascicles of each category and their corresponding cortical connections are described in the following subsection. On the basis of this fascicles the generated connectivity matrices in section4 are evaluated.

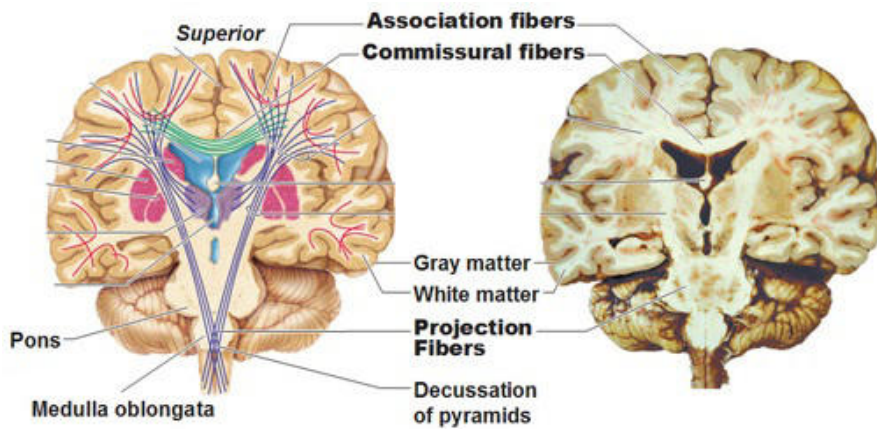


Figure 5: Frontal section of the human brain and the three types of fiber bundles: Association fibers (red), commissural fibers (green) and projection fibers (blue). Modified image taken from[5].

2.2.1. Association fibers

Fascicles or fiber bundles connecting cortical areas of the same cerebral hemisphere are referred to as association fibers. Two different kinds of association fibers exist: The long association fibers and the short association fibers. The first type connects different lobes within the same hemisphere while the latter one connects the adjacent gyri. This type of fiber is the most numerous in the human brain [13].

2.2.1.1. Long Association fiber: Superior Longitudinal Fasciculus (SLF)

The Superior Longitudinal Fasciculus is a lateral white matter fiber tract consisting of short and long fiber bundles. The SLF connects regions in the frontal lobe with parietal, occipital and temporal lobes and is present in the right and left hemisphere. The SLF is subdivided into three major fiber tracts [13][53][12]

- Long direct fiber tract - Arcuate Fasciculus (AF)
- Anterior indirect fiber tract - Horizontal segment of the SLF
- Posterior indirect fiber tract - Vertical segment of the SLF

The AF of the left hemisphere plays a major role in language processing and is additionally involved in verbal working memory. The AF in the right hemisphere is included in the aspect of language semantic and in visuospatial processing [12].

The cortical areas connected by the three major fiber tracts of the AF are listed in table 5 in Appendix A. The AF is very heterogeneous and shows an extreme left lateralization whereby in most human brains the AF in the right hemisphere connects only the caudal middle frontal gyrus with the middle temporal gyrus. Damages in the AF can cause different types of aphasia [54][29][13].

2.2.1.2. Long Association fiber: Uncinate Fasciculus (UF)

The Uncinate Fasciculus is a bidirectional, ventral associative white matter tract that connects cortical regions of the frontal cortex with the anterior temporal lobe [53]. The UF is typically considered to be part of the extended limbic system. The exact function of the UF is unknown but previous studies [14][26] have indicated that it is involved in language, emotion and memory processing [13]. The cortical areas connected by the UF are summarized in table 6 in Appendix A [53].

2.2.1.3. Long Association fiber: Inferior Fronto-occipital Fasciculus (IFOF)

The Inferior Fronto-occipital Fasciculus is a long ventral associative white matter tract connecting posterolateral temporal, occipital and parietal lobes to the frontal lobe [52]. A recent study identified two layers of the IFOF by combining DTI tractography with

fiber dissection. The first layer terminates in the inferior frontal gyrus and is superficial and anterosuperiorly directed. The second one is the deep and ventral layer and is further subdivided into three parts [68]:

- posterior component
- middle component
- anterior component

The cortical regions connected by the two layers of the IFOF [68][52] are listed in table 7 in Appendix A. Recent studies suggest that the IFOF plays a role in the semantic system [52] in reading, visual processing and attention [64].

2.2.1.4. Long Association fiber: Inferior Longitudinal Fasciculus (ILF)

The Inferior Longitudinal Fasciculus is a white matter fiber bundle and connects the occipital regions with the anterior part of the temporal regions. The ILS can be subdivided into three segments, a dorsal component, a ventral component and a direct Li-Am component. The cortical place of origin and the cortical termination areas of these three subcomponents are summarized in table 8 in Appendix A. The ILF is involved in visual recognition and semantic language processing [28].

2.2.1.5. Long Association fiber: Middle Longitudinal Fasciculus (ML)

The Middle Longitudinal Fasciculus is a mid-size associated white matter fiber bundle that passes through the entire superior temporal lobe and the inferior parietal lobe [56]. The ML originates in the temporal pole of the superior temporal gyrus and terminates in the angular gyrus of the inferior parietal lobe [22]. The connected cortical areas are listed in table 11 in Appendix A. The function of the ML is rather moderately understood but recent studies suggest that the MF could play a role in functions as language and attention [22][56].

2.2.1.6. Short Association fibers

Short association fibers are also referred to as U-fibers. They lie directly beneath the gray

matter and connect two adjacent gyri. Today little is known about the exact anatomic location, the number and also the function of these fibers but it is known that humans with leukodystrophie have less U-fibers than healthy people. A list of known U-fibers can be found in table 9 in Appendix A [74] [11].

2.2.2. Projection fibers

The projection fibers run vertically within the white matter and connect the cortex with the brainstem and spinal cord structures for transferring sensory and motor information [9]. They are classified into two categories: corticofugal or efferent projection fibers and corticopedal or afferent projection fibers. Corticofugal fibers carry nerve pulses from the cortex to the basal nuclei, brainstem and spinal cord while corticopedal fibers carry pulses from the thalamus to the cortex [75].

2.2.2.1. Fornix

The Fornix is a projection white matter fiber tract connecting the hippocampus with the anterior thalamic nucleus, the mammillary body and the hypothalamus. The afferent fibers of the fornix arise in the septal and hypothalamic nuclei and terminate in the hippocampus. Table 10 in Appendix A lists the cortical structures connected by the Fornix. The Fornix is part of the limbic system and appears to be necessary in memory function [50][13].

2.2.2.2. Mammillo-thalamic tract

The Mammillo-thalamic tract is a short white matter tract that connects the mammillary bodies with the anterior and dorsal nuclei of the thalamus. The Mammillo-thalamic tract belongs to the limbic system. The Mammillo-thalamic tract forms, together with other fibers of the medial forebrain bundle, a circuit between the hypothalamus and limbic structures of the midbrain. This important circuit connects visceral perceptions to emotion [50].

2.2.3. Commissural fibers

Commissural fibers run horizontally within the white matter crossing the midline and connecting two corresponding cortical regions of the human brain. This type of fiber is necessary for communication and information transport between the two hemispheres. The main part of the commissural fibers is the corpus callosum [75] [9].

2.2.3.1. Corpus Callosum

The Corpus Callosum is the most important commissure fiber tract. It is the largest white matter bundle of the human brain consisting of about 250 million axons. The Corpus Callosum is generally divided into four parts: rostrum, genu, body and splenium and connects the corresponding cortical areas of the left and right cerebral hemispheres (table 12 [74] in Appendix A). It allows transferring motor, sensory, and cognitive information between the two hemispheres [13].

2.3. Structural Connectome

Patric Hagmann[59] and Olaf Sporns[57] simultaneously and independently of one another introduced the term connectome in 2005 for describing the brain connectivity. They were the first to describe the structure of the brain by a comprehensive map. The nodes of this map represent the cortical areas of the human brain and the edges represent the white matter pathways which connect the neurons of the different cortical areas. An example comprehensive map is shown in figure 6(a). The term connectome is often referred to as the wiring diagram of our brain. Over the past few years various technologies were developed for mapping the connectome. Electron or light microscopy are used for mapping cellular connectivity at the microscopic scale. With this technology it was possible to map the first full structural connectome of the roundworm *C. elegans*, which consists of 300 neurons and is illustrated in figure 6(b) [41][48]. These 300 neurons are, compared to the 100 billion neurons in the human brain, manageable to map. New high-throughput serial electron microscopes (ATUM) were developed, which provides the opportunity to map 30nm slides of the human brain [45]. These new technologies open a new era in mapping the first full human structural connectome. With this era new challenges come such as saving and processing the amount of data (1 Petabyte for $1mm^3$ brain tissue) [72].

matter, gray matter and the CSF (2). In a third processing step (3a) the segmented cortical surface from step (2) is subdivided into well-known anatomical parcels which serve as nodes for the structural connectome. These anatomical parcels are further subdivided into smaller non-anatomical ROIs for high resolution connectomes(3b). In a fourth step a model (e.g. diffusion tensor) is estimated for each voxel of the raw dwMRI representing the main diffusion direction. Subsequently, whole brain tractography is applied, using the information of the fitted diffusion model, to reconstruct the white matter bundles. The white matter mask segmented in step (2) serves as seed point mask. In the last step (5) the anatomical parcels (3a,3b) are registered on the diffusion space. After successful registration the defined ROIs (3a,3b) are combined with the tractography results (4) to compute the connection weight between each pair of ROIs. The result is a structural connectivity matrix of the whole brain [32]. The first three steps form the morphological stream, step 4 the diffusion stream and step 5 the connectome stage. For a detailed description of these 5 steps the reader is referred to section 3 of this thesis.

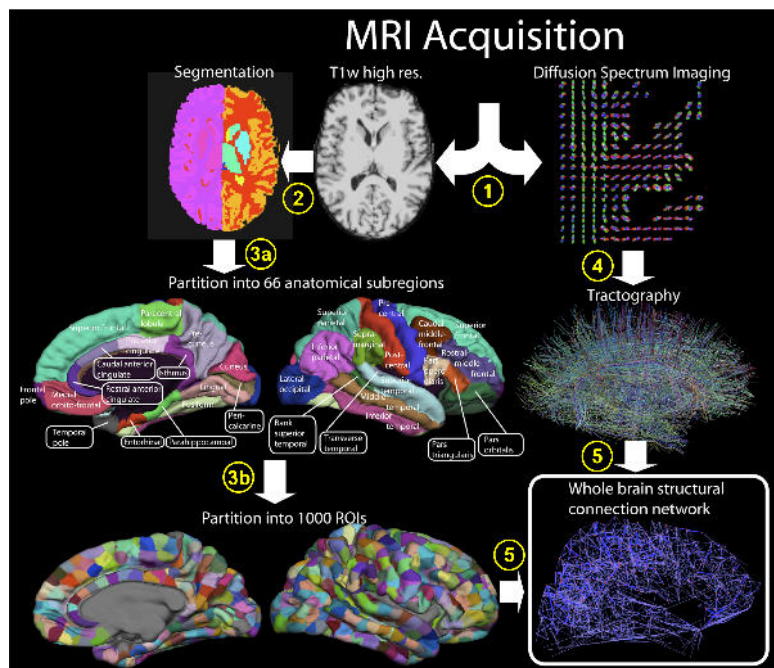


Figure 7: Flowchart of extracting the human structural connectome taken from [32]. (1) T1w and dwMRI acquiring; (2) Whole brain segmentation; (3) Parcellation of the brain in 66 anatomical ROIs (3a) and 998 non-anatomical ROIs (3b); (4) Whole brain tractography; (5) Combining results (3a,3b) and (4) for computing the structural connectome of the entire brain

2.3.2. Overview of existing Structural Connectome pipelines

Since the introduction of the term Connectome by Patric Hagmann and Olaf Sporn, a lot of research has been done in this field to improve mapping of the structural brain connectivity. This leads to an increase of new reconstruction algorithms for each individual processing step. However, each of these algorithms has its own advantages and disadvantages and was usually developed for a particular case. Therefore, using the same raw dataset but a different algorithm leads to different results, which makes it hard to compare results of their studies with equivalent studies of other research groups. On this account several pipelines were developed to standardize the workflow and make results from different research projects more comparable. At present four connectome mapping pipelines are available: Connectome Mapping Toolkit (CMTK ¹) [19], A pipeline toolbox for analyzing brain diffusion images (PANDA ²) [17], MR Connectome Automated Pipeline (MRCAP ³) [31], MRI Graph Reliability Analysis and Inference for Connectomics (MIGRAINE ⁴) [62]. These pipelines combine the most state of the art processing tools for creating the structural connectome. An overview of the general requirements of these pipelines is summarized in table 1.

Table 1: Overview of general information of the available structural connectivity pipelines

General Information	CMTK	PANDA	MRCAP	MIGRAINE
Software	Open Source	Open Source	Open Source	Open Source
Program language	Python	Matlab	JAVA	JAVA,Python
Operating system	Linux 32bit & 64bit	Linux 32bit & 64bit, MAC	Windows, MAC, Linux	Windows, MAC, Linux
Input Data Format	DICOM & NIFTI	DICOM & NIFTI	NIFTI	NIFTI
Parallel Computing	YES	YES	YES	YES
Underlying Framework	LONI,NIPYPE	PSOM	JIST, MIPAV	JIST, LONI
Computation Time	≥12h	≥12h	≥8h	≥12h
Support	Online discussion forum, active support community	Online discussion forum, mailing list and technical support by the developer	e-mail	e-mail

¹<https://github.com/LTS5/cmp>

²<http://www.nitrc.org/projects/panda/>

³<https://www.nitrc.org/projects/mrcap/>

⁴<https://github.com/openconnectome/m2g/>

3. Materials and Methods

In the following section, the methods used for generating the connectivity matrix of a human brain are described in detail. The connectome mapping toolkit⁵ was chosen as pipeline, because it is the only pipeline which allows mapping the connectome at multiple-scales. Furthermore, it offers the greatest variety of state-of-the-art tractography methods [19].

3.1. Data acquisition

The MRI datasets from two healthy subjects (age 32 and 25 years) were acquired at the Medical University of Graz with a 32 channel head coil on a SIEMENS Magnetom Tim Trio 3T system. From each subject 8 diffusion weighted images with different resolution, b-values and number of gradient directions were acquired. The important imaging parameters were summarized in table 2. Additionally, a high resolution morphological T1-weighted MRI was acquired from each subject in a matrix of 224x256x176 voxels of 1mm isotropic resolution.

3.2. Creating the structural Connectome

As previously described and illustrated in figure 7 (section 2.3.1) the process of estimating the structural connectivity networks from the acquired data involves several steps. In general, the process can be characterized by 3 streams or stages. The first stream is the morphological stream.

⁵<https://github.com/LTS5/cmp>

Table 2: Overview of general imaging parameters of the acquired diffusion weighted MRI

Imaging Parameter	Dataset 1	Dataset 2	Dataset 3	Dataset 4	Dataset 5	Dataset 6	Dataset 7	Dataset 8
Sequence	Standard-EPI	Readout-segmented EPI						
Resolution	2x2x3mm	1,5mm iso						
b-value	1000s/mm ²	1000s/mm ²	1000s/mm ²	2000s/mm ²	3000s/mm ²	4000s/mm ²	1000s/mm ²	1000s/mm ²
Averages	2	2	2	2	2	2	2	1
Gradient directions	12	12	12	12	12	12	64	12/20
Echo time	95ms	95ms	125ms	125ms	125ms	125ms	86ms	76ms
Repetition time	6700ms	6700ms	8100ms	8100ms	8100ms	8100ms	6200ms	11700ms
Acquisition time	4min11s	4min11s	4min36s	4min36s	4min36s	4min36s	13min26s	26min50s
Acquisition Matrix	114x114x50	160x160x83						

3.3. Morphological Stream

The acquired $T1w$ image constitutes the basis for the morphological stream. In this stream the white matter as well as the different gray matter structures of the brain are identified. The gray matter structures, such as the cortical gyri, thalamus and brain stem, will later on serve as nodes for the connectome. The white matter is the basis for tractography. The first stage of the morphological stream is the segmentation stage.

3.3.1. Segmentation

In this stage the brain is extracted from the skull and segmented into white matter, gray matter and subcortical areas and the white matter and pial surfaces are reconstructed. The results of this process will serve as basis for the subsequent parcellation stage. For this segmentation process the recon-all command of Freesurfer⁶ was used. This segmentation process is a complex procedure and therefore broken down into 5 sub-steps:

1. Non-uniform intensity correction

The measured signal intensities in the $T1w$ image are not uniform for homogeneous tissue, because of RF-coil uniformity, eddy currents and dielectric resonance effects. Thus, the signal intensities of the same tissue type vary as a function of their spatial locations [20]. The automated segmentation method in Freesurfer assumes a homogeneous intensity for each specific tissue type. Thus, this non-uniformities in the $T1w$ image were corrected using the non-parametric-non-uniform-intensity-normalisation method [69] implemented in the nu_correct tool from the Montreal Neurological Institute (MNI)⁷.

2. Talairach transformation

In the second step, the intensity corrected images were transformed into the Talairach space via an affine transformation (see section for further details on affine transformation) [20]. The Talairach space, also known as talairach atlas, is a 3 dimensional standardized coordinate system. The idea of this atlas is that distances between known anatomic structures (landmarks) are proportional to the brain size. By using this relationship the brain structures can be mapped independently from differences in size and shape into a standardized grid. The origin of this coordinate system is the anterior commissure [71].

⁶freesurfer.net/

⁷<http://www.bic.mni.mcgill.ca/software/distribution/>

Bringing the anatomical structures into a common coordinate system serves as basis for the subsequent segmentation process. The transformation matrix was determined using the talairach registration procedure developed by the Montreal Neurological Institute and implemented in the talairach_avi script of Freesurfer. This procedure uses a gradient descent algorithm at multiple scales to estimate the 12 transformation parameters by maximizing the correlation between the individual volume and an average volume composed of a large number of previously aligned brains [20].

3.Skull stripping

In the third step, the skull and non-brain tissue were removed from the intensity corrected images using a hybrid skull stripping algorithm [66]. In order to get robust and good results this method combines two different types of algorithms, the watershed approach and the deformable surface approach.

Watershed approach

The aim of the watershed approach is to segment the surface of the brain volume which will serve as initialization for the subsequent deformable surface approach. The main idea of this approach is representing the gray-level image as a topographical relief. Thus, voxel intensities are interpreted as high information, where bright voxels represent hills and dark voxels correspond to valleys. Now every local minimum in the relief (valley) is filled with water. In points where water from different basins meets, a barrier is built. Now the borders of the valleys are known and each valley represents a segmented part in the image.

In T1w MRI white matter is bright and surrounded by darker gray matter and even darker CSF. Therefore, white matter represents a hill whereas CSF is dark and represents a valley. Since the aim of the watershed algorithm is segmenting different valleys the T1w MRI was inverted. Afterwards the watershed algorithm is applied starting from the white matter and non-brain tissue resulting in two basins, the brain and non-brain tissue (CSF,skull, eyes, etc.). Given the fact that the watershed algorithm is just intensity based and incorporates no geometrical information same parts of the brain can still be removed and parts of non-brain tissue can be preserved. Therefore, a second algorithm based on geometrical information, the active contour algorithm, was used to find the true brain boundary [66][33].

Active contour model

The active contour model incorporates geometrical information and describes the contour of an object by a parametric curve, the so-called snake. This snake is iteratively deformed by different kind of forces until equilibrium is reached between these forces. In this case the desired boundary is achieved and the contour of the object is estimated. The active contour model can be mathematically expressed as:

$$\forall p \in P \quad \mathbf{S}(p, 0) = \mathbf{S}_0(p) \quad (7)$$

$$\forall (p, t) \in P \times R^+ \quad \frac{\delta \mathbf{S}(p, t)}{\delta t} = \mathbf{F}(\mathbf{x}, t) \quad (8)$$

where \mathbf{S}_0 is the initial contour or snake, P is the parameter space and $\mathbf{F}(\mathbf{x}, t)$ is the local force applied to the surface S at location $x = S(p, t)$

The active contour model implemented in Freesurfer models the brain surface with a icosahedron consisting of 10 242 vertices. The initial contour or surface template is the segmented result of the watershed algorithm. The following three different forces are responsible for the deformation process

- Atlas based force F_A : This force ensures that the snake holds the brain shape by using geometric information of a brain atlas.
- Intrinsic curvature reducing force F_S : This force ensures smoothness of the snake by penalizing high local curvatures.
- MRI-based force F_{MRI} : This force ensures that the snake is drawn toward the true brain boundary by denoting volume intensities from the T1w image.

The deformation of each vertex can be expressed as follows:

$$x_k^{t+1} = x_k^t + [F_S(x_k^t, t) + F_M(x_k^t, t) + F_A(x_k^t, t)]\delta t \quad (9)$$

where x_k^t is the k-th vertex of the icosahedron at the timestep t , x_k^{t+1} is the k-th vertex of the icosahedron at the next timestep and δt the time between two steps defined in Freesurfer with 0.5

If the forces are in equilibrium, the coordinates of the vertexes do not change anymore and the brain was successfully extracted from the skull [66].

4. Automated subcortical segmentation

Once the brain was extracted from the skull, the subcortical areas were segmented using the automatic subcortical segmentation proposed by Fischl [6] and implemented in Freesurfer. This segmentation method is based on the Bayesian approach and the probability of a segmentation W given the observed image I is

$$p(W|I) \propto p(I|W)p(W) \quad (10)$$

where $p(W|I)$ is the probability of a segmentation W given the observed image I , $p(I|W)$ is the conditional probability and $p(W)$ is the prior probability of the segmentation

This method has the advantage that a-priori information can be incorporated in the segmentation process. However, the variability of the subcortical regions in the brain generates the problem that no common a priori information as well as conditional probability $p(I|W)$ can be defined. Therefore, an atlas is used which allows them to vary with the location. The introduction of an atlas needs a transformation which maps the image coordinates on atlas coordinates. This is done by an affine transformation matrix L . Once this transformation is known, the a priori information can be estimated. This a priori information has two forms. Firstly, a global spatial information provided by the atlas and the transformation L is used to express the probability $p(W(\mathbf{r}) = c)$ that a class c_i occurs at a specific location in the atlas. The classes represent brain areas e.g. the amygdala and were manually defined in a large dataset. Secondly, spatial relationships between neighbouring regions or classes are incorporated like for example that the “posterior amygdala is frequently superior to anterior hippocampus, but never inferior to it”[6]. With the knowledge of the a priori information and the relationship L between native space and atlas space equation 10 can be re-written:

$$p(W|I, L) \propto p(I|W, L)p(W) \quad (11)$$

By considering the noise at each voxel and by assuming that it is independent from other voxels in the image, the conditional posteriori probability $p(I|W, L)$ can be re-written:

$$p(I|W, L) = \prod_{r \in R} p(I(Lr)|W(r)) \quad (12)$$

where \mathbf{r} is the location in the native image space, and R is the image domain

The prior probability of the full segmentation can be expressed as follows:

$$p(P) \propto \prod_{r \in N} p(W(\mathbf{r})) \prod_{i=1}^K p(W(\mathbf{r}_i) | W(\mathbf{r}), \mathbf{r}_i) \quad (13)$$

where N is the neighbour of a class, r is the central voxel of a class and r_i is the location of the neighbour

By combining equation 12 and 13 the segmentation class at each location can be computed by maximizing the conditional posterior probability [6].

$$\begin{aligned} W(\mathbf{r}) &= \underset{c}{\operatorname{arg\,max}} p(W(\mathbf{r}) = c | W(\mathbf{r}_i), \mathbf{I}(L(\mathbf{r})), \mathbf{r}_i) = \\ &= p(\mathbf{I}(L(\mathbf{r})) | W(\mathbf{r}) = c) p(W(\mathbf{r}) = c) \prod_{i=1}^K p(W(\mathbf{r}_i) | W(\mathbf{r}) = c, \mathbf{r}_i) \end{aligned} \quad (14)$$

In figure 8 the segmented cortical areas are shown.

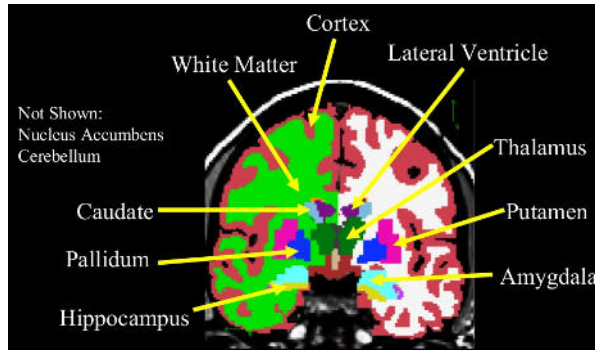


Figure 8: Slice of the human brain showing the segmented subcortical areas. Image taken from⁸

.

5. Surface construction

In the last step, the white matter surface and pial surface were generated from the successfully segmented regions. The white matter surface is the border between the segmented gray matter and white matter and the pial surface is the boarder between gray matter and cerebrospinal fluid. The surfaces are reconstructed by detecting the plane of least variance for every voxel [20].

⁸<http://de.slideshare.net/yashika54/working-with-freesurfer-rois-surfernmrmgharvardedu>

3.3.2. Parcellation

Once the surface model of the brain is segmented, neuroanatomical regions can be assigned to this model. This process is called parcellation of the brain. The automatic parcellation approach proposed by Fischl and implemented in Freesurfer was used for labelling the cortical sulci and gyri. This is a probabilistic process based on the Bayesian approach and incorporates two kinds of information, geometrical information from the cortical surface model and neuroanatomical convention from a training set. The training set contains 40 manually labelled T1wMRI. The atlas used in this parcellation process was the Desikan-Killiany atlas composed of 34 anatomical areas for each hemisphere. The procedure for labelling a parcel is the same as the segmentation of the subcortical areas (see 4. Automatic subcortical segmentation). Here again, the location of a parcel $P(\mathbf{r})$ is computed by maximizing the conditional posterior probability [23][7].

$$\begin{aligned}
 P(\mathbf{r}) &= \underset{c}{\operatorname{arg\,max}} p(P(\mathbf{r}) = c | P(\mathbf{r}_i), \mathbf{G}(f(\mathbf{r})), \mathbf{r}_i) = \\
 &= p(\mathbf{G}(f(\mathbf{r})) | P(\mathbf{r}) = c) p(P(\mathbf{r}) = c) \sum_{i=1}^K p(P(\mathbf{r}_i) | P(\mathbf{r}) = c, \mathbf{r}_i)
 \end{aligned} \tag{15}$$

where K is the number of vertices, \mathbf{r} is the location in native space, f is the affine transformation matrix or atlas function and c are the 34 classes in each hemisphere

The result is a fully parcelled brain shown in figure 9

Sub-parcellation

The brain was further subdivided into 998, 446, 217, 112 brain regions or parcels using the Lausanne atlas. The same transformations used for the Desikan-Killiany atlas and described above were used for the Lausanne atlas to maintain the topographical conditions of mapping. The Lausanne atlas was developed by a group of Swiss researchers [32]. They used a two-phase heuristical approach to further subdivide the 66 anatomical regions, called parcels p , of the averaged Desikan-Killiany template brain into 998 equally sized non-anatomical regions, called ROIs. In the first phase the surface size of a ROI was calculated according to the whole brain size. Afterwards the number of ROIs for each parcel was calculated according to the surface area of the parcel. For each parcel p region growing was started until the desired surface area was reached. This was the first ROI of the parcel p . A second ROI was generated by starting region-growing at a point near to the first ROI. This process was repeated until the desired number of ROIs

within a parcel was reached. Once a parcel was fully covered with ROIs, the centre of gravity was calculated for each ROI and the region-growing was started simultaneously for all ROIs in the parcel resulting in compact and equally sized regions. Merging always 2 or 3 regions of the higher resolution template brain results in a new template brain with 446, 217 and 112 regions. Adding up the 17 subcortical structures segmented in step 4 of the segmentation process described previously results in 1015, 463, 234, 129 and 83 parcels at each scale (figure 9) [32][46].

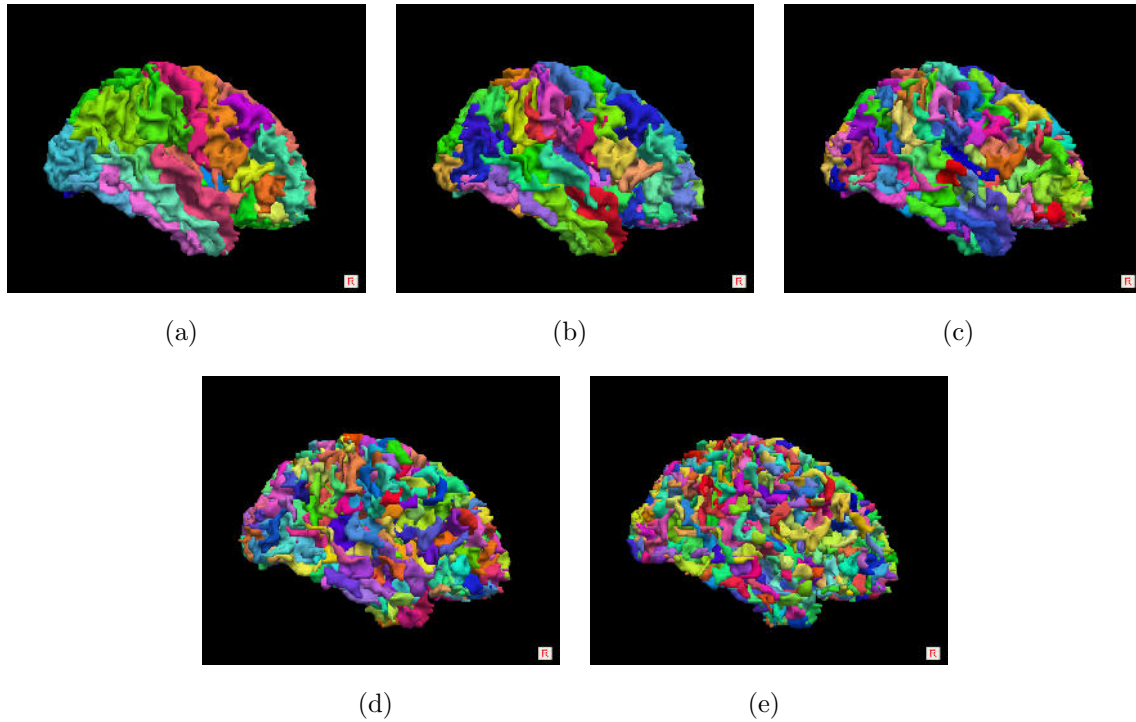


Figure 9: Cortex parcellation at 5 different scales using Desikan-Killiany and Lausanne atlas: (a) 83 regions, (b) 129 regions, (c) 234 regions, (d) 463 regions, (e) 1015 regions

3.3.3. Registration

Registration is a standard preprocessing step for determining a transformation matrix that aligns images from different imaging spaces to a target space. Two different imaging spaces are part of the connectome mapping procedure: the morphological space for determining the white matter mask and the cortical and subcortical brain areas and the

diffusion space for determining the white matter pathways. For a successful construction of the connectivity matrix the voxel on position (x,y,z) of T1w image must contain the same anatomical location of the brain as the voxel of the diffusion weighted image. Therefore, the results of the morphological stream are linearly registered to the diffusion space, or more precisely to the b0 image, which serves as reference space. The linear registration is represented by an affine transformation matrix. This transformation matrix A provides 12 degrees of freedom (DOF) including translation(3DOF), rotation(3DOF), shearing(3DOF) and scaling(3DOF).

$$\mathbf{v}_{\text{tar}} = \mathbf{A}\mathbf{v}_{\text{scr}} \quad (16)$$

The aim of the registration process is to find the transformation matrix which best fits the source image to the target image. This can be mathematically be defined as minimizing the misalignment between the source and target image using a cost-function C .

$$\arg \min_{\mathbf{A}} C(I_{\text{src}}, I_{\text{tar}}) \quad (17)$$

where C is the correlation ratio, A the transformation matrix, I_{src} the source image and I_{tar} the target image

Finding the minimum cost value (equation 17) is a very time consuming step for high-resolution images (1mm isotropic resolution) and therefore multi-resolution optimization procedures are used. This technique subsamples the original images to 8,4 and 2 mm and determines the affine matrix by starting the minimizing procedure for the largest resolution. The determined parameters serve as initial parameters for the next higher resolution and the procedure is repeated until the resolution of the target image is reached [38][37].

The registration was done using FSL⁹ tool FLIRT (FMRIB's Linear Image Registration Tool) which determines the registration matrix using the multi-resolution approach described above. The source, target and registered image are illustrated in figure 10

⁹<http://fsl.fmrib.ox.ac.uk/fsl/fslwiki/>

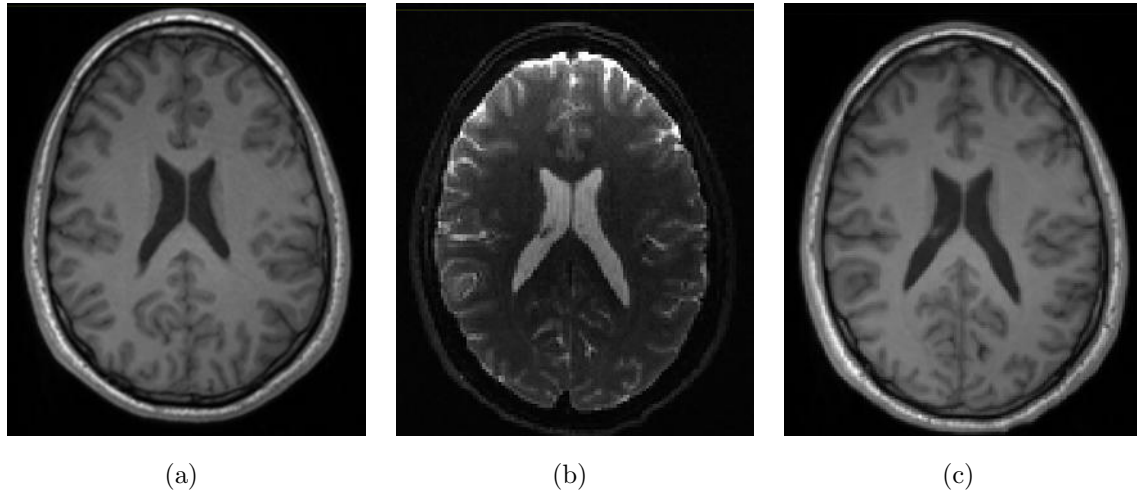


Figure 10: The source T1w image (a) in the morphological space, the target b0 image (b) in the diffusion space and the registered T1w image (c) in the diffusion space

3.4. Diffusion Stage

The diffusion stage is the second stream in the connectome procedure. It is necessary for determining the white matter pathways in the brain. These white matter pathways will later on serve as edges in the structural brain network.

3.4.1. Preprocessing

Diffusion weighted images are known to suffer from geometrical distortions. The two major sources are eddy currents and subject motion.

3.4.1.1. Motion correction

In diffusion weighted MRI different gradient directions are necessary for estimating the underlying diffusion direction of water molecules. A movement of the subject's head during the acquisition process leads to a different brain position in the acquired image. This means that the same slice of the head contains different brain locations for different

gradient directions. The aim of the motion correction process is aligning all acquired diffusion weighted images so that they contain the same anatomical location in each voxel. Only on this condition the diffusion direction of the water molecules can be estimated in a correct way.

Motion correction was done by registering the different diffusion weighted images onto the b0 image using the MCFLIRT method of FSL¹⁰. This method determines an affine registration for every diffusion weighted image as described in section 3.3.3.

3.4.1.2. Eddy current correction

During image acquisition a change in magnetic field occurs from rapid switching on/off the strong diffusion weighting gradients. This change in magnetic field induces eddy currents in the gradient coils of the MRI scanner. These eddy currents in turn produce a time-dependent magnetic field which acts against the origin gradient field and thereby modifies the sampled trajectory in k-space. This leads to geometric distortions in the reconstructed diffusion weighted image [4].

The eddy current distortions were corrected by registering the diffusion weighted images onto the b0 image using FSLs eddy correct tool¹¹. The method of this tool determines a linear affine transformation matrix as explained in section 3.3.3.

In figure 11 the acquired dw image and the corrected image are shown.

¹⁰<http://fsl.fmrib.ox.ac.uk/fsl/fslwiki/>

¹¹<http://fsl.fmrib.ox.ac.uk/fsl/fslwiki/>

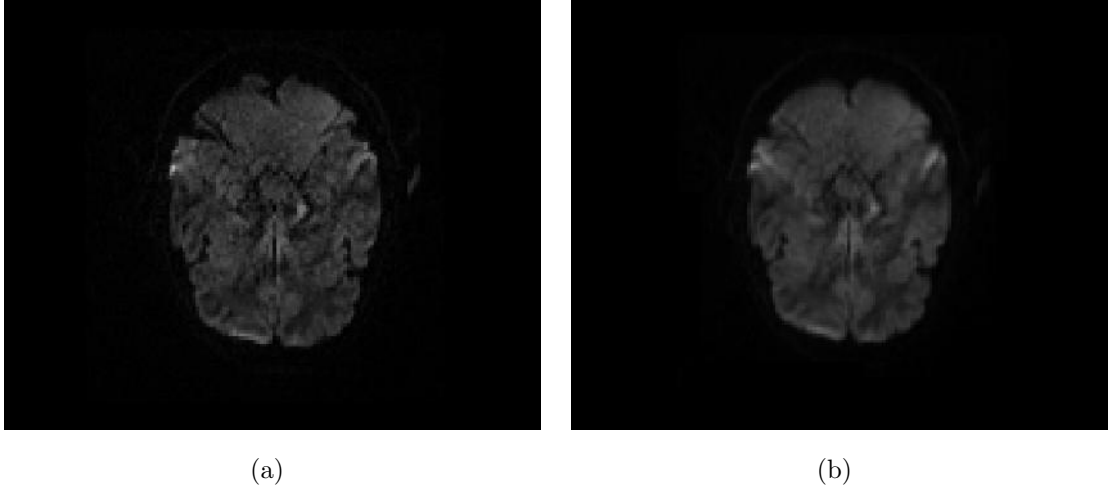


Figure 11: Raw diffusion weighted image (a) and result after motion and eddy-current correction (b)

3.4.2. Estimation of the diffusion direction in each voxel

For a successful reconstruction of the white matter pathways in the brain, the diffusion direction of water molecules is determined. Several different approaches exist for describing this diffusion process within a voxel. Within this thesis two different techniques are used, the most common diffusion tensor model and the fiber orientation distribution function.

3.4.2.1. Estimation of the diffusion tensor

The linear least squares method is the most common method for estimating the diffusion tensor from raw diffusion data. This estimation method minimizes the error between the measured signal S_k and $S_0 e^{-b\mathbf{g}_k^T \mathbf{D} \mathbf{g}_k}$ in the L2 norm (equation 18) [47].

$$\min_{\mathbf{D}} \sum_{k=1}^N \left\| S_k - S_0 e^{-b\mathbf{g}_k^T \mathbf{D} \mathbf{g}_k} \right\|_2^2 \quad (18)$$

where \mathbf{D} is the diffusion tensor, S_k is the measured signal along a gradient direction, S_0 is the signal obtained from the baseline image, b is the diffusion weighting factor and \mathbf{g}_k the normalized diffusion gradient vector

As mentioned before the diffusion tensor has 6 independent components. This means for solving equation 18 at least six measurements S_k along six non-collinear gradient directions g_k and also one baseline image ($b = 0$) are necessary. A system of six equations can be devised with these measurements [44].

$$\begin{aligned}
S_1 &= S_0 e^{-b \mathbf{g}_1^T \mathbf{D} \mathbf{g}_1} \\
S_2 &= S_0 e^{-b \mathbf{g}_2^T \mathbf{D} \mathbf{g}_2} \\
&\vdots \\
S_6 &= S_0 e^{-b \mathbf{g}_6^T \mathbf{D} \mathbf{g}_6}
\end{aligned} \tag{19}$$

For each individual gradient direction the apparent diffusion coefficient (ADC) can be calculated and the equation system 19 can be expressed in terms of ADCs:

$$\begin{aligned}
ADC_1 &= \ln(S_0/S_1)/b = \mathbf{g}_1^T \mathbf{D} \mathbf{g}_1 \\
ADC_2 &= \ln(S_0/S_2)/b = \mathbf{g}_2^T \mathbf{D} \mathbf{g}_2 \\
&\vdots \\
ADC_6 &= \ln(S_0/S_6)/b = \mathbf{g}_6^T \mathbf{D} \mathbf{g}_6
\end{aligned} \tag{20}$$

This equation system can be rewritten in matrix-vector-notations. The diffusion tensor is therefore represented by a six element column vector \mathbf{d} [44]

$$\mathbf{d} = [D_{xx}, D_{yy}, D_{zz}, D_{xy}, D_{xz}, D_{yz}]^T \tag{21}$$

The diffusion gradient encoding matrices from each of the six measurements (i) are represented as a six element row-vector \mathbf{H}_i and combined into a large 6x6 \mathbf{H} matrix [44].

$$\mathbf{H} = \begin{pmatrix} g_{x1}^2 & g_{y1}^2 & g_{z1}^2 & 2g_{xy1} & 2g_{xz1} & 2g_{yz1} \\ g_{x2}^2 & g_{y2}^2 & g_{z2}^2 & 2g_{xy2} & 2g_{xz2} & 2g_{yz2} \\ & & & \vdots & & \\ g_{x6}^2 & g_{y6}^2 & g_{z6}^2 & 2g_{xy6} & 2g_{xz6} & 2g_{yz6} \end{pmatrix} \tag{22}$$

The calculated apparent diffusion coefficients (ADC) from each individual measurement are expressed in an ADC-vector \mathbf{Y} [44]

$$\mathbf{Y} = [ADC_1, ADC_2, \dots, ADC_6]^T \quad (23)$$

The data for each acquisition can be expressed as: [44]

$$\mathbf{Y} = \mathbf{H}\mathbf{d} \quad (24)$$

With exactly six diffusion gradient directions, \mathbf{d} can be exactly determined analytically from equation 24 by multiplying both sides of equation 24 by the inverse of \mathbf{H} [44].

$$(\mathbf{H}^{-1}\mathbf{H})\mathbf{d} = \mathbf{Id} = \mathbf{H}^{-1}\mathbf{Y} \quad (25)$$

In general, more than six gradient directions are acquired to reduce the influence of noise in the estimation procedure. The diffusion gradient matrix is not a square matrix anymore and therefore no true inverse H^{-1} exists. Equation 24 can be solved by calculating the pseudoinverse of \mathbf{H} [44].

$$\mathbf{H}^\Psi = (\mathbf{H}^T\mathbf{H})^{-1}\mathbf{H}^T \quad (26)$$

Now the linear least squares fit of the diffusion tensor can be calculated by multiplying both sides of equation 24 with the pseudoinverse of \mathbf{H} [44]

$$\mathbf{H}^\Psi\mathbf{H}\mathbf{d} = \mathbf{Id} = \mathbf{H}^\Psi\mathbf{Y} \quad (27)$$

This estimation was done for each voxel in the acquired diffusion weighted images.

3.4.2.2. Estimating the fiber orientation distribution function

The fiber orientation distribution function was estimated using the constrained spherical deconvolution method introduced by J.D Tourinier and implemented in the Software MRTRIX¹² [35].

In this model, the orientation of fibers within a voxel is described as a function of the unit sphere using spherical harmonics [36]. Spherical harmonics (SH), in general indicated

¹²<http://www.brain.org.au/software/mrtrix/>

by Y_l^m , define an orthonormal basis over the sphere S. The following parametrization is used [70]:

$$s = (x, y, z) = (\sin\theta\cos\varphi, \sin\theta, \sin\varphi, \cos\theta) \quad (28)$$

where s is a location on the unit sphere (therefore $r = 1$), θ is the elevation angle and φ is the azimuthal angle

The basis functions Y_l^m are defined as [70][51]:

$$Y_l^m = \sqrt{\frac{2l+1}{4\pi} \frac{(l-m)!}{(l+m)!}} P_l^m(\cos\theta) \exp(im\varphi) \quad (29)$$

where l denotes the order, $m = -l, \dots, 0, \dots, +l$ is the phase factor and P_l^m are the associated Legendre polynomials

Figure 12 shows the SH basis function Y_l^m for $l = 0, 1, 2$ [70].

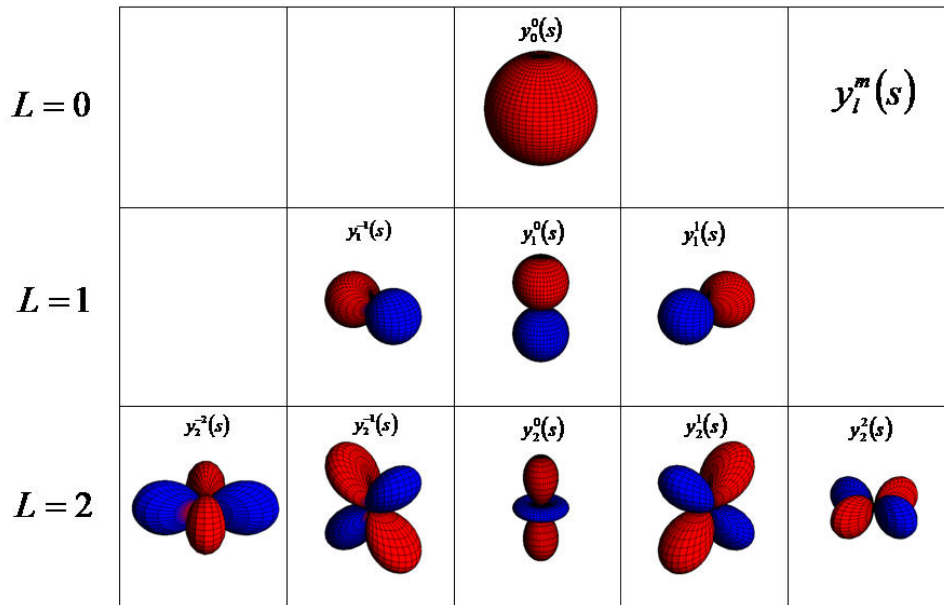


Figure 12: SH basis function for $l = 0, 1, 2$. Modified picture taken from [70].

Since Y_l^m are basis functions any spherical function can be expressed as a linear combination of these basis functions [51]

$$f(\theta, \varphi) = \sum_{l=0}^{\infty} \sum_{m=-l}^l c_l^m Y_l^m(\theta, \varphi) \quad (30)$$

where $f(\theta, \varphi)$ is a user-defined function, c_l^m are coefficients of the SH series and $Y_l^m(\theta, \varphi)$ are SH basis functions.

As previously mentioned, the basic idea of this method is to describe the orientation of fibers present in a voxel as a linear combination of spherical harmonics, the so-called fiber orientation distribution function. In order to achieve this, it is assumed that all fibers in the brain have identical diffusion characteristics. This means that the diffusion profiles measured from two independent fiber populations in the brain are identical in all aspects. Thus, the dw signal profile measured from one single fiber population can be represented as an axially symmetric response function $R(\theta)$ in spherical coordinates. The measured signal $S(\theta, \varphi)$ from a voxel containing several different fiber populations can therefore be represented as weighted sum of the rotated response function so that they are aligned with their respective orientation [36].

$$S(\theta, \varphi) = \sum_i f_i \mathbf{A}_i R(\theta) \quad (31)$$

where $S(\theta, \varphi)$ is the diffusion weighted signal attenuation in spherical coordinates, f_i is the volume fraction of the i -th fiber population within a voxel, A_i is the operator representing a rotation onto the direction (θ_i, φ_i) and $R(\theta)$ is the axially symmetric response function

Equation 31 can be further expressed as convolution of the fODF with the response function over the unit sphere (figure 13):

$$S(\theta, \varphi) = F(\theta, \varphi) \otimes R(\theta) \quad (32)$$

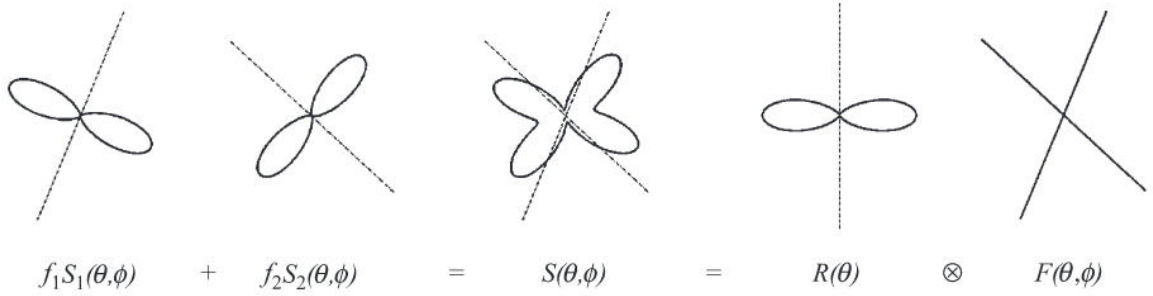


Figure 13: Principle of constrained spherical deconvolution: image taken from [36].

The voxel contains two fiber populations, represented by the dotted line, with different orientations (θ_1, ϕ_1) and (θ_2, ϕ_2) but identical volume fractions $f_1 = f_2 = 1/2$. The continuous line represents the signal attenuation profile $S(\theta, \varphi)$. The sum of the signal attenuation profiles weighted by their volume fractions results in the measured diffusion weighted signal profile $S(\theta, \phi)$. This is equal to the convolution of the axially aligned response function $R(\theta)$ with a fiber orientation distribution function $F(\theta, \varphi)$

From equation 32 it becomes apparent that the fiber orientation distribution can be estimated by performing spherical deconvolution of the response function from the diffusion weighted signal attenuation profile. Before the spherical deconvolution can be performed, the signal attenuation profile and the response function must be estimated.

Signal attenuation profile modelling using SH:

The diffusion weighted MRI signal is acquired using different gradient directions applied over a sphere. The first step in modelling the signal attenuation profiles is the parametrization of the gradient directions using equation 28. After parametrisation the signal can be expressed as a linear combination of basis functions $Y_l^m(\theta, \varphi)$ in spherical coordinates [40].

$$S(\theta, \varphi) = \sum_{l=0}^L \sum_{m=-l}^{m=l} c_l^m Y_l^m(\theta, \phi) \quad (33)$$

where c_l^m is the harmonic series coefficient, $Y_l^m(\theta, \phi)$ are the SH basis functions and $S(\theta, \varphi)$ is the measured signal attenuation in spherical coordinates

Furthermore, equation 33 can be expressed as a linear system using matrix-vector notation. This results in the following equation [40]:

$$\mathbf{s} = \mathbf{B}\mathbf{c} + \epsilon \quad (34)$$

where \mathbf{s} is the diffusion weighted signal vector of size $n_s \times 1$, n_s denotes the number of gradient directions, \mathbf{B} is a matrix of size $n_s \times n_c$ containing the spherical harmonic basis functions, \mathbf{c} is the harmonic series coefficient vector of size $n_c \times 1$ and epsilon is the noise vector

This equation can be rearranged to determine the spherical harmonic coefficients \mathbf{c} of the signal attenuation. For this linear equation no exact solution exists due to the noise in the acquired dataset. Therefore, a linear least squares approach was used [40].

$$\hat{\mathbf{c}} = \mathbf{B}^{-1}\mathbf{s} \quad (35)$$

Response function estimation:

The spherical deconvolution method requires an important preprocessing step, the estimation of the response function. This process involves several steps. At first the diffusion tensor was estimated from the raw dw data using a least squares approach. For each voxel in the white matter mask the fractional anisotropy was calculated. In voxels with a FA-value higher than 0.7, the diffusion is highly anisotropic and one can further assume that these voxels contain only single fiber populations. Thus, these voxels serve as basis for the response function estimation process. In each of these voxels the major eigenvector was calculated from the diffusion tensor. The direction of the eigenvector was used to estimate the rotation matrix, which is necessary to align the response function with the z-axis. This rotation matrix was then applied to the dw encoding scheme. Now the SH coefficients of each voxel can be calculated applying the spherical harmonic transformation. Finally, all estimated SH coefficients in voxels with a FA value > 0.7 were averaged resulting in the response function illustrated in figure 14 [34][19].

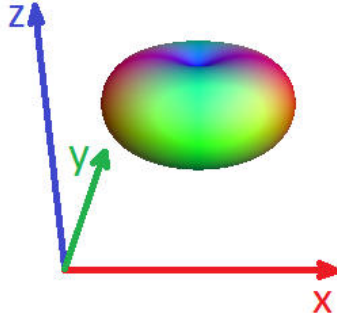


Figure 14: Estimated response function using voxel with a FA value > 0.7

Once the SH coefficients from the dw signal attenuation profile are estimated for each voxel and the response function is determined. The SH coefficients of the fODF can be obtained for every voxel using spherical deconvolution. In the spherical harmonics framework equation 32 can be reduced to a simple matrix multiplication.

$$f = R^{-1}c \quad (36)$$

where f is the spherical harmonic coefficient vector of $F(\theta, \phi)$ with size $n_c \times 1$, c is the spherical harmonic coefficient vector of $S(\theta, \phi)$ with size $n_c \times 1$ and R is the rotational harmonic matrix of $R(\theta)$ with size $n_c \times n_c$

The estimated fODF now describes the distribution of fiber orientation present in a voxel. This serves as basis for the following fiber reconstruction method in section 3.4.3.3.

3.4.3. White matter tractography

White matter tractography is a virtual reconstruction method for representing white matter tracts as three-dimensional trajectories. The simplest reconstruction methods are line propagation methods, also known as deterministic streamline fiber tractography. Within this thesis three of the most known deterministic tractography algorithms were used.

3.4.3.1. Fiber Assignment by Continuous Tracking

The first tractography algorithm used in this thesis was the Fiber Assignment by Continuous Tracking (FACT) technique introduced by S.Mori [65] and implemented in the Diffusion Toolkit¹³ (DTK) [61]. This method is based on the diffusion tensor model and assumes that the main eigenvector of the diffusion tensor coincides with the underlying fiber direction and is constant within a voxel. The output of this method is a 3D trajectory that best approximates the white matter tract [65].

In this approach fiber tracking is bidirectionally started at a random point within a seed-voxel. All voxels in the segmented Freesurfer white matter mask with a FA-value higher than 0.1 served as seed-voxels. From this initialization point the tracking is proceeded according to the direction of the principle eigenvector of the diffusion tensor until it reaches the voxel's boundary. At this point the tracking direction is changed to the direction of the major eigenvector of the neighbouring diffusion tensor. Equation 37 describes the resulting trajectory [65][42].

$$\mathbf{x}_1 = \mathbf{x}_0 + s\mathbf{v} \quad (37)$$

where \mathbf{x}_1 is the point where the tract intersects the voxel boundary, \mathbf{x}_0 is the initial point, s is the continuously variable step size and \mathbf{v} is the principle eigenvector of the diffusion tensor.

This procedure is schematically illustrated in figure 15.

¹³<http://trackvis.org/>

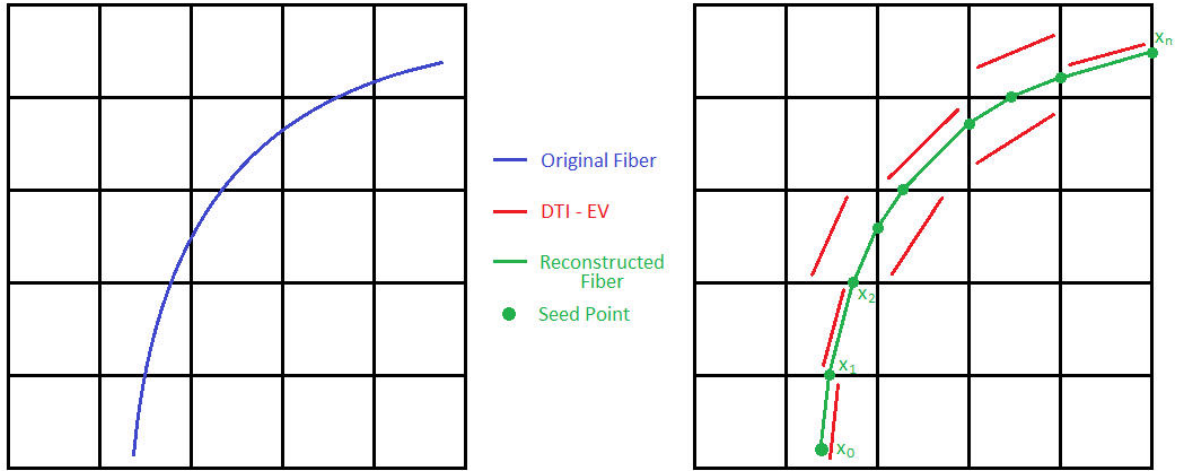


Figure 15: Principle of the fiber assignment by continuous tracking (FACT) approach.

The fiber is reconstructed (green line) in a step-wise process, starting at point x_0 and following the direction of the principle eigenvector of the diffusion tensor (red line) until the voxel's boundary is reached. At this point the tracking direction changes to the direction of the principle eigenvector of the new voxel. This step is repeated until the end voxel is reached or a termination criterion is fulfilled.

The fiber trajectory was reconstructed step by step by repeating the whole procedure again and again. Tracing was stopped if one of these two termination criteria was fulfilled [19]:

- FA-value < 0.1
- change in direction is higher than 60°

3.4.3.2. Streamline Propagation using Euler's method

The second tractography algorithm used in this thesis was the euler's line propagation method introduced by T.E.Conturo [15] and implemented in MRTRIX¹⁴. This method is also based on the diffusion tensor model. In this approach fiber tracking is bidirectionally started from an initial point within a seed-voxel. As before all voxels within the white matter mask with a FA-value higher than 0.1 served as seed-voxels. In contrast

¹⁴<http://www.brain.org.au/software/mrtrix/>

to the previously described FACT method, the tracts are reconstructed following the principle eigenvector of the diffusion tensor for a fixed step length, the so-called step size. Furthermore, the diffusion tensor is not estimated from each voxel in advance. It is estimated at every considered point via tri-linear interpolation of the 8 nearest neighbour voxels from the raw diffusion data. Therefore, the direction of the principle eigenvector can change within a voxel in contrast to the former FACT method where it is constant over the whole voxel [15]. The new point of the reconstructed trajectory is calculated as follows:

$$\mathbf{x}_1 = \mathbf{x}_0 + h\mathbf{v} \quad (38)$$

where \mathbf{x}_1 is the end point of the tract, \mathbf{x}_0 is the initial point, h is the fixed step size and \mathbf{v} is the principle eigenvector of the diffusion tensor at point \mathbf{x}_0

In the next step, the end point x_1 of the trajectory serves as start point and the process is repeated. Figure 16 shows a schematic representation of this technique.

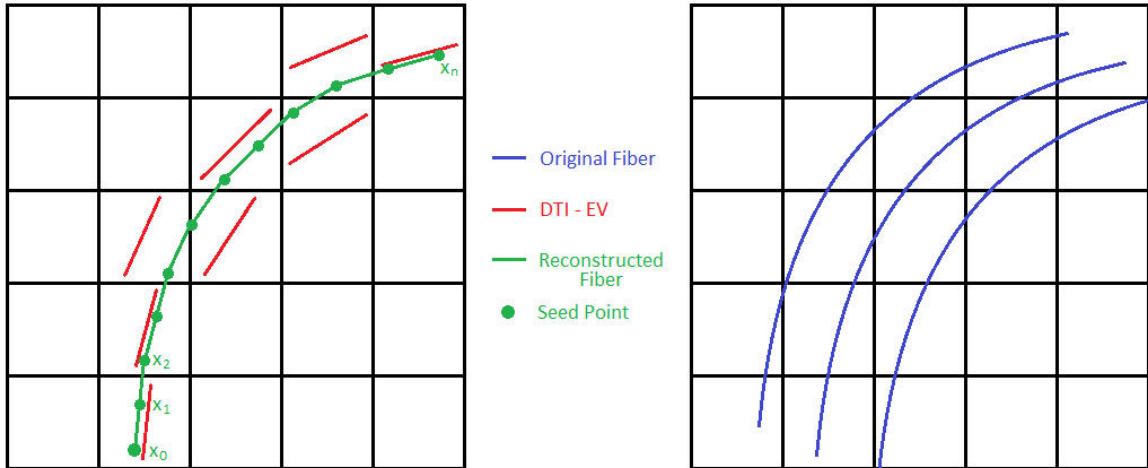


Figure 16: Principle of Euler's method. The fiber is stepwise reconstructed by starting at point x_0 and following the direction of the principle eigenvector of the diffusion tensor (red line) for a fixed step length h , in this case $1/2$ voxel length. At this point x_1 the new diffusion tensor is estimated from the tri-linearly interpolated raw-diffusion signals. Now the trajectory (green line) follows the major eigenvector of the diffusion tensor at this point. This step is repeated until the end voxel is reached or a termination criterion is fulfilled.

A discrete fiber trajectory is obtained by repeating the whole procedure until one of the following termination criteria was fulfilled [19]:

- FA-value < 0.1
- Radius of curvature between two steps is greater than 2mm
- Voxel outside the white matter mask is reached

3.4.3.3. Streamline Propagation using Newton-Raphson method

The third tractography algorithm used in this thesis was a line propagation method based on the fiber orientation distribution function. This algorithm was introduced by JD Tournier [35] and implemented in MRTRIX¹⁵.

In this method fiber tracking is bidirectionally started from an initial point within a seed-voxel. All voxels within the white matter mask with a FA-value higher than 0.1 and an ODF amplitude higher than 0.2 served as seed voxels. From this initial point x_0 the trajectory is stepwise reconstructed following the main peak of the fiber orientation distribution function fODF closest to the current direction, for a defined length h . The new point x_1 of the reconstructed trajectory is calculated as follows [35]:

$$\mathbf{x}_1 = \mathbf{x}_0 + h\mathbf{v} \quad (39)$$

where \mathbf{x}_1 is the end point of the tract, \mathbf{x}_0 is the initial point, h is the fixed step size and \mathbf{v} is the direction estimated from the fODF at point \mathbf{x}_0

The main peak of the fODF closest to the current direction is determined using a Newton-Raphson optimization algorithm. The Newton-Raphson algorithm is an iterative method for finding an extremum of a given function $f(x)$. In case of a maximum, the first derivative of $f(x)$ is zero and the second derivative of $f(x)$ is negative. Therefore, the iterative process for finding the maximum x of a given function $f(x)$ can be expressed as follows [35]:

$$x_{n+1} = x_n - \frac{f'(x_n)}{f''(x_n)} \quad (40)$$

¹⁵<http://www.brain.org.au/software/mrtrix/>

where x_{n+1} is the next point of the iterative process, x_n is the current point, $f'(x)$ is the first derivative of $f(x)$ and $f''(x)$ is the second derivative of $f(x)$

Typically after five steps ($n = 5$), convergence is reached and the peak of the fODF is estimated for the next tracing step. In figure 17 the principle of this algorithm is schematically illustrated [35].

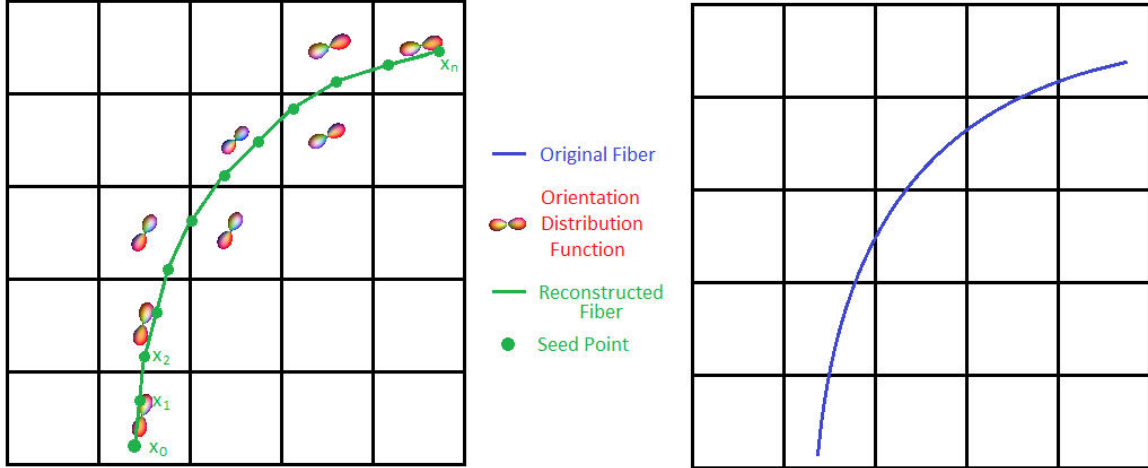


Figure 17: Principle of fiber tracking method. A fiber is stepwise reconstructed by starting at point x_0 and following the direction of the main peak of the fiber orientation distribution for a fixed step length h , in this case $1/2$ voxel length. At this point x_1 the new direction is estimated from the fODF by identifying the nearest peak. Now the trajectory (green line) follows the estimated direction at this point x_1 again for $1/2$ voxel reaching point x_2 . This step is repeated until the end voxel is reached or a termination criterion is fulfilled.

A discrete fiber trajectory is obtained by repeating the whole procedure until one of the following termination criteria is fulfilled [19]:

- FA-value < 0.1
- Fiber orientation distribution amplitude < 0.1
- Voxel outside the white matter mask is reached

3.4.4. Tractography Postprocessing and Parameters

For all three tractography algorithms identical tracking parameters were used. The step size h was adjusted in percentage of the voxel size to make diffusion datasets with different spatial resolution comparable. The number of reconstructed fibers was adjusted from 25 000 up to 650 000 fibers. In table 3 the used parameters are summarized.

Table 3: Overview of tracking parameters used

Number of fibers [10^3]	Step size [Voxel length]
25, 50, 100 175, 350, 650	1/10, 1/2, 1

Furthermore, the globally reconstructed fiber tracts were post processed using a cut-off filter. The idea behind this filter is to eliminate spuriously reconstructed fibers. All reconstructed fibers shorter than 20mm and longer than 400mm were assumed to be non-anatomical and therefore excluded [19].

3.5. Connectome Stage

In the last step the connectivity matrix C is estimated by combining the registered cortical and subcortical regions R with the reconstructed fibers. Every row-element C_i and column-element C_j of the connectivity matrix corresponds to one segmented region R . Therefore, the resulting connectivity matrix has a size of 83×83 for the lowest resolution and 1015×1015 for the highest resolution.

In order only fibers which arise as well as terminate in one of these regions can be assigned to an anatomical connection and an entry in the connectivity matrix. On this account the two endpoints of each fiber tract are calculated and checked if both of them lie within one of these regions R . Is this the case the corresponding cell C_{ij} in the connectivity matrix is increased by one, otherwise the fiber tract is rejected. This procedure is repeated for all fiber tracts resulting in a weighted connectivity matrix illustrated in figure 18

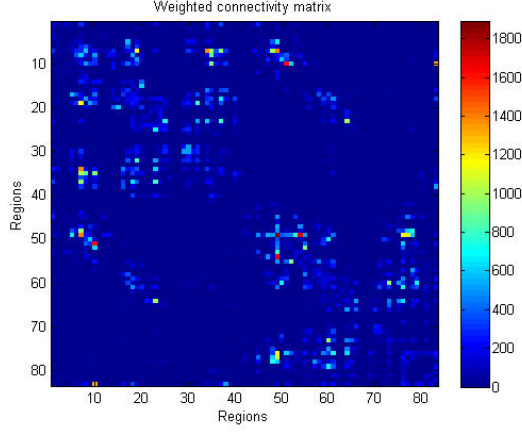


Figure 18: Weighted connectivity matrix

3.6. Connectome Comparison

As briefly mentioned in the background section of this thesis, the resulting structural connectivity matrix can be seen as a network with edges and nodes. Thus, different network measures and statistics can be applied to identify similarities and differences in the organization of neural networks in groups of subjects.

3.6.1. Pearson Correlation

The simplest valid measure for comparing individual connectivity matrices globally is the Pearson correlation coefficient. If x and y are the elements of two connectivity matrices of size N by N , the Pearson coefficient can be calculated using equation 41. Since the connectivity matrix is symmetrical only half of the matrix elements are taken into account for calculation [46].

$$R(x, y) = \frac{\sum_{i=1:N} \sum_{j=i:N} (x_{ij} - \bar{x})(y_{ij} - \bar{y})}{\sqrt{\sum_{i=1:N} \sum_{j=i:N} (x_{ij} - \bar{x})^2 \sum_{i=1:N} \sum_{j=i:N} (y_{ij} - \bar{y})^2}} \quad (41)$$

$$\bar{x} = \frac{\sum_{i=1:N} \sum_{j=i:N} x_{ij}}{N(N+1)/2} \quad \text{and} \quad \bar{y} = \frac{\sum_{i=1:N} \sum_{j=i:N} y_{ij}}{N(N+1)/2} \quad (42)$$

The group of Paulo Rodrigues shows that computing the Pearson correlation coefficient between the connectome matrices of the same subject is an indicator for the robustness of the methods used for generating the structural connectome. Thus, equation 41 is also used for checking the robustness of the methods used [58][46].

3.6.2. Network measures of brain connectivity

Two types of network measures are available, local network measures which describe features of a single node and global network measures which characterize the topology of a network at once. In this thesis global graph properties of the weighted connectivity networks were calculated for all acquisition schemes as well as for all tracking parameters of each subject using the Matlab brain connectivity toolbox [63]. More precisely, the network efficiency, characteristic path length, network density and average node degree were considered. In figure 19 the key measures of network topology are illustrated.

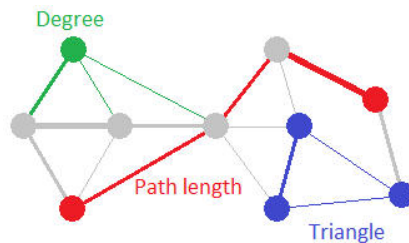


Figure 19: Key measures of network topology. Measures of centrality are based on node degree (green), measures of functional integration are based on shortest path lengths (red), measures of functional segregation are based on triangle counts (blue)

Before calculating the network properties the self-self connections, which means node i is connected to itself, are removed and the resulting connectivity map is normalized to make the connectivity maps resulting from different tracking algorithms and fiber numbers comparable.

3.6.3. Weighted average node degree

The node degree is a basic and important network measure and sometimes termed as nodal strength [8]. The degree of a node i indicates the number of edges connecting

to this node i . This is equivalent to the number of neighbouring nodes of node i . The weighted node degree is given by the sum of all neighbouring edge weights and was calculated with equation 43.

$$k_i^w = \sum_{j \in N} w_{ij} \quad (43)$$

where k_i^w is the weighted degree of the node i and w_{ij} is the weight (probability) of connecting node i with node j in the network.

The degree of all nodes, also called degree distribution, is an important marker of network resilience and development. A node with a high degree is interacting structurally or functionally with many other nodes of the network. The mean of all node degrees is most commonly used by the neuroscience community as a measure of network density or total “wiring cost” of the network [63].

3.6.4. Weighted characteristic path length

The characteristic path length is the most commonly used measure of functional integration. A path represents a route of information flow between pairs of brain regions. The length of a path characterizes the potential for functional integration between brain regions. A shorter path represents a stronger potential for functional integration than a longer path. The shortest weighted path length of a network is the sum of the inverse edge weights connecting two regions i and j (equation 44). A higher edge weight between region i and j implies a stronger association and therefore a shorter path [63].

$$d_{ij}^w = \sum_{a_{uv} \in g^{i^w \leftrightarrow j}} f(w_{uv}) \quad (44)$$

where f is an inverse map from weight to length and $g^{i^w \leftrightarrow j}$ is the shortest weighted path between i and j .

The characteristic path length of the brain network is the average shortest path length between all pairs of nodes and was calculated using equation 45.

$$L^w = \frac{1}{n} \sum_{i \in N} \frac{\sum_{j \in N, j \neq i} d_{ij}^w}{n-1} \quad (45)$$

where L^w is the weighted characteristic path length, n the number of nodes in the network and d_{ij} is the shortest weighted path length (distance) between nodes i and j as defined in equation 44

The characteristic path length is primarily influenced by long paths. In a disconnected network the paths between disconnected nodes have an infinite length whereby the characteristic path length also becomes infinite. This means that the characteristic path length is no longer a meaningful measure of integration for disconnected networks [63].

3.6.5. Weighted global efficiency

The weighted global efficiency is, in addition to the weighted characteristic path length, a further measure of functional integration. It is calculated by averaging the inverse shortest path length of a network. Disconnected nodes which have an infinite path length have a global efficiency of zero. This means that the global efficiency compared to the characteristic path length yields meaningful results for disconnected networks [63].

$$E^w = \frac{1}{n} \sum_{i \in N} \frac{\sum_{j \in N, j \neq i} (d_{ij}^w)^{-1}}{n-1} \quad (46)$$

where E^w is the weighted global efficiency, n is the number of nodes in the network and d_{ij}^w is the shortest weighted path length (distance) between nodes i and j as defined as follows

The global efficiency of a network is another indicator for functional integration. The higher the efficiency between nodes, the more information can be carried between these two nodes [63].

3.6.6. Network density

The density is the most simplistic measure of network structures and is also called connectivity of a network. The network density provides a first indication of how well-connected a network is. A network density of 1 means that all potential edges exists and all nodes

of the network are connected. However, in biological networks only a small fraction of connections exists (range 10-40%) [43]. The network density is defined as the proportion of non-zero edges to the number of potential connections in the network (equation 47) [63].

$$\kappa = \frac{E}{n(n-1)} \quad (47)$$

where κ is the network density, E is the number of non-zero edges in the network and n is the number of nodes in the network

3.7. Evaluation of the structural connectivity matrix

Till now it still remains unclear which connections in the structural connectivity matrix are really existent in the human brain and which are erroneously generated during the complex mapping procedure. Therefore, the resulting connectivity matrices were evaluated by using two types of manually defined structural connectivity matrices. A so-called “FP-matrix” which contains spurious connections and a so-called “Anatomic valid matrix” which contains connections from 8 well known white matter bundles. A connection was defined as artificial if it connects a region from the left temporal lobe with a region from the right frontal lobe or vice versa (figure 21). The anatomic valid matrix was generated with the help of a literature research. In the course of this research the cortical and subcortical regions connected by 8 well known fiber bundles were identified and entered as corresponding edges into the structural connectivity matrix. Fiber bundles of different neuroanatomical nature were chosen to include connections at different levels of difficulty.

- Association fibers: Superior Longitudinal Fasciculus (SLF), Uncinate Fasciculus (UN), Inferior Fronto-occipital Fasciculus (IFOF), Inferior Longitudinal Fasciculus (ILF), Middle Longitudinal Fasciculus (ML), U-fibers (Ufibers)
- Projection fibers: Fornix (Fornix)
- Commissural fibers: Corpus Callosum (CC)

The resulting anatomic valid matrix is illustrated in figure 20.

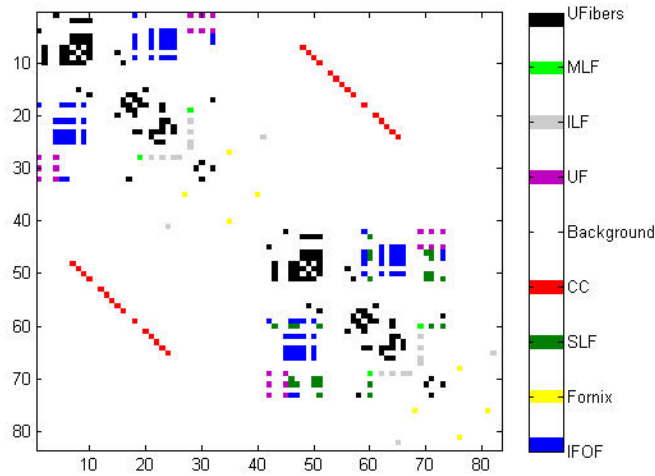


Figure 20: Cortical and subcortical connections of the main white matter pathways in the right hemisphere (Region 1-41) and the left hemisphere (Region 42-83). Corpus Callosum (CC), Middle Longitudinal Fasciculus (MLF), Inferior Longitudinal Fasciculus (ILF), UFibers, Superior Longitudinal Fasciculus (SLF), Uncinate Fasciculus (UF), Inferior Fronto-occipital Fasciculus (IFOF), Fornix.

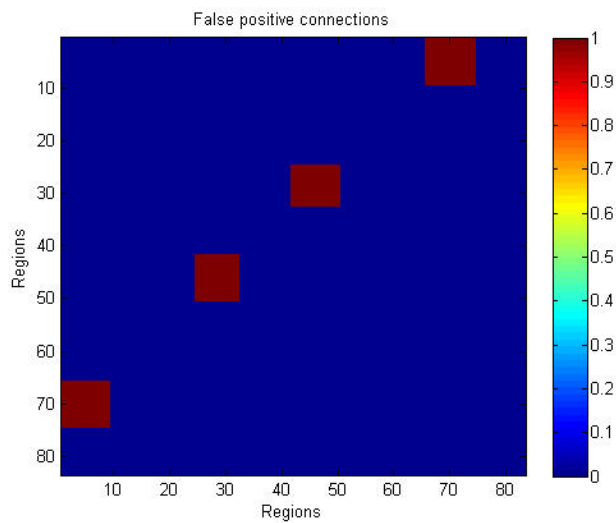


Figure 21: Structural connectivity matrix of defined false positive connections (red dots). FP are connections from the frontal lobe in the right hemisphere to the temporal lobe in the left hemisphere and vice versa.

4. Results and Discussion

In this chapter the results of this thesis are reported and discussed. The first section shows the results of every step in the processing pipeline. The streamline statistics which are a first indication of how well the tracts were reconstructed are demonstrated and discussed in section two. Section three shows the differences in global network measures resulting from different methods or settings in the processing pipeline. The robustness and reproducibility of the used methods are discussed in section four. In the last section the accuracy of the three fiber tracing algorithms are evaluated.

In this chapter several shortcuts will be used. The shortcut “ss1/10” means a step size of one tenth of the voxel length of the diffusion dataset, “ss1/2” means a step size of half of the voxel length and “ss1” a step size of one voxel length. Furthermore the term “FACT” corresponds to the Fiber Assignment by Continuous Tracking method (section 3.4.3.1), “EUL” denotes Euler’s Streamline Propagation method (section 3.4.3.2) and “CSD” refers to the Streamline Propagation based on CSD (section 3.4.3.3).

4.1. Pipeline Results

In this section the results of every individual stage of the connectome mapping process are presented in detail.

4.1.1. Results of the morphological Stream

The first results of the morphological stream are the segmented pia matter and the white matter. The area between pia matter and white matter was used for parcellation resulting in 66, 112, 217, 446 and 998 cortical areas and additionally 17 subcortical areas. Figure 22 shows the results of the morphological stream of subject 2.

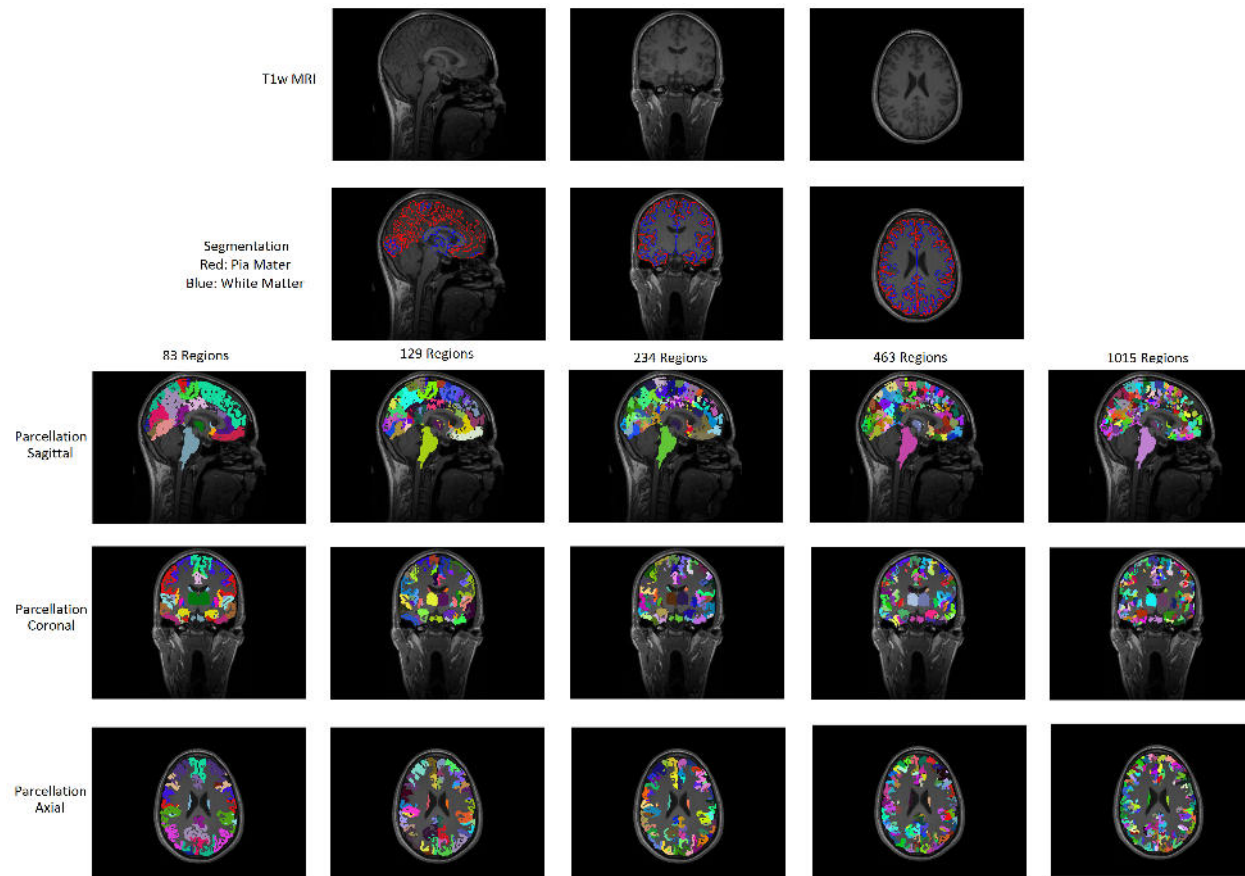


Figure 22: Results of the morphological stream from subject 2. First row shows the acquired T1w MRI. In the second row the segmentation results from Freesurfer are shown. The red line corresponds to the segmented pia mater and the blue line represents the boarder between gray and white matter. The last three rows show the segmented cortical and subcortical areas in the 5 different scales in the sagittal, coronal and axial slice.

4.1.2. Results of the Diffusion Stream

Figure 23 shows the results of the diffusion stream of subject 2 using different methods.

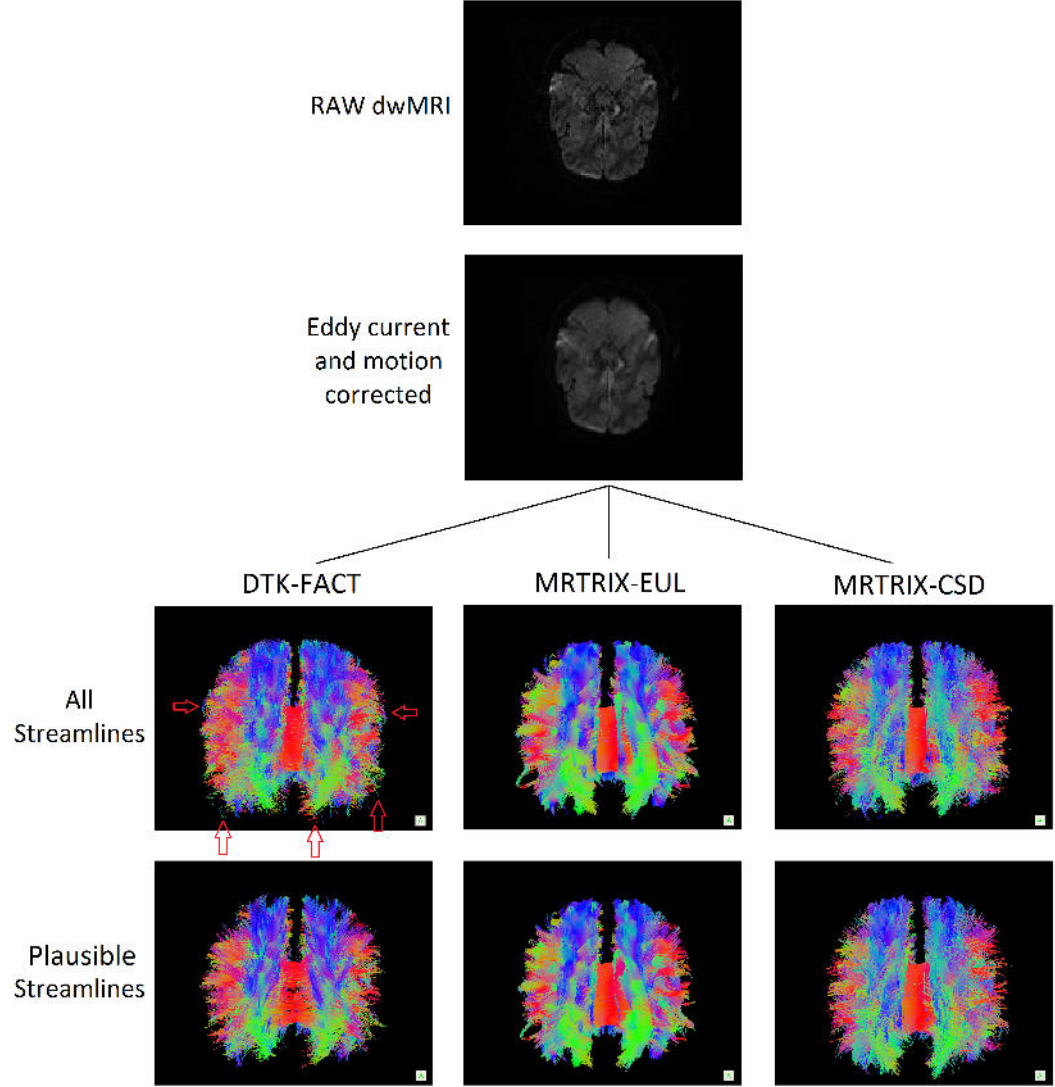


Figure 23: Results of the diffusion stream. The term “All streamlines” means all streamlines generated from the tractographic algorithm and “usable fibers” are fibers which connect two cortical areas and are longer than 20mm and shorter than 400mm. The red arrows indicate artificial fibers resulting from the used tractography algorithm.

4.1.3. Results of the Connectome Stream

The connectivity matrices were calculated by combining the results of the diffusion stream with the results of the morphological stream. This leads to 5 connectivity matrices in different scales. Figure 24 shows the results of the connectome stream for dataset 1 of subject 2.

In figure 25 a part of the Arcuate Fasciculus connecting the superior temporal gyri with the pars opercularis in the left hemisphere is illustrated in all five resolutions. This image shows that the registration procedure used to combine the results of the morphological stream with the results of the diffusion stream works well for all resolutions. All connections are still preserved in all resolutions.

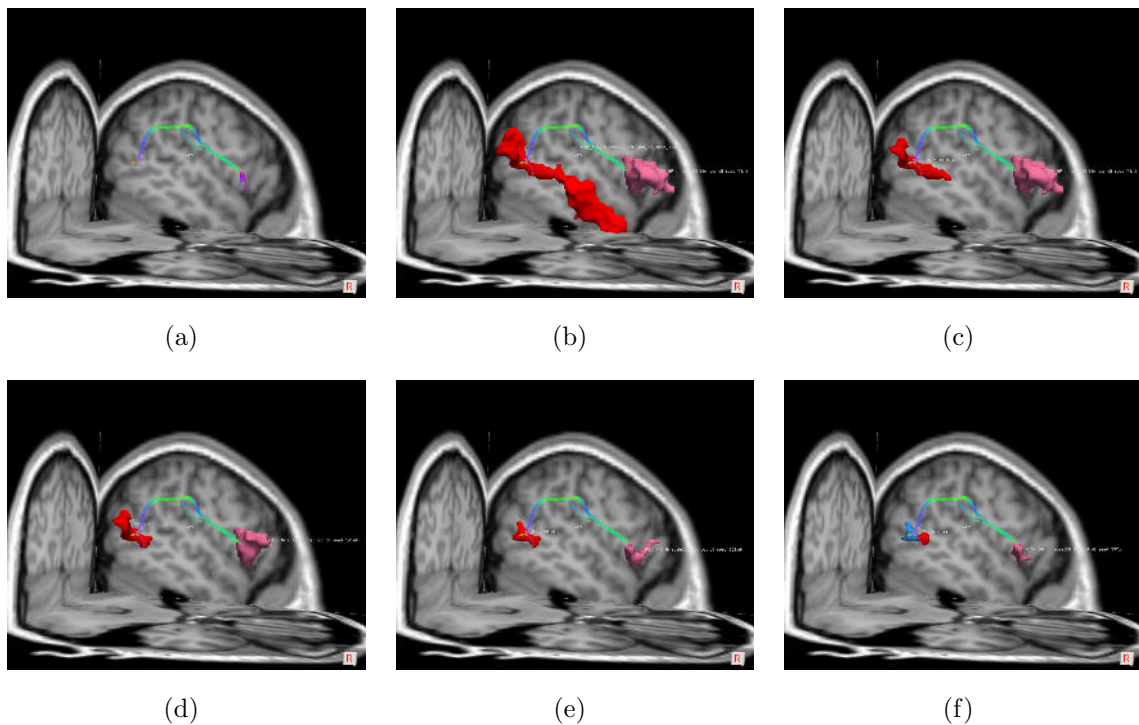


Figure 25: Part of the Arcuate Fasciculus connecting the superior temporal gyri with the pars opercularis in the left hemisphere. Reconstructed Arcuate Fasciculus of subject 2 (a) and connected cortical areas with 83 (b),129 (c),234 (d),463 (e),1015 (f) parcellated regions

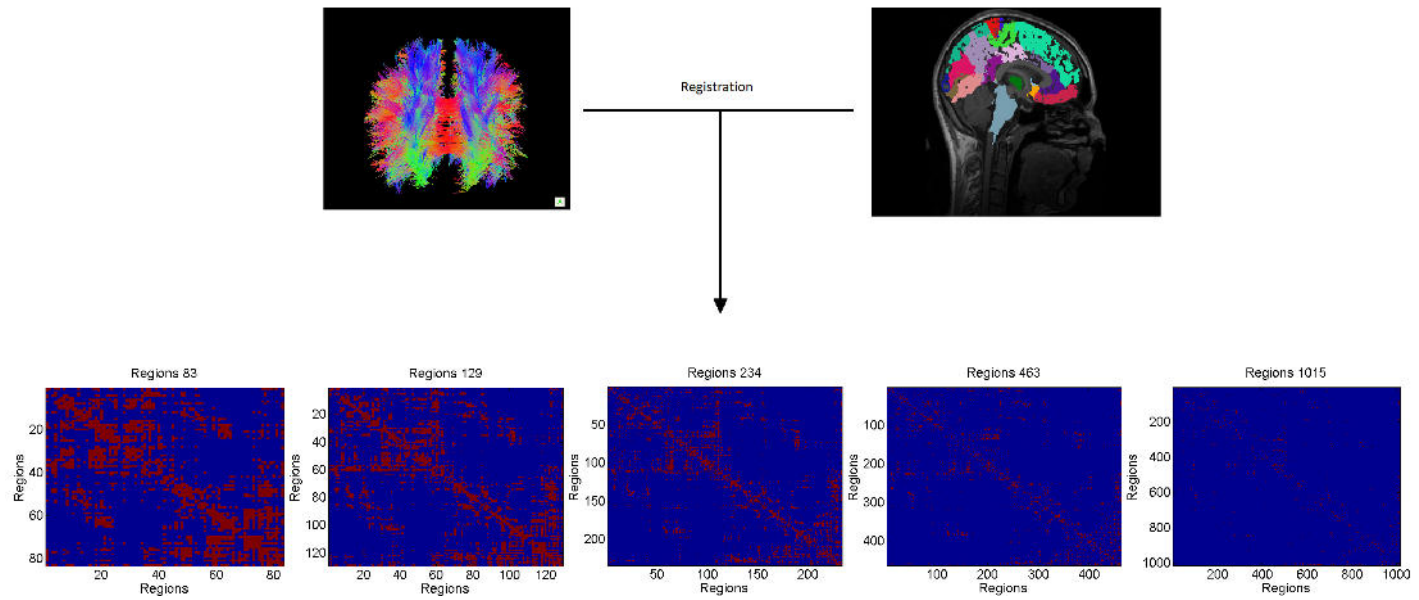


Figure 24: Connectivity matrices in five different scales calculated by combining the registered results of the morphological stream with the results of the diffusion stream.

4.2. Streamline Statistics

The first indication of how well a streamline algorithm worked was the number of valid fibers. A fiber is valid if it connects two cortical areas and therefore only these fibers contributed to the calculation of the structural connectivity matrices. The number of valid fibers, also referred to as usable fibers, was counted for each tractography algorithm and dataset. The influence of the number of reconstructed fibers was considered by calculating the mean and standard deviation of the valid fibers for each method. The results are listed in table 4.

As can be seen in table 4, the standard deviation of the number of fibers is very low, thus the number of usable fibers is independent from the number of seed points used for tractography. The number of valid fibers is about 50% for the FACT approach, 75% for the CSD approach and 77% for the EUL approach and very consistent over different datasets. The FACT approach generates 25% more spurious fibers compared to the CSD and EUL approach. In figure 23 some of these spurious fibers are shown (red arrow). One reason for this high drop in valid fibers is that the FACT algorithm uses no type of interpolation and therefore noisy voxels have a high influence on the reconstruction result. Furthermore, the continuously varying step size of this approach has two major disadvantages. First it can lead to an overshoot in highly curved regions leading to artificial fibers and second the angle threshold (60°) can be a limitation factor leading to fragmentary fibers.

Another interesting observation was that the number of valid fibers increases by 10% for increasing the spatial resolution from $2 \times 2 \times 3 \text{mm}$ to 1.5mm isotropic (dataset 8) for subject 2 and by 5% for subject 1 using the CSD approach. On the one hand the decreasing voxel size leads to a lower SNR, noticeable in a drop of valid fibers for the FACT approach, and on the other hand it leads to a decreased influence of partial volume effects leading to more valid connections. It seems that the CSD approach is most robust against noise, whereas the advantage of lower partial volume effects gets compensated with the disadvantage of the lower SNR for the EUL approach. The influence of the partial volume effects is illustrated in figure 26.

The influence of the number of gradient directions is negligible for DTI approaches but highly significant for the CSD approach. Increasing the number of diffusion gradients leads to a spherical harmonic model of a higher order. On the one hand this makes it possible to reconstruct crossing fibers within a voxel but on the other hand it is even more likely to connect regions which are anatomically not linked. Thus, the drop

in valid connections is likely due to the higher complexity of the model. Thus, these results cannot be directly compared with the results in the subsequent sections because for further calculations only the valid fibers are used and spurious connections are not considered anymore.

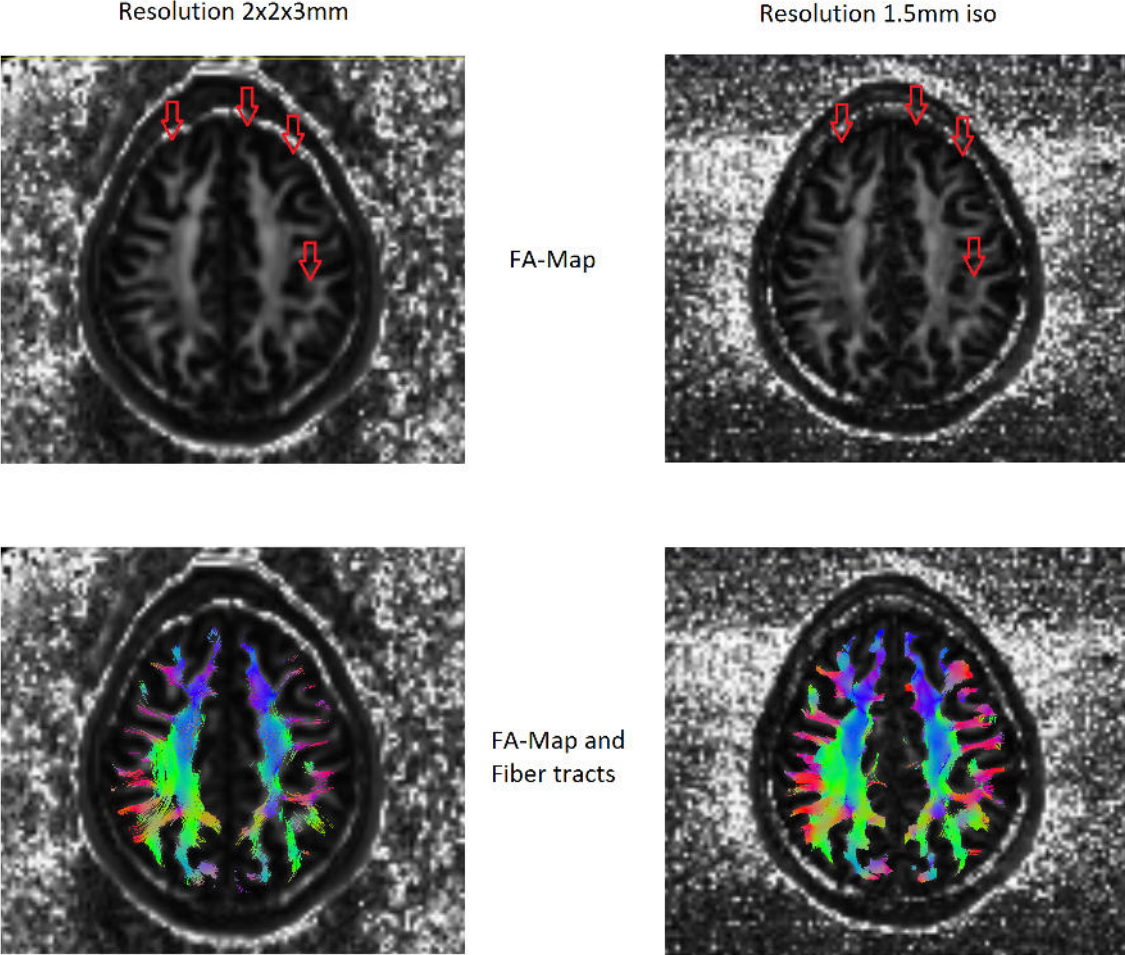


Figure 26: Influence of the partial volume effects on the tractography results. In regions near the white-gray matter boundary or in small white matter tracts partial volume effects play a critical role in fiber reconstruction. The red arrows indicate some of these locations.

Table 4: Summary of streamline statistics. The term “Total” means the number of generated fibers and “Usable” denotes the number of usable fibers. Since the numbers of fibers used for tractographie are adjusted (see table 3) the term “Mean usable” denotes the mean and standard deviation of the different numbers of fibers.

Tractography	Subject 1				Subject 2				
	Total [$\times 10^3$]	Valid [$\times 10^3$]	Usable [%]	Mean Usable [%]	Total [$\times 10^3$]	Usable [$\times 10^3$]	Usable [%]	Mean Usable [%]	
Dataset 1	FACT	93,4	51,4	55	$54,9 \pm 0,40$	96,4	42,9	44,5	$44,3 \pm 0,60$
	EUL ss1/10	100	77,0	77,0	$77,5 \pm 1,00$	100	77,6	77,6	$77,7 \pm 0,14$
	EUL ss1/2	100	79,1	79,1	$79,1 \pm 0,45$	100	80,0	80,0	$80,0 \pm 0,11$
	EUL ss1	100	80,3	80,3	$80,3 \pm 0,13$	100	82,5	82,5	$82,3 \pm 0,08$
	CSD ss1/10	100	78,2	78,2	$78,3 \pm 0,11$	100	74,5	74,5	$74,5 \pm 0,19$
	CSD ss1/2	100	79,2	79,2	$79,3 \pm 0,10$	100	76,1	76,1	$76,1 \pm 0,21$
	CSD ss1	100	79,3	79,3	$79,2 \pm 0,10$	100	76,8	76,8	$76,7 \pm 0,15$
Dataset 2	FACT	93,8	50,3	53,7	$53,6 \pm 0,50$	98,7	46,7	47,3	$47,0 \pm 0,60$
	EUL ss1/10	100	77,2	77,2	$77,5 \pm 0,40$	100	78,4	78,4	$78,4 \pm 0,21$
	EUL ss1/2	100	79,4	79,4	$79,4 \pm 0,30$	100	79,9	79,9	$79,8 \pm 0,15$
	EUL ss1	100	81,0	81,0	$80,9 \pm 0,16$	100	82,0	82,0	$82,2 \pm 0,10$
	CSD ss1/10	100	78,2	78,2	$78,2 \pm 0,40$	100	73,4	73,4	$73,2 \pm 0,58$
	CSD ss1/2	100	79,6	79,6	$79,4 \pm 0,20$	100	75,2	75,2	$75,2 \pm 0,05$
	CSD ss1	100	79,9	79,9	$79,9 \pm 0,10$	100	75,4	75,4	$75,8 \pm 0,20$
Dataset 3	FACT	94,6	51,1	54,1	$53,7 \pm 0,60$	99,1	49,3	49,7	$49,4 \pm 0,60$
	EUL ss1/10	100	76,8	76,8	$76,9 \pm 0,14$	100	76,9	76,9	$76,7 \pm 0,13$
	EUL ss1/2	100	78,8	78,8	$78,8 \pm 0,21$	100	79,6	79,6	$79,6 \pm 0,12$
	EUL ss1	100	80,8	80,8	$80,8 \pm 0,14$	100	80,2	80,2	$79,9 \pm 0,14$
	CSD ss1/10	100	78,1	78,1	$78,3 \pm 0,20$	100	73,9	73,9	$73,9 \pm 0,30$
	CSD ss1/2	100	79,5	79,5	$79,5 \pm 0,14$	100	75,3	75,3	$75,0 \pm 0,25$
	CSD ss1	100	79,6	79,6	$79,6 \pm 0,12$	100	75,6	75,6	$75,6 \pm 0,12$
Dataset 4	FACT	88,6	50,8	57,3	$57,2 \pm 0,51$	97,6	51,7	53,0	$52,6 \pm 0,40$
	EUL ss1/10	100	76,4	76,4	$76,3 \pm 0,12$	100	76,3	76,3	$76,4 \pm 0,18$
	EUL ss1/2	100	77,2	77,2	$77,2 \pm 0,15$	100	76,7	76,7	$76,7 \pm 0,10$
	EUL ss1	100	77,8	77,8	$77,9 \pm 0,12$	100	78,2	78,2	$78,0 \pm 0,12$
	CSD ss1/10	100	79,9	79,9	$79,9 \pm 0,70$	100	74,2	74,2	$74,3 \pm 0,16$
	CSD ss1/2	100	80,0	80,0	$80,0 \pm 0,11$	100	74,6	74,6	$74,4 \pm 0,16$
	CSD ss1	100	78,6	78,6	$78,4 \pm 0,65$	100	74,6	74,6	$74,3 \pm 0,25$
Dataset 5	FACT	84,7	46,7	55,1	$55,0 \pm 0,50$	95,1	49,8	52,3	$52,2 \pm 0,48$
	EUL ss1/10	100	75,2	75,2	$75,2 \pm 0,10$	100	74,2	74,2	$74,2 \pm 0,18$
	EUL ss1/2	100	77,2	77,2	$77,0 \pm 0,20$	100	74,2	74,2	$74,1 \pm 0,10$
	EUL ss1	100	78,2	78,2	$78,1 \pm 0,20$	100	75,7	75,7	$75,7 \pm 0,26$
	CSD ss1/10	100	78,0	78,0	$77,9 \pm 0,10$	100	72,8	72,8	$72,9 \pm 0,15$
	CSD ss1/2	100	78,1	78,1	$78,2 \pm 0,16$	100	72,6	72,6	$72,6 \pm 0,06$
	CSD ss1	100	77,1	77,1	$77,0 \pm 0,26$	100	73,1	73,1	$73,1 \pm 0,10$
Dataset 6	FACT	81,6	45,6	55,9	$55,8 \pm 0,51$	93,1	51,9	55,7	$55,7 \pm 0,51$
	EUL ss1/10	100	77,2	77,2	$77,3 \pm 0,10$	100	75,5	75,5	$75,3 \pm 0,22$
	EUL ss1/2	100	78,3	78,3	$78,4 \pm 0,30$	100	75,2	75,2	$75,2 \pm 0,10$
	EUL ss1	100	78,7	78,7	$78,6 \pm 0,35$	100	76,3	76,3	$76,3 \pm 0,14$
	CSD ss1/10	100	78,2	78,2	$78,3 \pm 0,10$	100	72,4	72,4	$72,4 \pm 0,14$
	CSD ss1/2	100	78,5	78,5	$78,5 \pm 0,20$	100	72,3	72,3	$72,0 \pm 0,15$
	CSD ss1	100	76,9	76,9	$76,9 \pm 0,06$	100	71,8	71,8	$71,9 \pm 0,25$
Dataset 7	FACT	97,7	54,3	55,6	$55,1 \pm 0,50$	99,9	46,9	47,0	$46,9 \pm 0,60$
	EUL ss1/10	100	75,5	75,5	$75,5 \pm 0,14$	100	78,7	78,7	$78,6 \pm 0,10$
	EUL ss1/2	100	77,2	77,2	$77,2 \pm 0,25$	100	80,5	80,5	$80,5 \pm 0,18$
	EUL ss1	100	80,7	80,7	$80,8 \pm 0,10$	100	83,0	83,0	$83,0 \pm 0,17$
	CSD ss1/10	100	68,5	68,5	$68,4 \pm 0,15$	100	67,2	67,2	$67,2 \pm 0,20$
	CSD ss1/2	100	69,8	69,8	$69,9 \pm 0,20$	100	69,3	69,3	$69,2 \pm 0,10$
	CSD ss1	100	69,7	69,7	$69,7 \pm 0,10$	100	69,5	69,5	$69,4 \pm 0,18$
Dataset 8	FACT	86,1	44,9	52,3	$52,1 \pm 0,19$	87,8	39,7	45,2	$44,8 \pm 0,30$
	EUL ss1/10	100	73,5	73,5	$73,4 \pm 0,10$	100	75,6	75,6	$75,4 \pm 0,12$
	EUL ss1/2	100	74,7	74,7	$74,8 \pm 0,10$	100	77,5	77,5	$77,6 \pm 0,09$
	EUL ss1	100	78,7	78,7	$78,9 \pm 0,10$	100	81,0	81,0	$81,1 \pm 0,05$
	CSD ss1/10	100	85,1	85,1	$85,1 \pm 0,06$	100	89,9	89,9	$89,7 \pm 0,20$
	CSD ss1/2	100	87,6	87,6	$87,5 \pm 0,10$	100	91,0	91,0	$91,7 \pm 0,10$
	CSD ss1	100	88,2	88,2	$88,1 \pm 0,10$	100	91,8	91,8	$91,7 \pm 0,10$

4.3. Network Measures

As previously mentioned, the structural connectivity matrix models the human brain as a network. It is a direct mathematical way of characterizing its complex architecture. From this point of view, a wide range of graph-theoretical properties can be used to study global organizational principles or pathologies of the human brain network. One fundamental question which is addressed within this section is how sensitive these network measures are to different acquisition schemes and tractographic approaches. More precisely, the sensitivity of common network measures which are the network density, average nodal degree, global efficiency and characteristic path length were evaluated using three different tractography approaches (CSD, EUL and FACT) and eight different acquisition schemes (table 2). Furthermore, the influence of the number of reconstructed fibers as well as the influence of the number of network nodes (brain areas) on these five network measures was analyzed. It is important to note that the network measures were calculated from the unthresholded weighted structural connectivity matrices and not as usually by using adjacency matrices. This has three reasons: First the creation of an adjacency matrix needs a preprocessing step for eliminating artificial fibers. This is generally done by setting a threshold and eliminating edges with a connection strength lower than the adjusted threshold. The choice of the “right” threshold varies highly in different studies from eliminating 10% up to 80% of the edges. Second, a previous study [58] has shown that the variability in the resulting adjacency matrix is about 20% higher than in unthresholded weighted connectivity matrices. Third, the weighted connectivity matrix considers the strength of a connection and therefore it is more sensitive to pathological changes.

All structural connectivity matrices were normalized before calculating the network measures to make results from different subjects, datasets and tractography methods better comparable.

4.3.1. Network Density

The first topological network measure considered was the network density. The network density is the simplest measure and characterizes the number of inter-regional connections. The evaluation of the influences on the network density was subdivided into two parts: The influence of fiber count and the influence of the number of brain regions.

Influence of fiber count

In the first instance, we analyzed the influence of the number of reconstructed fibers on the network density. Since the results were very consistent over the two subjects, the mean network density as a function of the number of reconstructed fibers was plotted in figure 33.

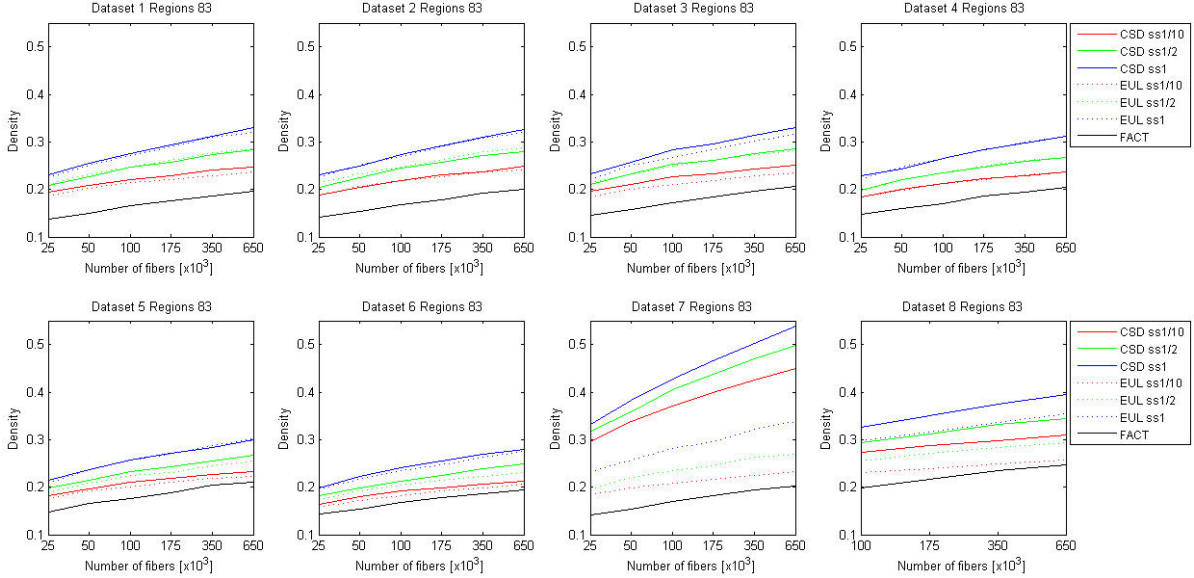


Figure 27: Network density plotted as a function of the number of reconstructed fibers averaged over both subjects. Each subfigure represents the calculated network density of the structural connectivity matrices resulting from one dataset (for further acquisition details for each dataset see table 2).

The density of all studied networks is low. This means that brain regions are only connected to few other brain regions. In a first step we will consider only the results in the first diagram. As one can see the network density is very similar for the EUL and CSD approach but differs significantly for the FACT approach. The FACT approach uses a continuously varying step size which can lead to an overshoot in highly curved regions. Furthermore, in regions where two different white matter bundles e.g. Cingulum and Corpus Callosum are directly adjacent, the high step size can lead the trajectory to go astray from the first bundle (Cingulum) to the second bundle (Corpus Callosum) (see figure 28(c)). Dataset 1 was acquired with only twelve diffusion gradient directions. Thus, only a spherical harmonic model of second order can be used for the CSD approach. A second order model can, similarly to the diffusion tensor model, only describe the fiber population within a voxel by one direction. As both algorithms are discrete

streamline propagation approaches with a fixed step size the resulting fiber tracts are similar and thus the network density is also similar. These differences in performance of the tractography are demonstrated by means of the Cingulum in figure 28. As one can see the Cingulum is reconstructed in fragments using the FACT approach and it is well and also very similarly reconstructed using the CSD or EUL approach. This confirms the decrease in network density for FACT compared to the two other approaches.

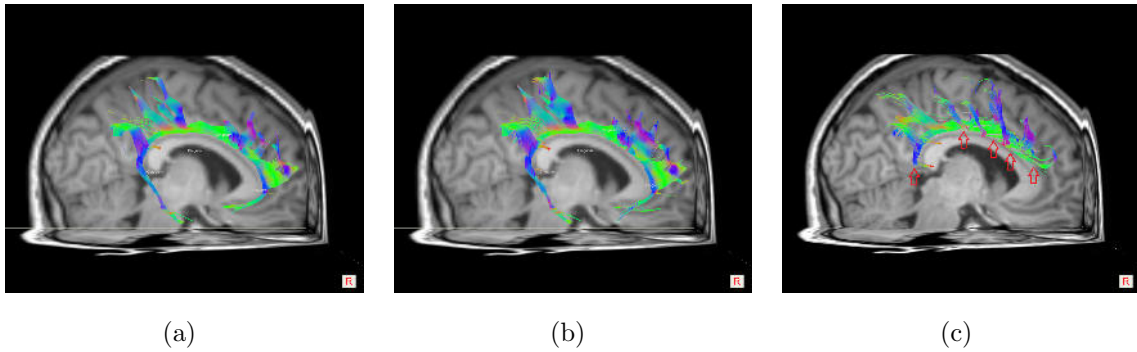


Figure 28: Differences in performance of the used tractography algorithm demonstrated on the reconstructed Cingulum. The Cingulum bundle is well reconstructed using the EUL-approach (a) and CSD-approach (b) and reconstructed in fragments using the FACT approach (c). The red arrows indicate locations where an overshoot occurs in reconstruction.

Furthermore, figure 27 shows that the tractography settings have a significant influence on the network density. An increase in step length from $1/10$ to $1/2$ leads to an increase in network density of 4%. This increase in density has two reasons. First the higher step size fans out the bundles near the white gray matter boundary resulting in more connections. Second a higher step size can cause the trajectory to go astray. This is for example the case for reconstructing the Cingulum. The Cingulum lies directly above the Corpus Callosum. If the step size is too high, an overshoot can occur so that the trajectory reaches an adjacent voxel of the Corpus Callosum bundle and continues on this way. This is illustrated in figure 29. Therefore, care should be taken using a higher step size, because not all edges are anatomical. For further discussion about anatomical and false positive connections see the subsequent section 4.5.1.

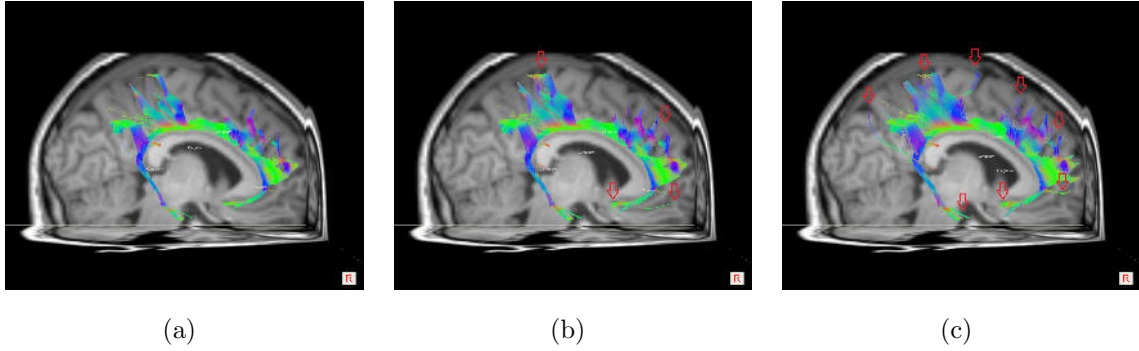


Figure 29: Influence of the step size demonstrated on the reconstructed Cingulum. The EUL approach was used for tracing and a step size of $1/10$ voxel length in (a), a step size of $1/2$ voxel length in (b) and a step size of voxel length in (c). The red arrows indicates artificial tract fibers because of an overshoot.

In addition an increase in the network density can be observed for every used tractography approach by increasing the number of fibers. The way of a reconstructed trajectory is mainly influenced by the seed point. Since it is not known where a fiber starts within a voxel, the seed points are chosen randomly within a voxel. As it is schematically presented in figure 30 a different seed point location leads to a different trajectory. Furthermore, the figure reveals that if the seed point is chosen too close to the boundary, the fiber can not be reconstructed. Increasing the number of fibers is related with an increase in the number of seed points within a voxel. Therefore, more different trajectories were reconstructed connecting different cortical areas. This explains the increase in network density.

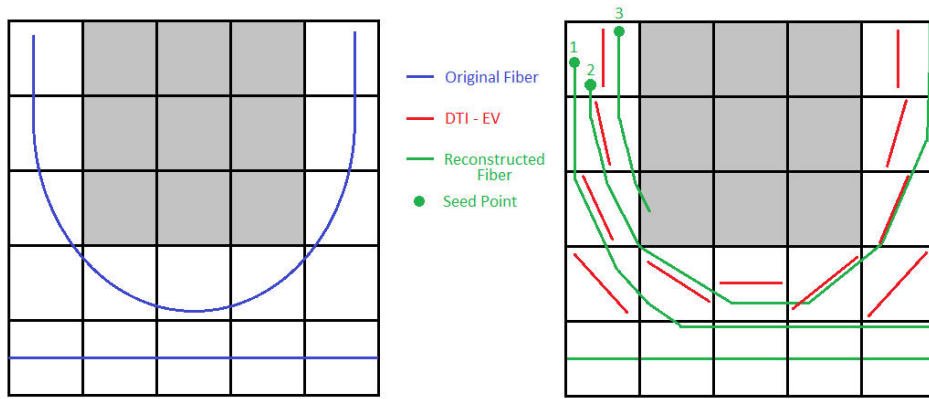


Figure 30: Schematic representation of the influence of the seed point location on the reconstructed fiber tracts. Three different locations lead to three different fiber tracts.

Figure 31 shows this influence of the seed point on fiber tracts reconstructed in the brain of subject 1. A fiber count of 25 000 means that one trajectory is reconstructed from every white matter voxel and thus a fiber count of 100 000 means that 4 trajectories are reconstructed per voxel. The red arrow indicates a position where the location of the seed points is crucial for correct streamline reconstruction.

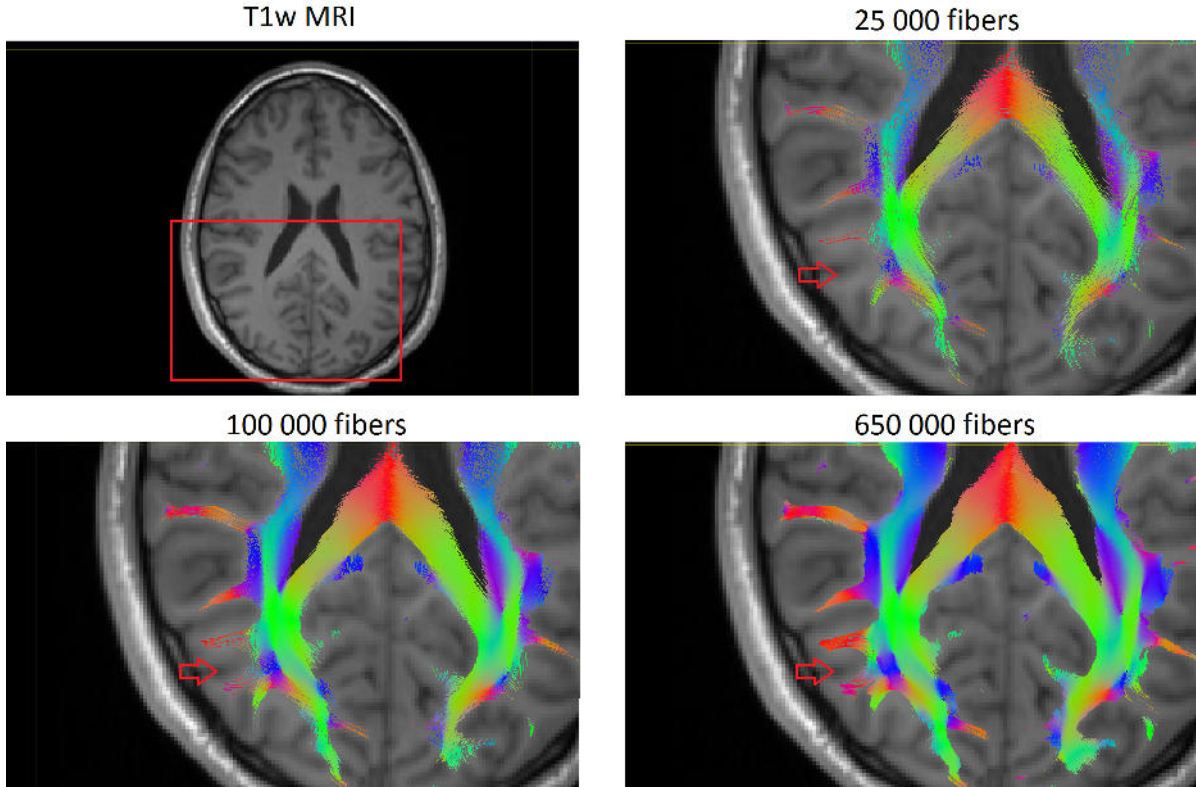


Figure 31: Influence of the number of fibers used for tractography on the network density. The more fibers are used the denser is the network. Red arrow indicates a position where the number of seed points is crucial

Taking a look now at the further diagrams in figure 27, one can observe that the network density is very similar in networks resulting from the same dw imaging modalities (diagram 1 to diagram 3). The change in b-value (dataset 3 to dataset 6) leads to a significant drop of the network density, but the trends are the same for all methods. On the one hand an increase of the b-value leads to a higher diffusion weighting and therefore to a more precise estimation of the diffusion direction but on the other hand the higher diffusion weighting leads to a higher signal attenuation and therefore to a drop in signal to noise ratio. The signal attenuation for a given b-value is given by $\exp(-bD)$. The largest diffusivity is about $1 \cdot 10^{-3} \text{mm}^2/\text{s}$ along a homogeneously aligned fiber bundle [24]. Thus, the signal attenuation for $b = 1000 \text{mm}^2/\text{s}$ (dataset 3), $b = 2000 \text{mm}^2/\text{s}$ (dataset 4), $b = 3000 \text{mm}^2/\text{s}$ (dataset 5) and $b = 4000 \text{mm}^2/\text{s}$ (dataset 6) is $S_{b1000} = \exp(-1) = 0.37$, $S_{b2000} = \exp(-2) = 0.14$, $S_{b3000} = \exp(-3) = 0.05$ and $S_{b4000} = \exp(-4) = 0.02$. Therefore, the diffusion weighting signal for a b-value of $4000 \text{mm}^2/\text{s}$ is only 2% of the non diffusion weighting signal. Furthermore, the SNR is 20 times lower in acquired datasets

using a b-value of $4000\text{mm}^2/s$ compared to a b-value of $1000\text{mm}^2/s$. Due to this high drop in SNR, the noise becomes a limiting factor for fiber tracing, especially for long fibers. This explains the drop in network density by increasing the b-value.

An increase in the gradient direction from 12 to 64 (dataset 7) allows to describe the fiber population within a voxel with a spherical harmonic model of eighth order for the CSD approach. This higher order model can resolve crossing and kissing fibers within a voxel (figure 32) resulting in a denser network. The increased number of gradient directions shows no change in the network density for the two tractography models based on diffusion tensor. This is obvious, because a diffusion tensor always describes the diffusion within a voxel with a single direction. Thus, an increase in gradient directions only leads to an increase in SNR.

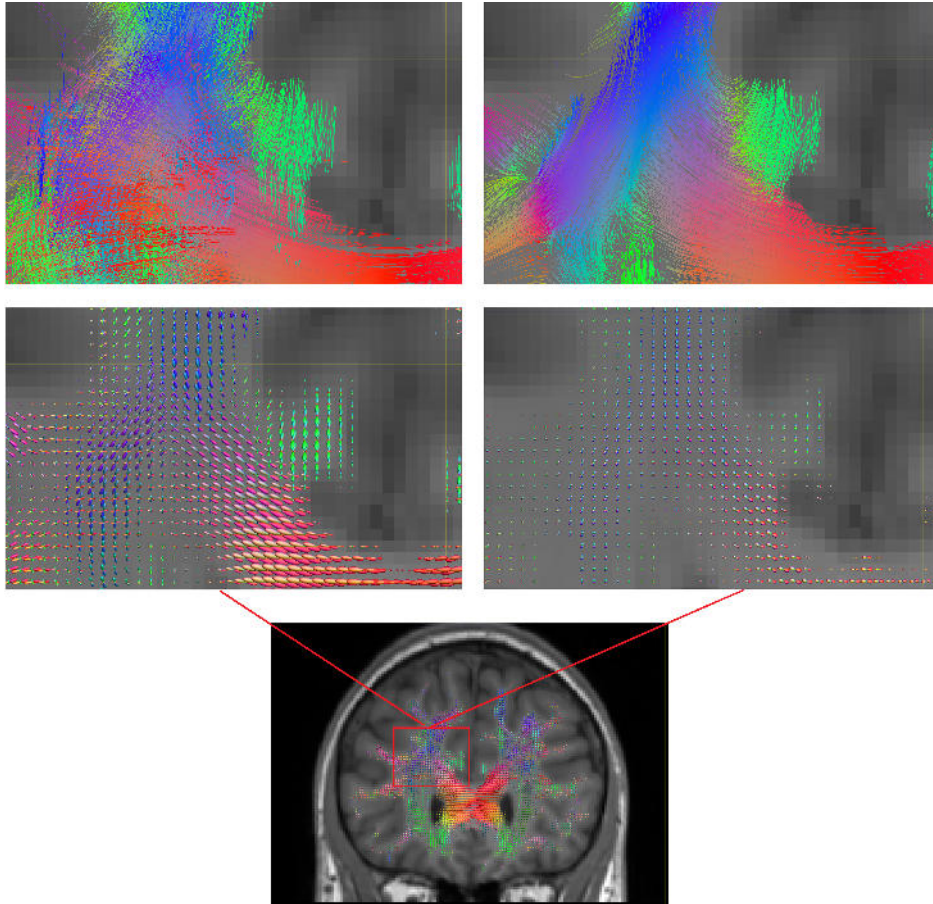


Figure 32: Spherical harmonic model of eighth order for 64 gradient directions on the left side and spherical harmonic model of order two for 12 gradient directions on the right side. The higher order model allows resolving crossing and kissing fibers within a voxel. Thus, fibers can go in different directions through a voxel connecting more cortical areas than the model of second order.

In figure 27 we see that an increase in the spatial resolution (dataset 8) leads to an increase in the network density for all methods. As already shown in figure 26 in the previous section, an increase in the spatial resolution is beneficial in regions where partial volume effects prevent the fiber tracing. Partial volume effects occur if different tissue types are present within a voxel. This is for example the case in the gray-white matter boundary or in regions where tracts are very thin. This decrease in voxel size allows to reconstruct thin tracts much better than for a higher voxel size and it leads to an increase in cortical connections and therefore to a denser connectome. However, it comes

with lower SNR and longer acquisition times.

Influence of the number of regions

In a second step, the influences of the number of regions on the network density were analyzed. Here again, all results were very consistent over both subjects, and therefore the averaged network density as a function of the number of nodes is illustrated in figure 33. Since the previously explained performance differences of the tractography algorithms remain the same for different scales, only the impacts of the nodal scale are discussed.

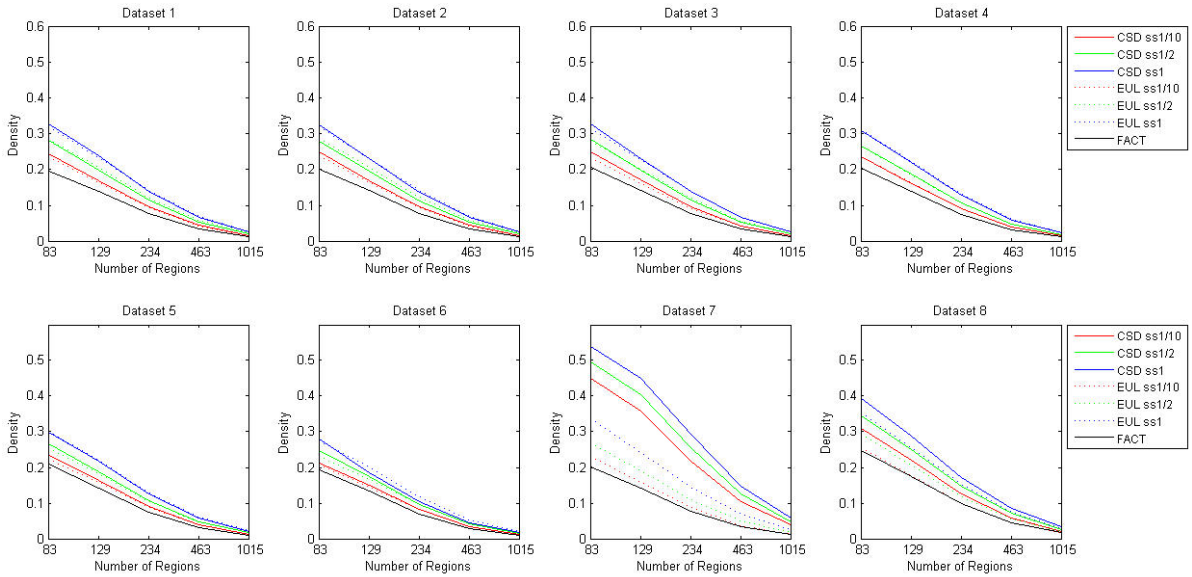


Figure 33: Network density plotted as a function of network nodes averaged over both subjects. Each subfigure represents the calculated network density of the structural connectivity matrices resulting from one dataset (for further acquisition details for each dataset see table 2).

The network density in general decreases with increasing number of nodes resulting in sparse matrices at the highest scale. This shows that white matter bundles in the human brain only connect a few regions. Furthermore, the white matter bundles are very compact and terminate only in a small cortical area. Therefore, an increase in the number of nodes leads to many unconnected regions. This is illustrated in figure 34 using as example a part of the Corpus Callosum. This part connects the precentral gyrus of the left hemisphere with the precentral gyrus of the right hemisphere. As can be seen in this figure, this fiber bundle connects only two region at all scales. Thus, many disconnected

nodes exist resulting in a sparse structural connectivity network and in a drop of the network density. The network density is only 3 to 4% and therefore reduces the statistical power of a group-wise study. However, this example in figure 34 demonstrates one beneficial effect of using a higher nodal scale. Due to the smaller cortical area it is more sensitive to pathological changes and allows a more precise localisation.

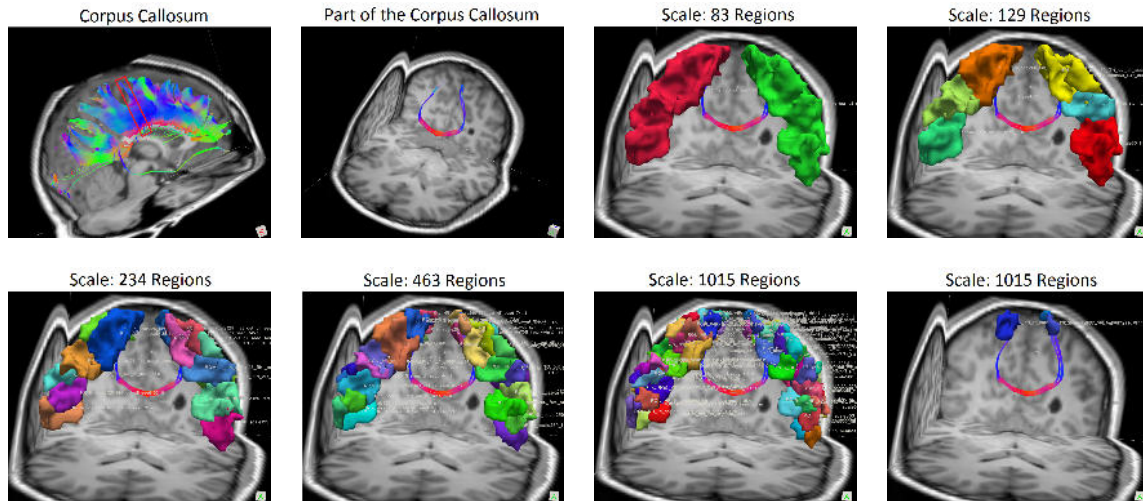


Figure 34: Influence of number of nodes on the network density demonstrated with a part of the Corpus Callosum (b). This part of the Corpus Callosum connects the precentral gyrus of the left hemisphere with the precentral gyrus of the right hemisphere (c). In every resolution the part of the Corpus Callosum is only connected by a single region of the precentral gyrus.

It is important to note that the network density has a high influence on all subsequent network measures. Therefore, results from different tractography algorithms as well as from different datasets can not be compared directly, but under consideration of the network density.

4.3.2. Nodal Degree

The second network measure considered is the average nodal degree. The nodal degree is strongly associated with the network density and describes the number of connected neighbouring nodes averaged over all nodes. The evaluation of the influences on the average nodal degree was subdivided into two parts: The influence of fiber count and the influence of the number of brain regions.

Influence of fiber count

In a first step, the impact of the fiber count on the nodal degree of the structural connectome was investigated. The average nodal degree as a function of the fiber count averaged over both subjects is illustrated for all methods and datasets used in figure 35. Since the trends are the same for different connectome scales, the average nodal degree is only illustrated here for scale 83.

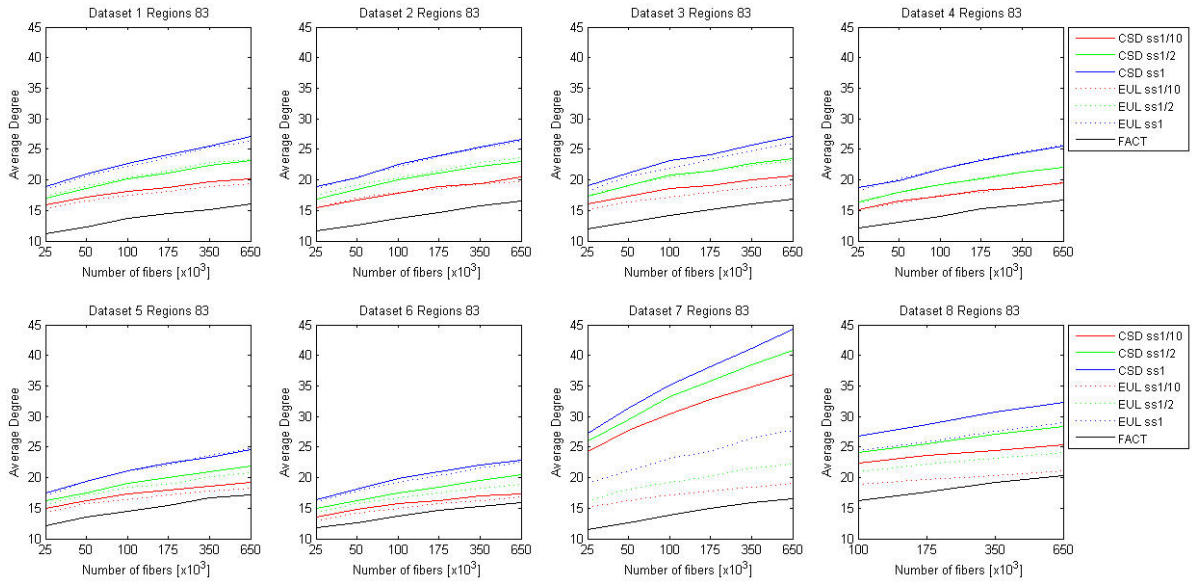


Figure 35: Average nodal degree of the structural network plotted as a function of the number of reconstructed fibers averaged over both subjects. Each subfigure represents the calculated average nodal degree of one dataset (for further acquisition details for each dataset see table 2). Note the different scales on the y-axis

Considerations in the first diagram (dataset 1) show that the average nodal degree is similar in networks generated with the EUL or CSD approach and lower in networks generated with the FACT approach. A higher nodal degree indicates a higher communication between network nodes. Therefore, a higher average nodal degree is always accompanied with a denser connectome. As already described in detail in the previous section, the density in structural networks generated with the EUL or CSD approach is significantly higher than in networks generated with the FACT approach and consequently the nodal degree is also higher. The same can be observed in networks generated with a higher step size and fiber count.

Networks generated from datasets acquired with similar imaging modalities (dataset 2 and 3) show similar results. The average nodal degree decreases by 3% in networks generated from higher b-value. As explained previously, the noise is a limitation factor for tractography and long fiber tracts were not longer reconstructed leading to a lower number of connections between brain regions. Furthermore, the nodal degree in networks generated from the high resolution dw MRI (dataset 8) is significant higher. Again, this is due to lower partial volume effects, which allows the reconstruction of small fiber tracts leading to new connections which are absent in other datasets.

Influence of the number of regions

Additionally the impact of the number of regions on the nodal degree of a network is analyzed. Here again, the nodal degree was averaged over both subjects. The results for every dataset and method as a function of the number of nodes are illustrated in figure 36.

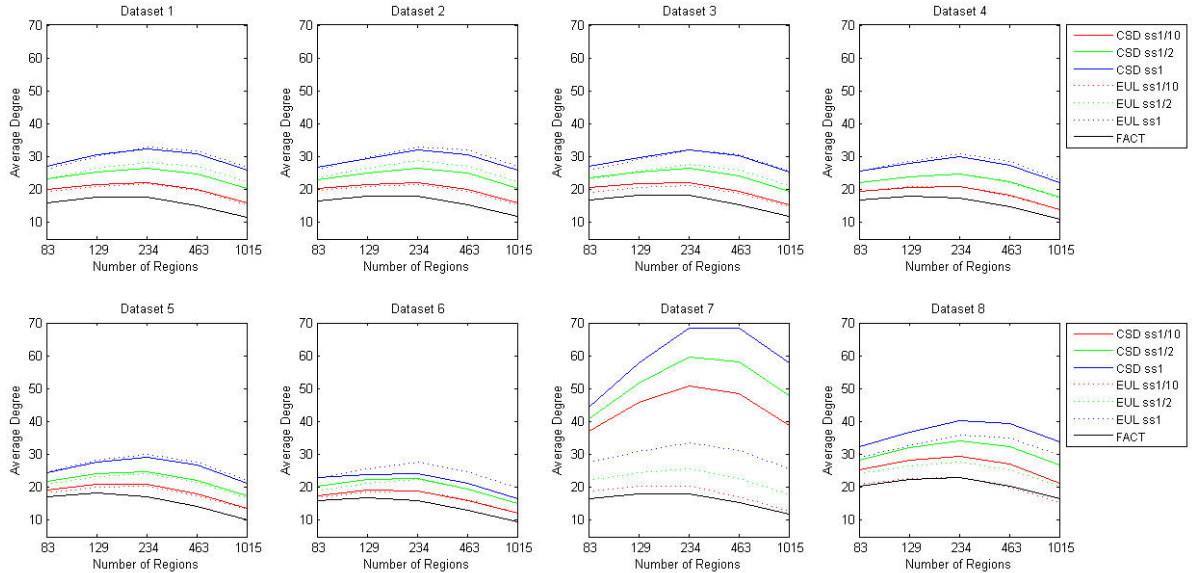


Figure 36: Average nodal degree of the network plotted as a function of network nodes averaged over both subjects. Each subfigure represents the calculated averaged nodal degree of one dataset (for further acquisition details for each dataset see table 2).

As can be seen in figure 36, the trends of the average nodal degree are similar over all datasets. Since the differences in the average nodal degree resulting from different

tractography methods and datasets were already discussed above, only the differences of different scales are considered now.

An increase of the number of nodes means that one parcel of the lowest resolution is subdivided into a few parcels leading to a higher scale. Since the original connection between the two parcels still remains, a subdivision always leads to an equal or higher number of connections. For example a tract which branches out near the gray-white matter boundary terminates in the whole parcel. Therefore, a subdivision of this parcel is accompanied by an increase in the nodal degree or number of edges. This is illustrated for a part of the Inferior Front-occipital Fasciculus in figure 37. One may now expect that the average nodal degree for all generated structural connectivity networks should increase. This is the case until a scale of 234 nodes. At higher scales the average nodal degree decreases. This can be observed for all different combinations in figure 36. The drop in the nodal degree is caused by a combination of two effects, first by averaging over all nodes in the network and second by the sparsity of the network. As previously demonstrated, the network density is about 3% for the highest scale, which means that 970 000 edges had a nodal degree of zero. Due to the averaging process these zero edges overshadow the increase of the nodal degree. This highlights additionally that the number of nodes has a great influence on the network indices.

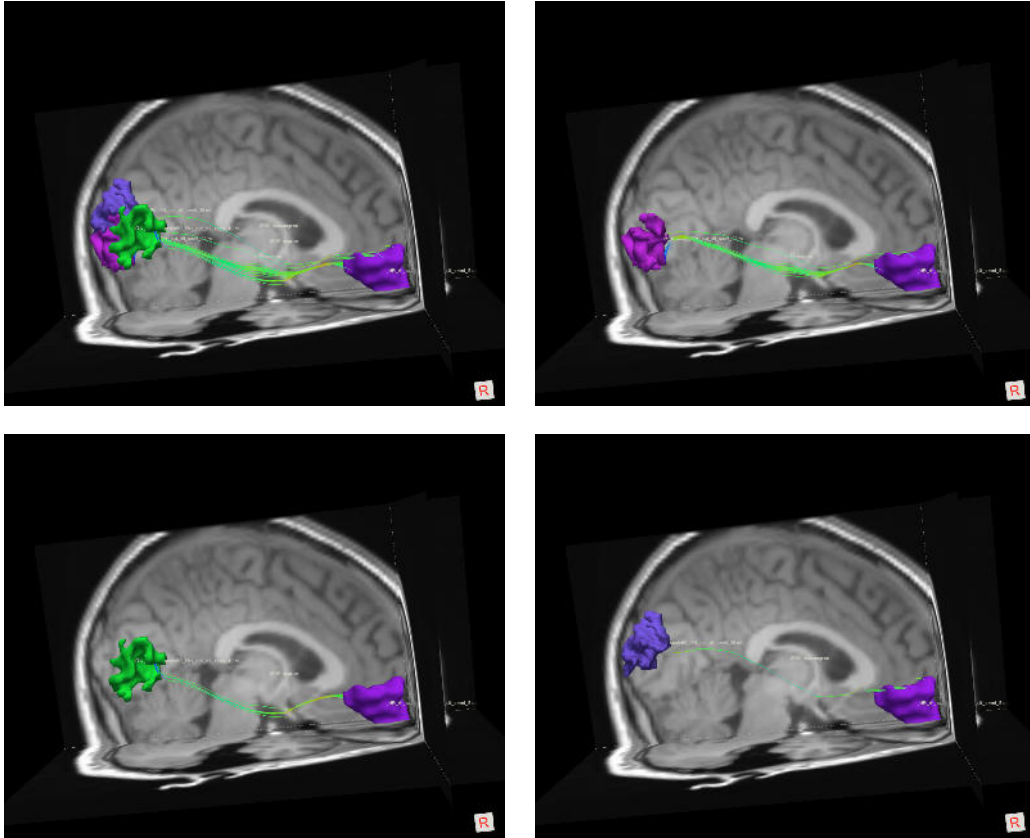


Figure 37: Influence of number of nodes on the nodal degree. Illustrated on a part of the Inferior Fronto-occipital Fasciculus

4.3.3. Characteristic Path Length

The next network measure investigated was the characteristic path length. The path length describes the shortest way to reach a node in the network and is therefore strongly associated with the network density. The characteristic path length is the mean of the shortest path length of a network. The evaluation of the influences on the characteristic path length was subdivided into two parts: The influence of fiber count and the influence of the number of brain regions.

Influence of fiber count

At first, the impact of the fiber count on the characteristic path length of the structural connectivity network was investigated. Here again, the averaged char. path length over both subjects is illustrated as a function of the fiber count in figure 38. Since the

results are similar over different connectome scales the characteristic path length is only illustrated for scale 83.

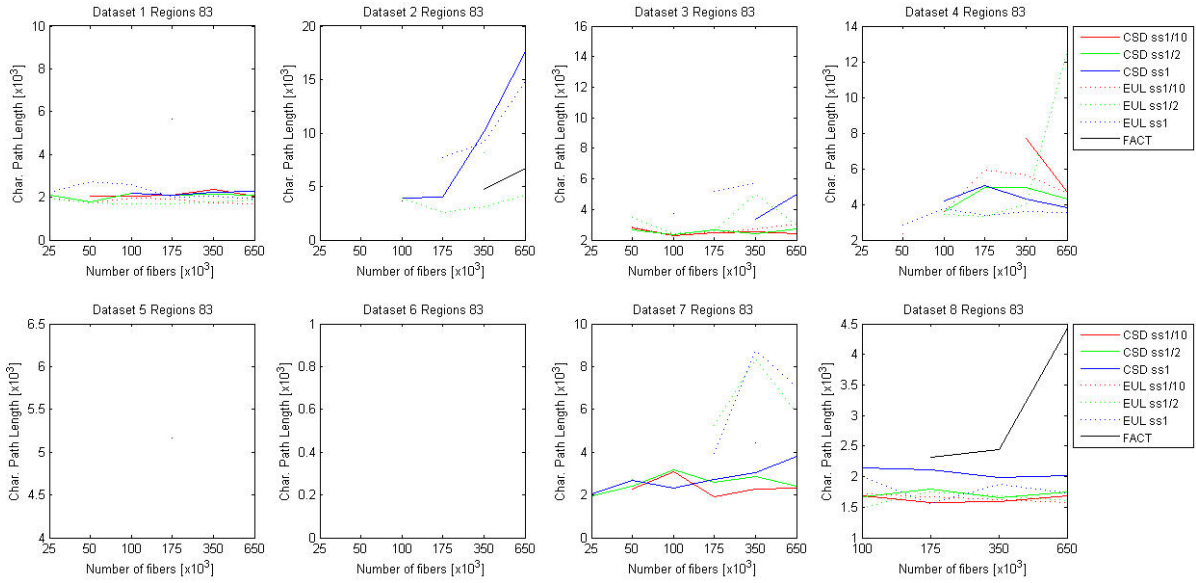


Figure 38: Characteristic path length of the network plotted as a function of the number of reconstructed fibers of subject 2. Each subfigure represents the calculated char. path length of one dataset (for further acquisition details for each dataset see table 2). Note the different scales on the y-axis

The characteristic path length serves as indicator for a connected network. Only if every node in the network has at least one connection to another node, the characteristic path length is a meaningful measure, otherwise it is infinite. Since the 83 cortical and subcortical regions at the lowest scale are from anatomical origin with a known function, a connected structural network should exist. Considerations about figure 38 show that for most approaches a connected network only exists if at least 100.000 fibers were used for fiber tracing. This again is due to the low number of seed points and the used seeding strategy. Our observations show that in most cases the entorhinal cortex in the left or right hemisphere is not connected. This is a small cortical area located in the medial temporal lobe. One known connection to this area is the Cingulum. Since it is a small white matter bundle, partial volume effects play a major role in the reconstruction, leading to an early termination for low resolution datasets as illustrated in figure 39. Furthermore, it is conspicuous that the structural networks generated with the FACT-approach are only connected networks if a high-resolution dwMRI (dataset 8) or 650.000

fibers are used (figure 40). In dataset 5 and 6 no tracing-algorithm was able to create a connected structural network due to the low SNR.

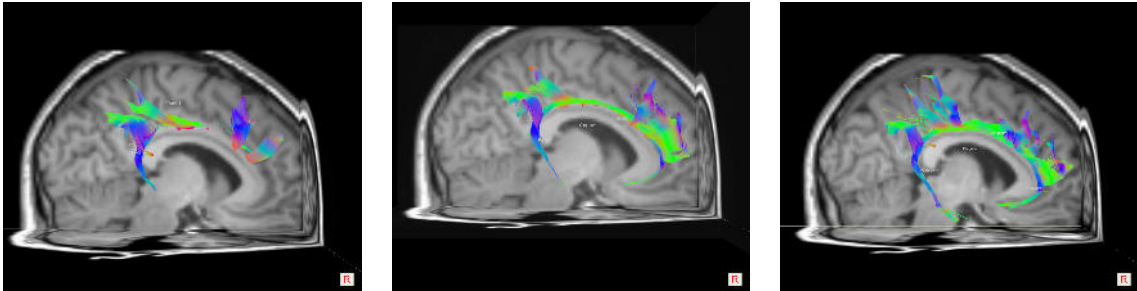


Figure 39: Cingulum reconstructed using EUL-approach and dataset 6 in figure (a), dataset 7 in figure (b) and dataset 8 in figure (c)

Influence of the number of regions

In a second step, the influences of the number of regions on the char. path length of the structural network were analyzed. Here again, all results were very consistent over both subjects, and therefore the averaged char. path length as a function of the number of nodes is illustrated in figure 33.

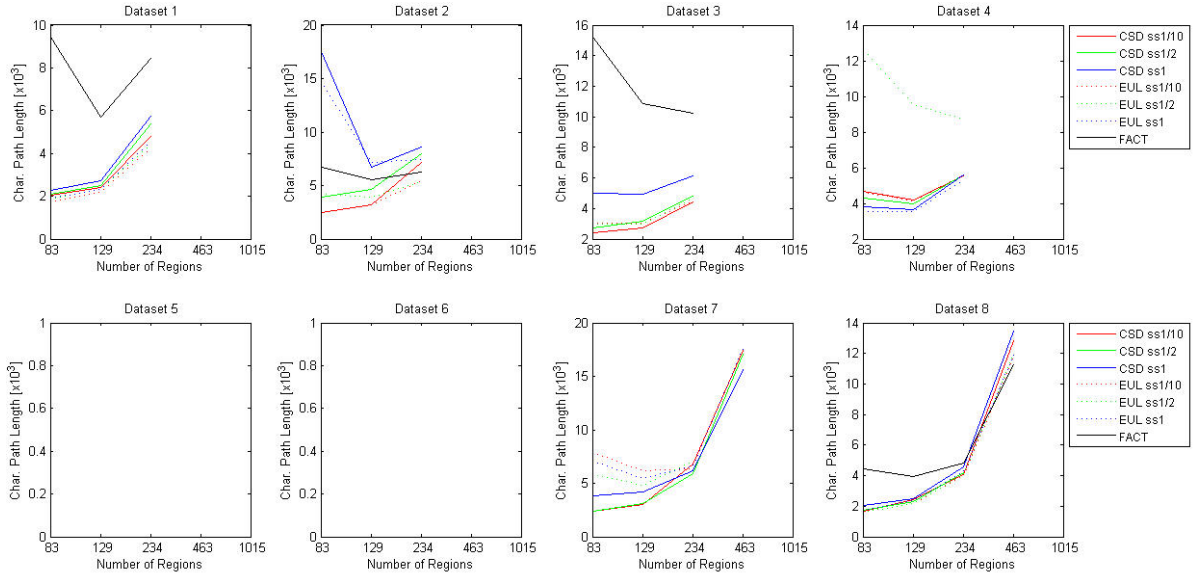


Figure 40: Characteristic path length of the network plotted as a function of network nodes of averaged over two subjects. Fiber count used for reconstruction was 650.000. Each subfigure represents the calculated char. path length of one dataset (for further acquisition details for each dataset see table 2). Note the different scales on the y-axis

Structural networks generated with FACT show in general a higher char. path length than networks generated with EUL and CSD. Furthermore, the char. path lengths of EUL and CSD are very consistent. The char. path length is mainly influenced from “long” connections, which can in this case be interpreted as weak connections consisting of only a few tracts. If a few of these weak connections exist, the char. path increases dramatically. Therefore, it seems that structural connectivity matrices created with FACT algorithm have more weak connections than the networks generated with the other two approaches. Furthermore, in figure 40 it is recognizable that the char. path length is much lower using a high-resolution dw MRI (dataset 8). This means that networks generated with this dataset provide more balanced edges than networks generated from other datasets. As before, the char. path length for dataset 5 and 6 is infinity, because of the low SNR not all long fiber tracts were reconstructed correctly.

As shown above, an increase in the number of network nodes leads to an increase in the nodal degree. Therefore, connections between two nodes were split up leading to a lower connection strength or weight. On the basis of this increase of weak connections in the structural network, the char. path length increases with a higher nodal scale.

Figure 40 indicates that structural networks generated with high-resolution dwMRI (dataset 8) are connected networks until a scale of 463 nodes, whereas structural networks generated with conventional dwMRI (dataset 1-7) are only connected networks until a scale of 234. The only exceptions are networks generated with the multi-direction fiber tracking approach (CSD). Here again, this is due to the fact that crossing and kissing fibers can be reconstructed leading to a denser and well-connected structural connectome.

4.3.4. Global Efficiency

The last network measure considered was the global network efficiency. The global efficiency is the inverse char. path length averaged in the structural network. Here, the evaluation of the influences on the global efficiency of a structural connectivity network was subdivided into two parts: The influence of fiber count and the influence of the number of brain regions.

Influence of fiber count

At first, the impact of the fiber count on the global efficiency of a structural connectivity network was investigated. Once again, the results were very consistent over both subjects and the averaged global efficiency as a function of the number of fibers is shown in figure 41.

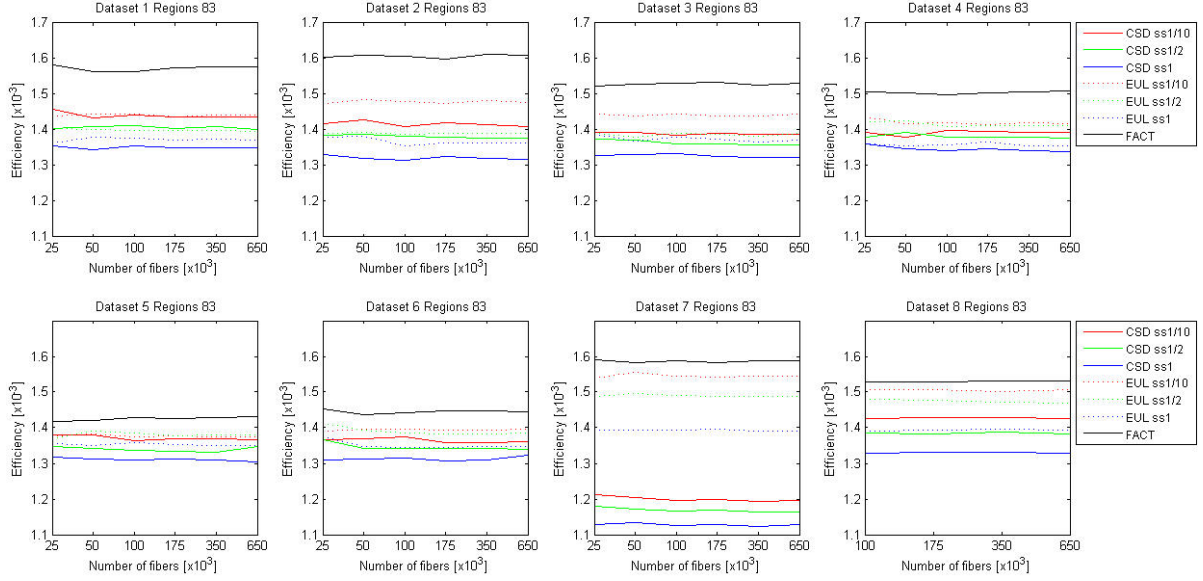


Figure 41: Global efficiency of the network plotted as a function of the number of reconstructed fibers averaged over both subjects. Each subfigure represents the calculated global efficiency of one dataset (for further acquisition details for each dataset see table 2). Note the different scales on the y-axis

The global efficiency of a structural network is mainly influenced by short paths. Short paths are, in this context, strong connections between a pair of nodes. When taking a look at diagram 1 in figure 41, it can be seen that structural networks generated with the FACT approach are most efficient. This has two reasons. Firstly, the network density in FACT networks is much lower compared to the CSD and EUL networks leading to stronger connections or higher weights. Secondly, as has already been observed for the char. path length, the networks for CSD and EUL are more balanced regarding the edge-weight. This means that these networks have many moderate edge weights, and only few strong and weak edges. The networks generated with EUL and CSD approach have a similar efficiency. The drop in the global efficiency for networks generated with a higher step-size is a result of the increased network density. As noted above, a higher network density means more edges and therefore a lower weight between edges. Increasing the number of fibers does not have a substantial impact on the global efficiency. This is obvious because the strongest and densest connections were already reconstructed with a low number of seed fibers.

If we take a look now at the results using similar dwMRI datasets (diagram 2,3), similar trends can be observed. Thus, the global efficiency is a very robust network measure. A

decrease in the global efficiency can be observed for using higher b-value dwMRI (diagram 4-6). Noticeable is the drop in efficiency if a dataset with more diffusion gradient directions (dataset 7) is used in combination with a CSD approach for generating the structural connectome. This multi-direction fiber model creates a much denser connectome with about twice as much edges compared to networks generated with other approaches. By using the same number of fibers, the edges in this network are much weaker, which explains the drop.

As seen before for the path length, the efficiency of the structural networks generated from high-resolution dwMRI is slightly lower than for networks generated from conventional dwMRI. This indicates a more balanced connectome regarding the edge-weight, with many moderate connections and only a few weak and strong connections.

Influence of the number of regions

In a second step, the influences of the number of regions on the global efficiency of the structural network were analyzed. All results were again very consistent over both subjects, and therefore the averaged global efficiency as a function of the number of nodes is illustrated in figure 33.

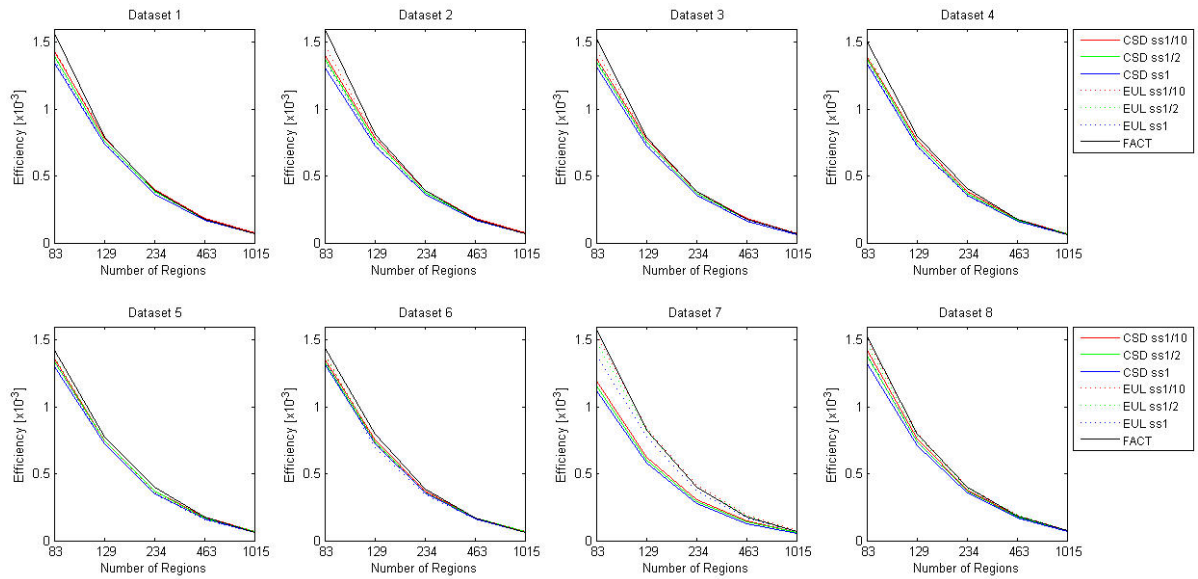


Figure 42: Global efficiency of the network plotted as a function of network nodes averaged over both subjects. Each subfigure represents the calculated global network efficiency of one dataset (for further acquisition details for each dataset see table 2).

As can be seen in figure 42, the trends of the average nodal degree are similar over all datasets. Since the differences in the global efficiency of structural networks resulting from different tractography methods and datasets were already explained above, only the differences over different scales are considered.

An increase in the number of nodes is accompanied by an increase in the number of edges within a network. Holding the strength of network constant, which is in this context the number of fibers, and increasing the number of nodes simultaneously the strength between the edges decreases. The result is an increase in the global efficiency of a network. This explains the drop in network efficiency which can be observed in figure 42. This curve progression shows as well that the number of nodes has a major impact on network measures. This should be considered when comparing network indices from different studies.

4.4. Robustness

Since the aim of structural connectivity is to study similarities and differences in groups of subjects it is essential that the methods used for estimating the structural connectivity matrices are robust and that the results are reproducible. Otherwise, the variability in the structural connectivity matrices occurring from inexact mapping methods or acquisition schemes can highly influence the accuracy of studies or even alter results in group comparisons. Therefore, the intra-subject as well as the inter-subject variability of the raw connectivity matrices was evaluated for each tractography method.

4.4.1. Intra-subject variability

The intra-subject variability describes the variability of the structural connectivity in the same subject. It was tested in a two step-procedure.

4.4.1.1. Same scans processed twice

In the first step, the eight acquired datasets were processed twice for both subjects in order to evaluate the robustness of the complex processing pipeline. As the same dataset is used, one may expect that the same structural connectivity matrices would result. In order to check this, the Pearson correlation coefficient between each entry

of the two resulting raw connectivity matrices was calculated. The resulting correlation coefficients of subject 1 as a function of the number of nodes and tractography algorithm are illustrated in figure 43.

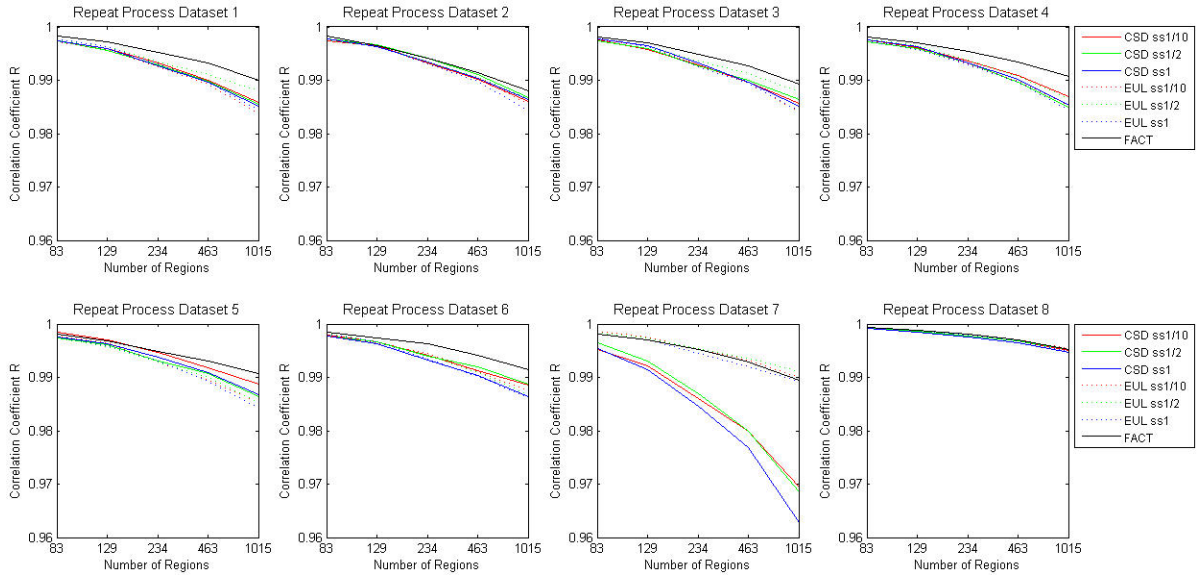


Figure 43: Intra-subject variability processing the same dataset of subject 1 twice as a function of the number of nodes and tractography algorithm. Each sub-figure shows the results for one acquired dataset (see table 2 for further explanations).

Figure 44 shows the resulting correlation coefficients as a function of the number of nodes and tractography algorithm of subject 2. This offers the same trends for the correlation coefficient as for subject 1.

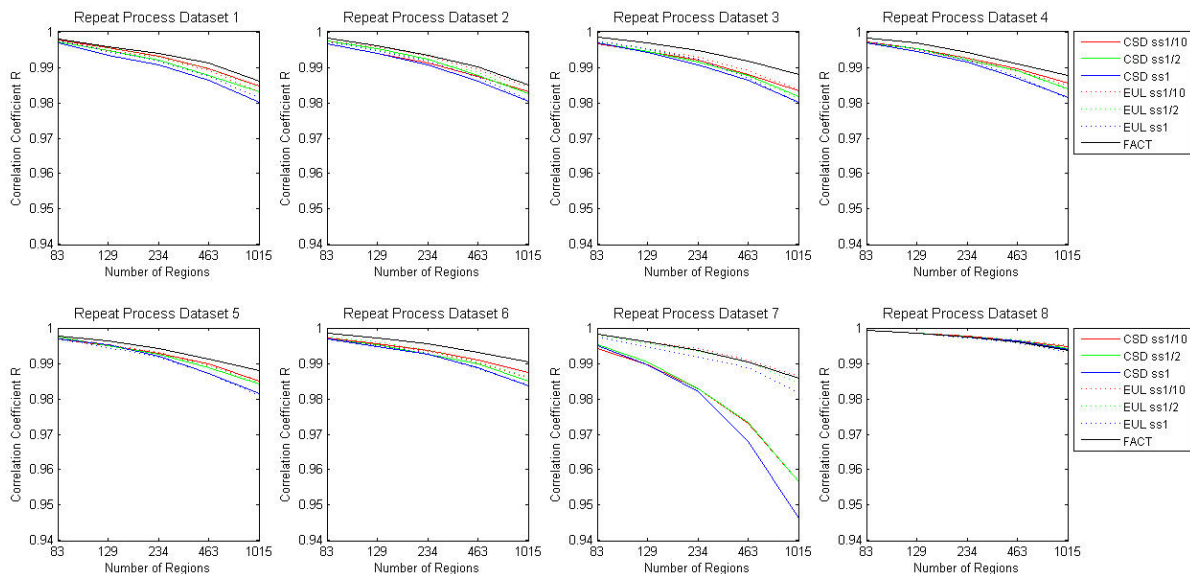


Figure 44: Intra-subject variability processing the same dataset of subject 2 twice plotted as a function of the number of nodes and tractography algorithm. Each subfigure shows the results for one acquired dataset (see table 2 for further explanations).

The resulting connectivity matrices from reprocessing the same datasets are highly correlated, but not exactly the same. This is due to the fact that the seed points for tractography are placed randomly within a voxel. As previously shown in figure 30, this has an influence on the reconstructed fibers and also on the generated structural connectome. The correlation coefficient decreases linearly with increasing number of regions and ranges between 0.993 for the lowest scale (83 regions) and 0.945 for the highest scale (1015 regions) with corresponding p -values < 0.01 . This is obvious, because at the highest scale the parcels have a surface of 1.5cm^2 and therefore the influence of the randomly placed seed points is much higher compared to lower scales. The FACT algorithm shows the highest stability for all datasets. A drop in the correlation coefficient occurs if the gradient directions are increased from 12 to 64 using the CSD approach for fiber tracing. This is due to the randomly placed seed points, which have a much higher influence on crossing fibers, because they can go two or more ways rather than one within a voxel. As may be expected, increasing the number of gradient directions has no influence on the repeatability for the two DTI approaches. Furthermore, a small drop in the correlation coefficient can be observed for higher step sizes. This is due to the fact that the reconstructed fibers fan out near the white-gray matter boundary leading

to a higher variability. Dataset 8 with the highest spatial resolution shows the highest correlation coefficient but in general all used methods are very stable for all datasets, with a minimal correlation coefficient r of 0.947.

4.4.1.2. Same subject scanned twice

Since the processing pipeline is very stable regarding reproducibility, the influence of the acquisition method was analyzed in a second step. Therefore, the same subject was scanned twice with exactly the same imaging parameters. Additionally, a third MRI was acquired with different imaging parameters (see table 2 for further details), which may be an issue if researchers pool together differently acquired diffusion datasets. The three acquired datasets for each subject were processed independently resulting in 3 connectivity matrices. As before, the Pearson correlation coefficient between the connectivity matrices for every possible combination (dataset 1 and dataset 2, dataset 2 and dataset 3, dataset 1 and dataset 3) was calculated resulting in 3 diagrams for each subject.

Influence of fiber count

Since the trends remain the same for different scales, the influence of fiber count on the repeatability is only shown for scale 83 in figure 45 for both subjects.

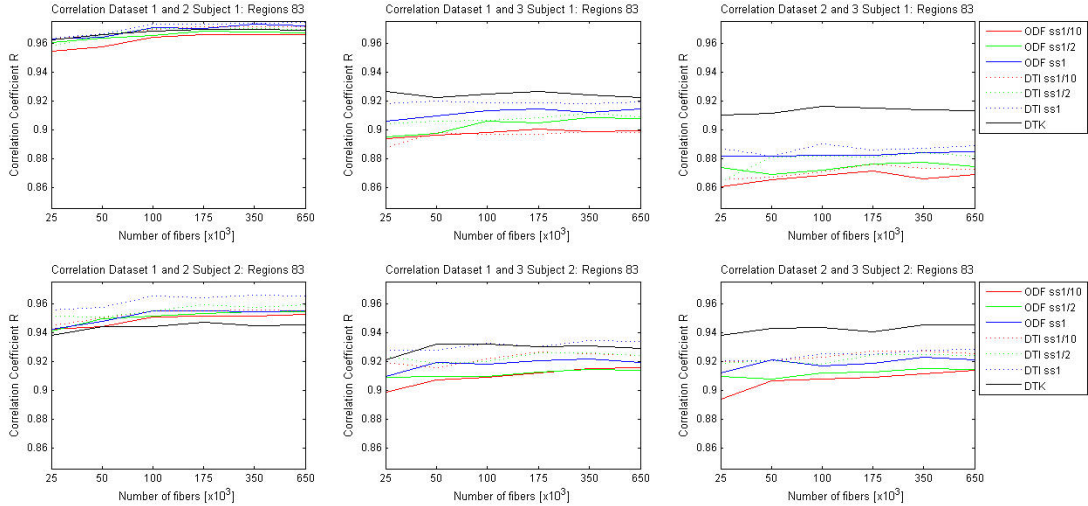


Figure 45: Pearson correlation coefficient plotted as a function of number of fibers and different tractography algorithms. First row shows results from subject 1 and second row from subject 2.

The number of fibers has no considerable impacts on the reproducibility. One should take care when comparing these results with the results of section 4.2, because for calculating the Pearson correlation only valid fibers can be used. In this context the FACT-algorithm is the most stable approach for different imaging parameters. This means that the connections which are reconstructed using the FACT approach are very robust. In contrast, the CSD-approach seems to be less robust, because the spherical harmonic coefficients are directly estimated from the raw-diffusion signal and therefore noise has the most influence.

An increase in the step-length leads to a higher correlation coefficient and therefore to a higher reproducibility for both fixed step size approaches. A longer step size means that the trajectory reaches the termination point faster and thus the chance to go astray is lower compared to a smaller step size.

Influence of the number of regions

Figure 46 shows the calculated Pearson correlation coefficient as a function of the number of brain nodes for both subjects.

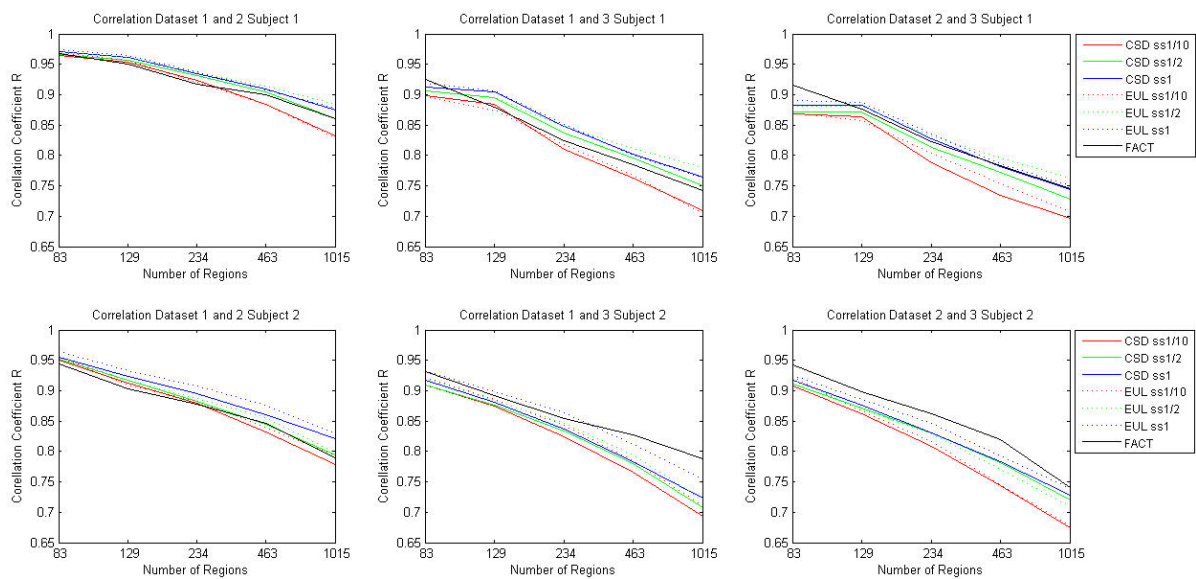


Figure 46: Pearson correlation coefficient plotted as a function of number of nodes for different tractography algorithms. First row shows results from subject 1 and second row from subject 2.

The results in figure 46 also show a high correlation for every pair of resulting connectivity matrices. The correlation-coefficient ranges from 0.87 for the lowest scale to 0.68 for

the highest scale with a p-value < 0.01 . Comparing these results with the results of the previous section (figure 43 and 44) a high drop in the correlation coefficient can be found. This is due to the disturbances of the MR acquisition, noise, susceptibility artefacts and head motion of the patient. These factors have a great impact on the streamline results leading to different tracts through the brain. It is obvious that the variability increases with increasing number of brain regions because at the highest scale (1015 regions) small deviations of the streamline trajectories lead to different connections of brain regions. Here again the FACT approach is the most robust and the CSD approach is the least robust method but generally all methods are very robust over all scales.

4.4.2. Inter-subject variability

The inter-subject variability describes the variability of the structural connectivity over different subjects. It is already known from several post mortem studies that brain size, locations of the cortical regions and cortex folding structure is not equal over subjects. For a group-wise comparison it is a very important condition that the variability between the structural connectomes is lower than the sensitivity of a pathological disease in order to get meaningful results. Therefore, inter-subject variability was analyzed by calculating the Pearson correlation coefficient between the raw connectivity matrices of the two subjects. This was done for every acquired dataset in all scales as well as for different numbers of reconstructed fibers to establish which shows the lowest variability.

Influence of fiber count

Figure 47 shows the inter-subject variability for each dataset as a function of the number of reconstructed fibers. Since trends remain the same over different scales the results are only shown for scale 83.

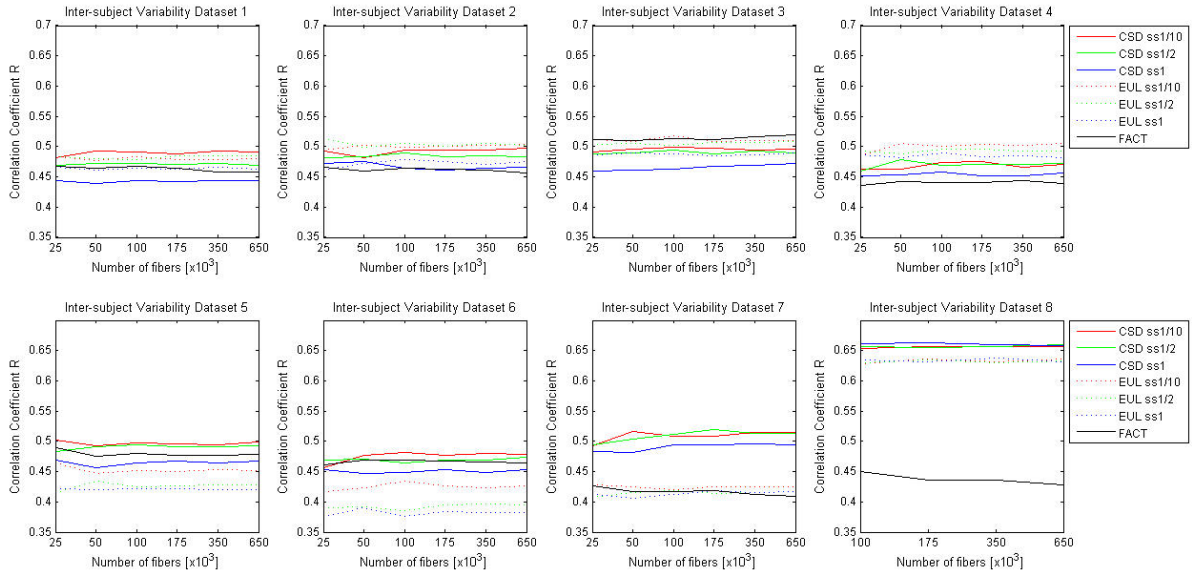


Figure 47: Correlation coefficient plotted as a function of the number of reconstructed fibers for 83 brain regions. Each subfigure shows the resulting inter-subject variability for every acquired dataset (see table 2 for further explanations)

The number of reconstructed fibers did not considerably influence the correlation coefficient. The correlation coefficient is similar using datasets with the same spatial resolution, same b-value and same number of diffusion gradients. This is illustrated in the first three diagrams of figure 47. An increase in the b-value (dataset 3 to dataset 6) implicates a lower SNR. As a consequence noise affects the reconstructed fibers and the correlation coefficient decreases.

An increase in the number of diffusion gradients from 12 (dataset 1,2,3) to 64 (dataset 7) results on the one hand in a drop of 5% in the correlation coefficient for the two DTI approaches and on the other hand in a rise of 5% in the correlation coefficient for the CSD approach. This increase is obvious because a spherical harmonic model of order eight was taken, which reconstructs kissing and crossing fibers very well and therefore reduces the inter-subject variability.

A significant increase in the correlation coefficient can be observed in the high resolution dwMRI (dataset 8) for the CSD and EUL approach. A higher resolution implicates lower partial volume effects and therefore small tracts can be reconstructed pretty well in both subjects leading to a lower inter-subject variability.

Influence of the number of regions

Figure 48 shows the inter-subject variability for each dataset as a function of the number of reconstructed fibers.

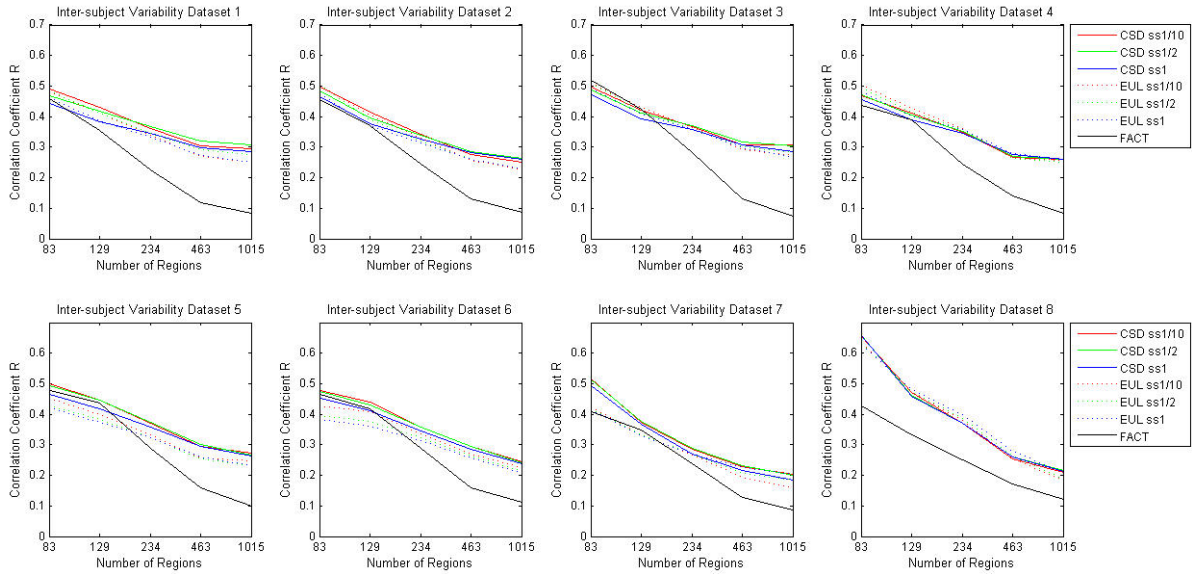


Figure 48: Correlation coefficient plotted as a function of the number of brain regions. Each subfigure shows the resulting inter-subject variability for every acquired dataset (see table 2 for further explanations)

In figure 48 it is shown that the correlation-coefficient decreases with increasing number of nodes, from 0.65 for the lowest scale down to 0.08 for the highest scale. As previously described, the connectivity matrices generated from high resolution dwMRI (dataset 8) show the highest correlation. When comparing these correlation coefficients with the previously calculated intra-subject correlation coefficients a high drop of 30-50% can be observed. This high drop can be explained by biological fluctuation of the brain. No brain equals another and the variability between subject 1 and 2 with regard to the brain size, shape and volume as well as the variability of the cortex folding structure is shown in figure 49. These fluctuations often lead to the case that the same white matter tract originates or terminates in one of the neighbouring nodes of these subjects. This leads to different structural connectivity matrices and therefore to a decrease in the correlation coefficient. A lower intra-subject than inter-subject variability is an important condition for group-wise studies, otherwise the instability of the used methods can pretend significant differences in the structural connectivity of these groups but of course a low variability is preferable.

The EUL-method shows similar results compared to the CSD-method. The FACT approach shows the lowest inter-subject correlation and therefore the highest inter-subject variability. This can be explained by a much lower network density, as previously shown. As a consequence a lower number of samples (edges) can be included in the correlation calculation. Furthermore, a lower network density implicates a higher edge strength. Thus, a variability of an edge with higher strength has a higher influence on the correlation coefficient.

Furthermore, the resulting correlation coefficients show that group-wise studies are only meaningful with 83 and 129 brain regions. For a higher number of nodes the high inter-subject variability can become a limiting factor and may influence the statistical results. In addition, noise in the acquired data can overshadow differences in group studies at higher scales. However, the use of higher number of nodes increases the sensitivity and therefore allows to study the branching of one single bundle (figure 25). The use of a high number of nodes makes sense if one is interested in studying the structural connectivity in a single subject. In addition, it may be meaningful for multi-scale group studies. This means making a group-wise comparison between patient and controls in the lowest scale (83 regions). If an affected subnetwork can be found, a higher resolution can be taken to localize the pathology more precisely.

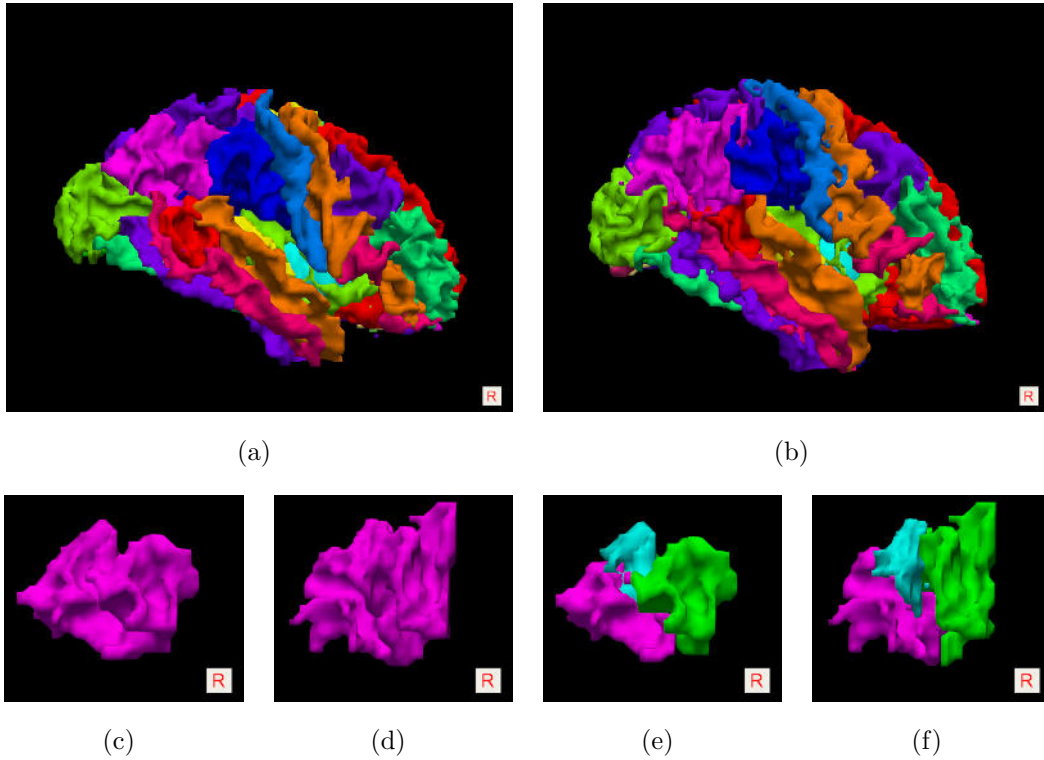


Figure 49: Biological fluctuations in brain size, shape and cortex folding structure between subject 1 (a) and subject 2 (b). Variation of the parcellated inferior parietal cortex of subject 1 and subject 2 for 83 (c) (d) and 129 brain regions (e) (f)

4.5. Anatomic Validation

In the previous section it was shown that the choice of tractography algorithm and diffusion weighted dataset has a major influence on network measures. On this account the choice of the “right” method becomes even more important for all kinds of structural connectivity studies. But what approach is the best in an anatomical reasonable way? In order to establish this we proposed a method to evaluate parts of the structural connectivity matrix. This method makes it possible to compare the information differences contained in the structural connectivity matrices using different approaches. The results are shown in this subsection.

4.5.1. Valid anatomic connections

In a first step, the quality of the reconstructed fiber bundles was evaluated for each tractography approach and dataset. In figure 50 the eight reconstructed white matter bundles which were taken for the evaluation process are shown.

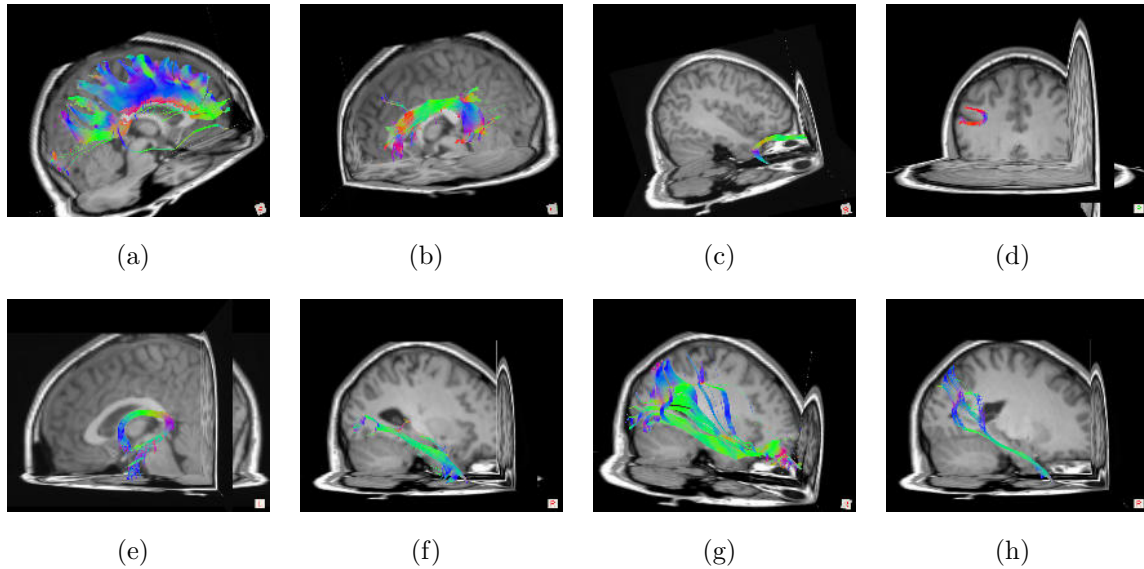


Figure 50: Reconstructed white matter bundles from dataset 8 of subject 1 using the CSD approach. Reconstructed Corpus Callosum (a), Superior Longitudinal Fasciculus (b), Uncinate Fasciculus (c), U-fiber (d), Fornix (e), Inferior Longitudinal Fasciculus (f), Inferior-fronto Occipital Fasciculus (g), Middle Longitudinal Fasciculus (h)

Each generated structural connectivity matrix was compared with the manually defined valid structural connectome matrix. The result is a new structural connectivity matrix containing only connections of those eight fiber bundles. This anatomic valid structural connectivity matrix is illustrated in figure 51 for three different approaches.

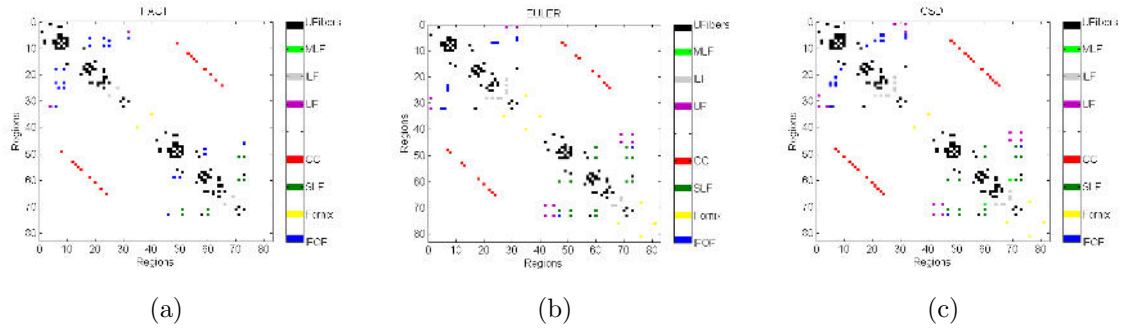


Figure 51: Valid connections in the structural connectome generated with the FACT approach (a), EUL approach (b) and CSD approach (c)

Afterwards the number of found connections in each valid structural connectivity matrix was counted. The results for subject 1 are illustrated in figure 52 and the results for subject 2 in figure 53.

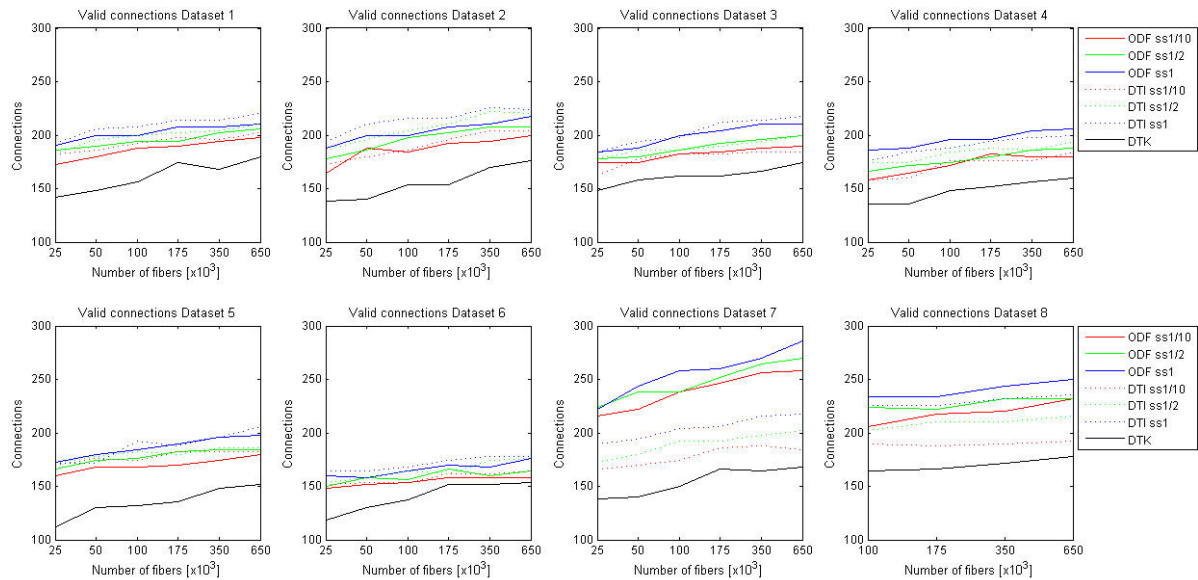


Figure 52: Number of valid anatomical connections in the structural connectivity matrices of subject 1 as a function of the fiber count and tractography method. Each subfigure represents the results of one dataset (for further acquisition details for each dataset see table 2). Note the different scales on the x-axis

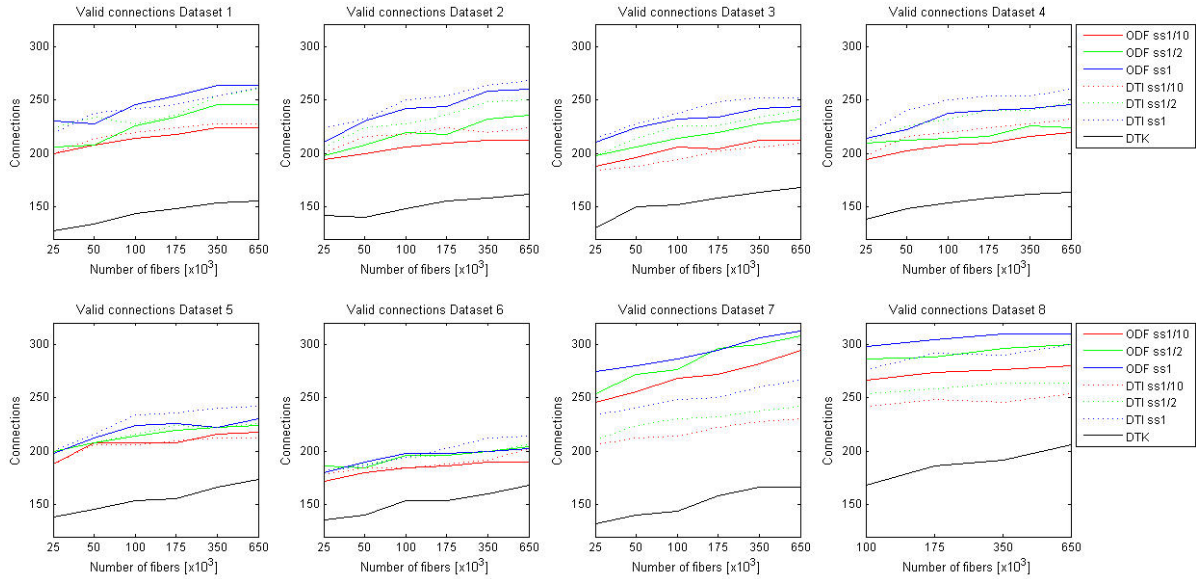


Figure 53: Number of valid anatomical connections in the structural connectivity matrices of subject 2 as a function of the fiber count and tractography method. Each subfigure represents the results of one dataset (for further acquisition details for each dataset see table 2). Note the different scales on the x-axis

Considerations in the first diagram (dataset 1) of both subjects show that about 30% more valid connections were reconstructed with the EUL and CSD approach than with the FACT approach. This is consistent with the findings in the network density. The differences in performance of the used tractography methods are clearly illustrated in figure 51. The U-fibers, which are the simplest and shortest fiber bundles, as well as the Corpus Callosum, which is also a very simple and dense fiber tract, were pretty well mapped with all three approaches. The first significant differences were found in the three highly curve-shaped bundles Fornix, Superior Longitudinal Fasciculus and Uncinate Fasciculus. The Fornix was successfully reconstructed with the EUL and CSD approach leading to 8 edges in the structural network, whereas only two edges are found in the network generated with the FACT approach. Furthermore, the SLF reconstructed with the CSD approach connects 14 pairs of cortical areas, the SLF reconstructed with the EUL approach connects 12 pairs of cortical areas and the SLF reconstructed with the FACT approach connects only 2 pairs of cortical areas. For the UF 14 edges were found in the structural networks reconstructed with the EUL or CSD-approach and only 8 edges were found using the FACT approach. The results of these three bundles show the weaknesses of the FACT approach. As this tractography algorithm uses a continu-

ously varying step size firstly an overshoot occurs in these highly curved regions leading to an inaccurate fiber trajectory and secondary the angle threshold condition is violated leading to an early termination.

The last three bundles which are the Inferior-fronto Occipital Fasciculus, the Middle Longitudinal Fasciculus and the Inferior Longitudinal Fasciculus are very long and complex bundles. On their path through the brain, they cross and kiss many other bundles and therefore they represent a great challenge for tractography approaches. The results in figure 51 shows that the CSD approach maps these bundles most precisely resulting in the most edges followed by the EUL approach and the FACT approach.

If a higher step size is used for tractography, the number of valid anatomic connections increases slightly. This again is due to the fact that the higher step size fans out the fibers near the gray-white matter boundary leading to more cortical connections. The biological fluctuations of the two subjects are also evident in the results. In subject 2 10% more fibers were found on average than in subject 1. However, the trends of valid connections are very consistent over both subjects.

Similar to the network measures the number of valid anatomic connections is very consistent over the first 3 datasets. A drop in valid connections of 15% can be observed looking from dataset 3 to dataset 6. Once again, this drop occurs due to the decreasing SNR in the acquired dataset. According to this low SNR only short tracts were reconstructed well. These short tracts make up more than 90% of the existing edges in the structural network mapped with dataset 6.

As shown in digram 7 in figure 53 the number of valid connections increases significantly by 25% using a complex tractography method in combination with 64 diffusion gradient directions. In contrast to the other DTI models, this model reconstructs kissing and crossing fibers and contains information in the structural connectivity which is absent in the structural connectivity networks mapped with the DTI approaches. On the basis of these findings the CSD-approach seems to be a powerful tool for studying the structural connectivity in human brains. These findings are in accordance with the findings in network density.

Furthermore, the number of anatomic connections increases by about 15% for all tractography approaches using a higher spatial dwMRI (dataset 8). Again, a higher spatial

resolution means a lower influence of partial volume effects and therefore a denser connectome. These high-resolution dw datasets can be powerful if one is interested in studying the structural connectivity of small or thin bundles in the human brain. However, it is important to note that the scanning time increases dramatically for these datasets, which can be a limiting factor in group-wise studies.

4.5.2. False positive connections

Each generated structural connectivity matrix was compared with the manually defined false positive matrix resulting in a new structural connectivity matrix containing only false positive connections. The number of these false positive connections was counted and the results for subject 1 are illustrated in figure 54 and the results for subject 2 in figure 55.

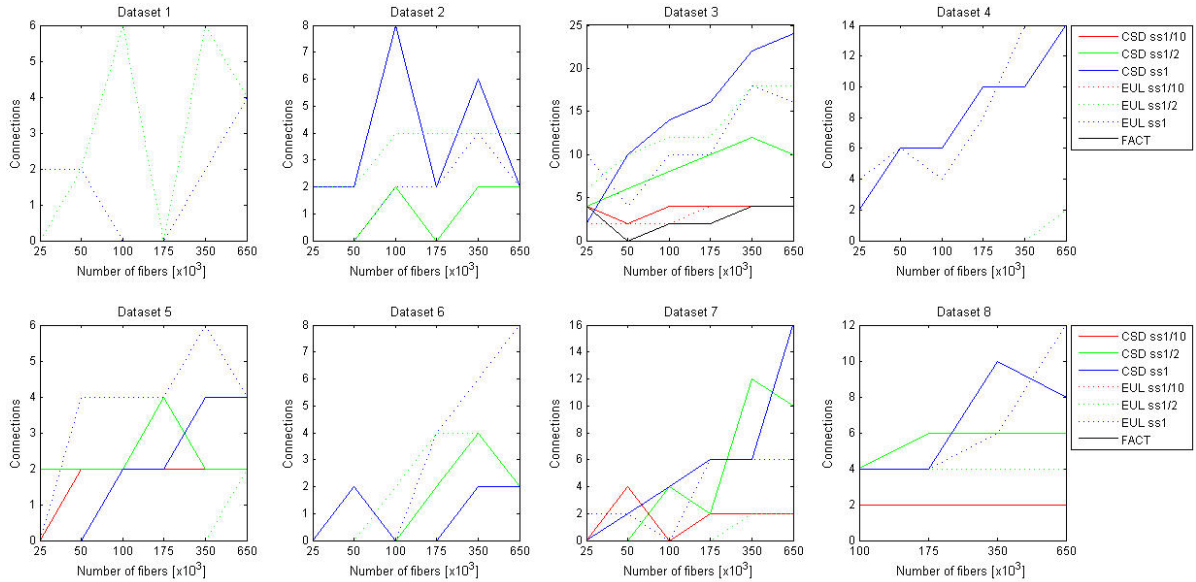


Figure 54: Number of false positive connections in the structural connectivity matrices of subject 1 as a function of the fiber count and tractography method. Each subfigure represents the results of one dataset (for further acquisition details for each dataset see table 2). Note the different scales on the y-axis.

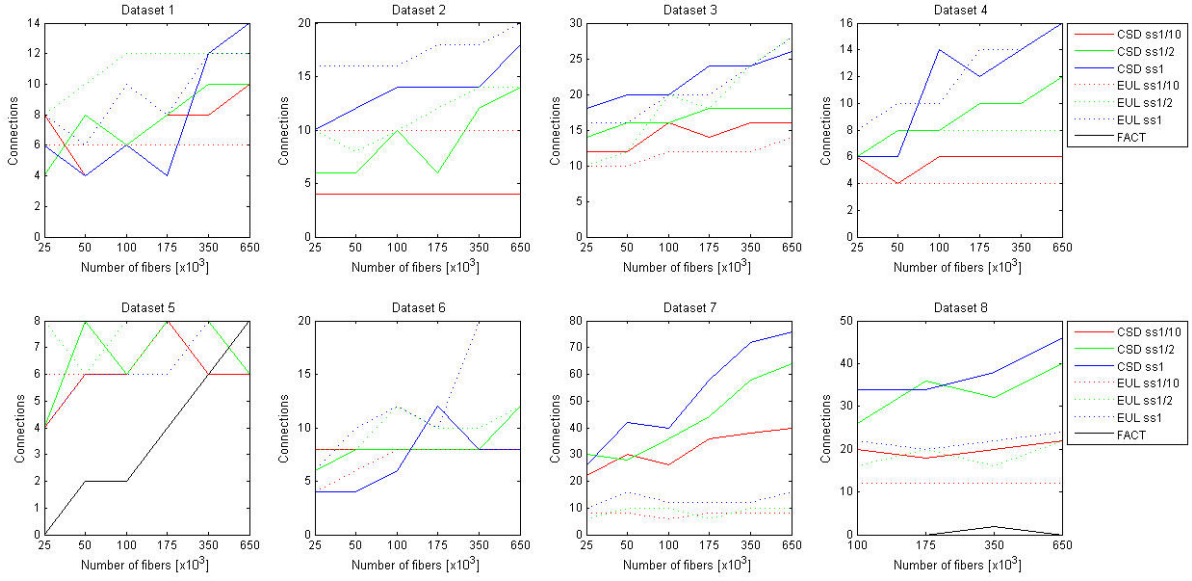


Figure 55: Number of false positive connections in the structural connectivity matrices of subject 2 as a function of the fiber count and tractography method. Each subfigure represents the results of one dataset (for further acquisition details for each dataset see table 2). Note the different scales on the y-axis

The first interesting observation in this analysis was that the number of false positive connections is much lower in structural connectivity matrices resulting from the FACT approach than in the structural networks resulting from the other two approaches. This demonstrates the strength of the FACT approach. Furthermore, an increase in the spatial resolution is accompanied by an increase in false positive connections for all methods. This has two reasons. The first reason is that the impact of diffusion noise is higher according to the lower voxel size. The second reason is that the fiber tracts cross much more voxels during the reconstruction process. Therefore, the chance to go astray is much higher. In all structural connectivity networks mapped with a higher step size an increase in false positive edges can be observed. It is important to note that an increase in step size leads to a higher branching of the white matter bundles, which on the one hand leads to a denser network but on the other hand increases the chance for an overshoot resulting in artificial edges. This is demonstrated in figure 56 using the example of the Unicate Fasciculus.

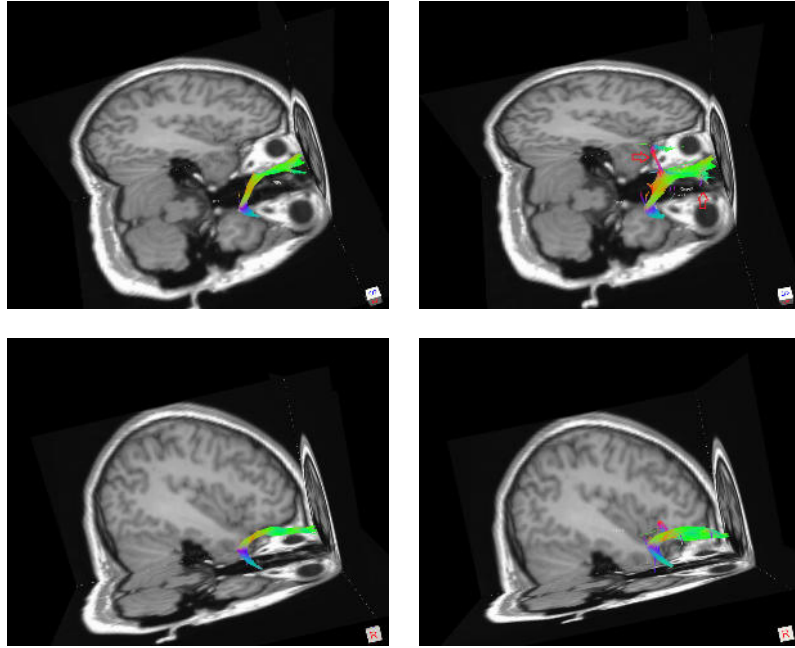


Figure 56: Influences of the step size demonstrated on the Unicate Fasciculus. Left row illustrates the Unicate Fasciculus reconstructed with the CSD approach using a step size of $1/10$ voxel length. The right row shows the Unicate Fasciculus reconstructed with the CSD approach using a step size of one voxel length. Red arrow indicates an artificially generated fiber occurring from an overshoot because of the high step size.

In addition, structural connectivity networks created from dataset 7 using a multi-direction approach (CSD) contains much more false positive edges than structural networks created from single-direction approaches (DTI). In multi-direction models the trajectories can go two or more ways within a voxel. The trajectory is determined by using the closest direction to the current direction, which can result in the choice of a wrong branch which is illustrated in figure 57.

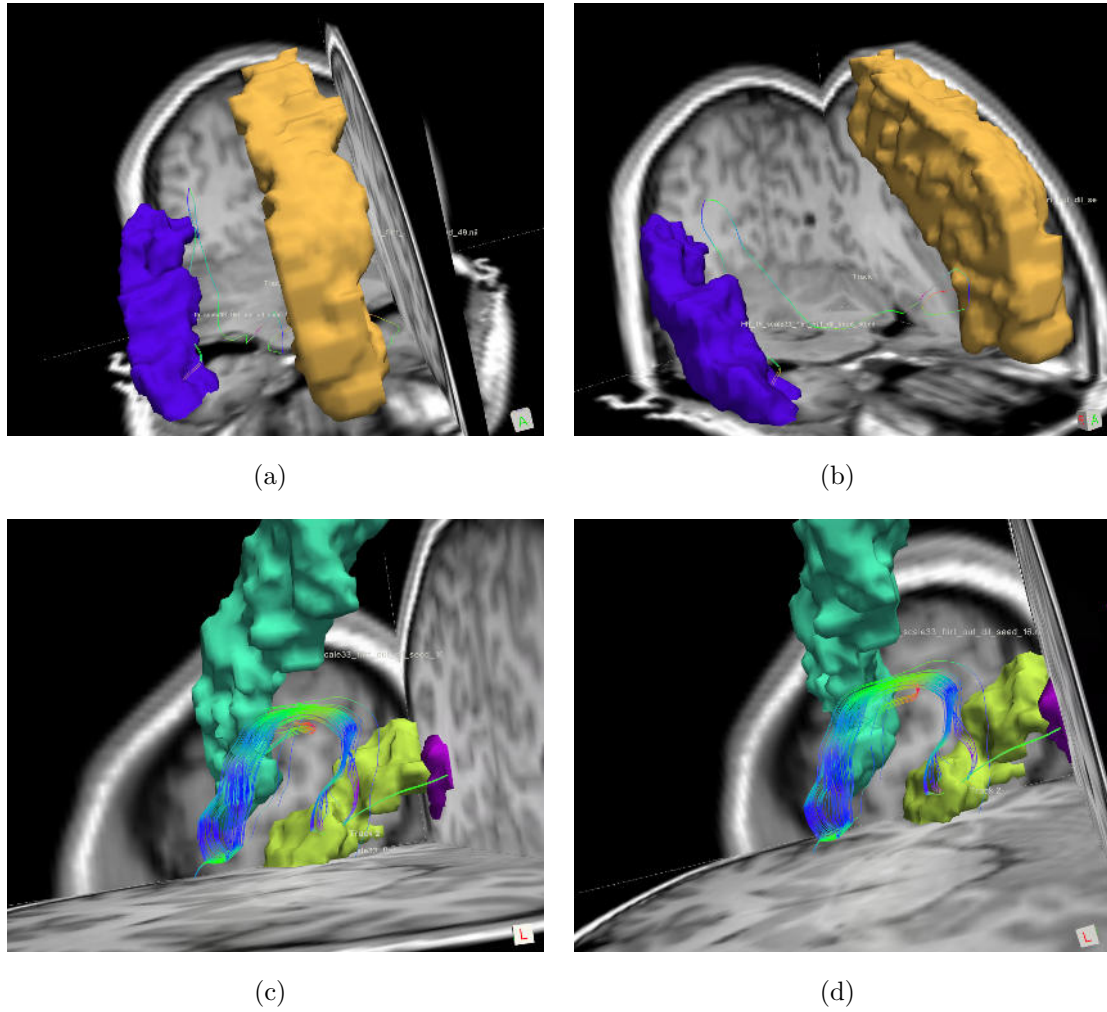


Figure 57: Artificially generated fibers from the CSD approach using a spherical harmonic model of order eight (dataset 7)

This evaluation of information contained in the structural connectivity network shows once again that no “best mapping method” exists. On the one hand using higher complex models in combination with a high number of diffusion gradient directions allows the reconstruction of complex fiber bundles, which are absent in simple DTI approaches. But on the other hand the number of false positive connections increases dramatically due to the complexity of the model. Therefore, a strategy of estimating and eliminating such false positive connections is necessary if one uses this type of combination for group-wise studies. Otherwise, these wrong connections can pretend differences in these groups which do not exist in the human brain. The same can be noticed for structural connectivity networks mapped from high-resolution diffusion weighted datasets.

Furthermore, the analysis shows that the FACT approach estimates the least number of false positive connections, which is preferable for structural connectivity studies. However, this should be interpreted with care, because many connections, especially long complex connections, are absent in these structural connectivity matrices. Therefore, pathologies which may exist in these complex bundles may not be recognized.

5. Conclusion

The aim of this thesis was to investigate the impacts of network indices derived from the human structural brain network and four research questions should be answered.

(1) How do different DWI acquisition schemes influence the structural connectivity and network measures? (2) How does the number of nodes influence the results of structural connectivity? (3) Has the fiber tracing algorithm and the number of reconstructed fibers an impact on the structural connectivity and on network measures? (4) Which combinations of the used methods are most robust and reproducible? For these investigations structural connectivity maps were generated from dwMRI datasets acquired from two healthy subjects. The network indices were calculated from the weighted structural connectivity matrices.

In a first step, the influence of different tractography approaches and their settings was analyzed. It was shown that the choice of the tractography method in combination with different step size settings has a great influence on the structural connectivity network and the corresponding network measures. The major impact was determined on the network density. It is already known from previous studies that the network density strongly affects network indices and these effects were confirmed in this thesis. Structural connectivity networks generated with the FACT algorithm show the lowest density and average nodal degree but the highest efficiency. The networks generated using the multiple fiber direction model (CSD-approach) show the highest density and nodal degree but the lowest efficiency. The network indices derived from the structural connectivity matrices that were generated using the EUL-approach are between them. In general, an increase in step size led to a denser but less efficient structural network.

In a second step, the impacts of different diffusion MRI acquisition schemes on the structural connectivity networks were investigated. An increase in spatial resolution from $2 \times 2 \times 3 \text{mm}^3$ to 1.5mm isotropic resulted in a denser (5%) but less efficient structural

connectome. Increasing gradient directions from 12 to 64 showed no variation in network measures for the two DTI approaches but a severe change for the ODF approach. The density increased by 20% for the structural connectomes. Furthermore, the networks generated with DTI approaches were more efficient than networks generated with the ODF approach.

In order to analyse the information content in the structural connectivity networks resulting from different combinations of tractography algorithms and dwMRI a “valid” structural connectivity matrix was introduced. This “valid” matrix contains anatomical edges of 8 well known white matter bundles. The analyses showed that the structural networks derived from the two single-direction tractography approaches (EUL and FACT) generally contain less valid connections than the multi-direction tractography approach. However, the CSD-approach generated more false positive connections than the two other approaches. An increase in spatial resolution of the dw MRI led to a more precise reconstruction of white matter bundles especially of thin bundles. As a result the structural connectome was denser with an increase of 15% in valid connections.

Furthermore, the impact of fiber count used for tractography was investigated. Our investigations revealed an increase of 4% in network density and nodal degree when increasing the fiber count from 25 000 to 650 000 whereas the global efficiency remained constant. In order to obtain an anatomical structural network, which means that every brain region is at least connected with one other brain region, at least 100 000 fibers were necessary.

To study similarities and differences in the structural connectivity of the human brain it is essential that the methods are robust and the results are reproducible. Therefore, the intra-subject as well as the inter-subject variability of the raw connectivity matrices was evaluated for each used method. In general all methods used are robust and the results were reproducible. The lowest inter-subject and intra-subject variability was found between structural connectivity matrices generated from high-resolution diffusion weighted datasets. The two DTI based approaches show a lower intra-subject variability than the complex ODF based approach but a higher inter-subject variability, because crossing and kissing fibers cannot be traced.

In a last step, the influence of the number of nodes on the structural connectivity networks was investigated. Increasing the nodes resulted in a sparser structural connectome with a density of 4% at highest parcellation scale (1015 nodes). Thus, the number of

nodes has the greatest influence on the structural connectivity network of all investigated methods. Furthermore, the intra-subject as well as the inter-subject variability increased with the number of nodes. The higher number of nodes allows to study the branching of a white matter bundle in the human brain but due to the significantly higher variability it is not well suited for group-wise studies. However, in combination with lower resolution it may be powerful for assessing pathologies in cortical areas or white matter bundles.

In summary, this thesis demonstrated that structural connectivity networks of the human brain are highly sensitive to different acquisition and parcellation schemes as well as tractographic algorithms. Therefore, care should be taken when comparing network indices between studies. A comparison must always be done with reference to the nodal scale and density of the networks. Furthermore, the findings of this thesis indicate that at present neither a “best mapping approach” nor a “superior dwMRI scheme” exists. Each combination of dwMRI, tractography algorithm and parcellation scheme has to be carefully and individually chosen according to the type of the connectivity study. If the main interest is in studying long complex bundles, the CSD approach in combination with a high number of gradient directions is preferable. The high resolution dwMRI is more suitable for studying thin bundles in the structural network of the human brain. In group-wise studies the high-resolution dwMRI in combination with the CSD approach will deliver the best results, but the scan time increases dramatically from 5 min to 30 min, rendering clinical usage virtually impossible. For studying neurological diseases the FACT approach in combination with conventional DTI acquisition is recommended because of its high reproducibility. The investigations showed that the higher nodal scale makes sense in a multi-scale approach for assessing the location of the pathology step by step by increasing the number of nodes.

References

- [1] Zalesky A, Fornito A, Harding IH, Cocchi L, Yücel M, Pantelis C, and Bullmore ET. Whole-brain anatomical networks: does the choice of nodes matter? *Neuroimage*, 50(3):970–983, 2010.
- [2] Andrew L. Alexander, Jee Eun Lee, Mariana Lazar, and Aaron S. Field. Diffusion tensor imaging of the brain. *Neurotherapeutics*, 4:316–329, July 2007.
- [3] X. An, R. Bandler, D. Öngür, and J.L. Price. Prefrontal cortical projections to longitudinal columns in the midbrain periaqueductal gray in macaque monkeys. *Journal of Comparative Neurology*, 401:455–479, 1989.
- [4] J. L. Andersson and S. Skare. Image distortion and its correction in diffusion mri. *Diffusion MRI: Theory, Methods, and Applications*, pages 285–302, 2010.
- [5] Antranik. Cerebral white matter and gray matter and basal ganglia. *Anatomy, Science*, 2011.
- [6] Fischl B, Salat DH, Busa E, Albert M, Dieterich M, Haselgrove C, van der Kouwe A, Killiany R, Kennedy D, Klaveness S, Montillo A, Makris N, Rosen B, and Dale AM. Whole brain segmentation: Automated labeling of neuroanatomical structures in the human brain. *Neuron*, 33:341–355, 2002.
- [7] Fischl B, van der Kouwe A, Destrieux C, Halgren E, Segonne F, Salat DH, Busa E, Seidman LJ, Goldstein J, Kennedy D, Caviness V, Makris N, Rosen B, and Dale AM. Automatically parcellating the human cerebral cortex. *Cerebral Cortex*, 14(1):11–22, 2004.
- [8] Danielle S. Bassett, Jesse A. Brown, Vibhas Deshpande, Jean M. Carlson, and Scott T. Grafton. Conserved and variable architecture of human white matter connectivity. *NeuroImage*, 54:1262–1279, 2011.
- [9] Subhash Chandra Bhatnagar. Neuroscience for the study of communicative disorders. *Lippincott Williams and Wilki*, 4, 2012.
- [10] Westin C.-F, Maier S.E, Mamata H, Nabavi A, Jolesz F.A, and Kikinis R. Processing and visualization for diffusion tensor mri. *Medical Image Analysis*, 6:93–108, 5 July 2001.
- [11] William Wesley Campbell and Russell N. DeJong. Dejong’s the neurologic examination, teil 327. *Lippincott Williams and Wilkins*, 2005.
- [12] Marco Catani and Michel Thiebaut de Schotten. A diffusion tensor imaging tractography atlas for virtual in vivo dissections. *Cortex*, 44:1105–32, 2008.
- [13] Marco Catani and Michel Thiebaut de Schotten. Atlas of human brain connections. *Oxford University Press*, 2012.

- [14] Marco Catania and Marsel Mesulam. The arcuate fasciculus and the disconnection theme in language and aphasia: History and current state. *Cortex*, 44:953–961, 2008.
- [15] Thomas E. Conturo, Nicolas F. Lori, Thomas S. Cull, Erbil Akbudak, Abraham Z. Snyder, Joshua S. Shimony, Robert C. McKinstry, Harold Burton, and Marcus E. Raichle. Tracking neuronal fiber pathways in the living human brain. *Proceedings of the National Academy of Sciences of the United States of America*, 96(18):10422–10427, 1999.
- [16] R. Cameron Craddock, Saad Jbabdi, Chao-Gan Yan, Joshua Vogelstein, F. Xavier Castellanos, Adriana Di Martino, Clare Kelly, Keith Heberlein, Stan Colcombe, and Michael P. Milham. Imaging human connectomes at the macroscale. *Nat Methods*, 10(6):524–539, 2013.
- [17] Zaixu Cui, Suyu Zhong, Pengfei Xu, Yong He, and Gaolang Gong. Panda: a pipeline toolbox for analyzing brain diffusion images. *Front Hum Neurosci.*, 7:42, 2013.
- [18] Goldberg-Zimring D, Mewes AUJ, Maddah M, and Warfield SK. Diffusion tensor magnetic resonance imaging in multiple sclerosis. *J Neuroimagine*, 15:68S–81S, 2005.
- [19] Alessandro Daducci, Stephan Gerhard, Alessandra Griffa, Alia Lemkaddem, Leila Cammoun, Xavier Gigandet, Reto Meuli, Patric Hagmann, and Jean-Philippe Thiran. The connectome mapper: An open-source processing pipeline to map connectomes with mri. *PLoS ONE*, 7(12):e48121, 2012.
- [20] Anders M. Dale, Bruce Fischl, and Martin I. Sereno. Cortical surface-based analysis i. segmentation and surface reconstruction. *NeuroImage*, 9:179–194, 1999.
- [21] PhD Goldberg-Zimring Daniel, MD Mewes Andrea A. J., MSc Maddah Mahnaz, and PhD Warfield Simon K. Diffusion tensor magnetic resonance imaging in multiple sclerosis. *J Neuroimaging*, 15:68S–81S, 2005.
- [22] Nicolas Menjot de Champfleura, Igor Lima Maldonadoa, Sylvie Moritz-Gassera, Paolo Machia, Emmanuelle Le Barsa, Alain Bonafea, and Hugues Duffaua. Middle longitudinal fasciculus delineation within language pathways: A diffusion tensor imaging study in human. *European Journal of Radiology*, 88:151–157, 2013.
- [23] Rahul S. Desikan, Florent Segonne, Bruce Fischl, Brian T. Quinn, Bradford C. Dickerson, Deborah Blacker, Randy L. Buckner, Anders M. Dale, R. Paul Maguire, Bradley T. Hyman, Marilyn S. Albert, and Ronald J. Killiany. An automated labeling system for subdividing the human cerebral cortex on mri scans into gyral based regions of interest. *NeuroImage*, 31:968–980, 2006.
- [24] Jones DK, Knösche TR, and Turner R. White matter integrity, fiber count, and other fallacies: the do’s and don’ts of diffusion mri. *Neuroimag*, 73:239–254, 2013.

- [25] Bassett DS, Brown JA, Deshpande V, Carlson JM, and Grafton ST. Conserved and variable architecture of human white matter connectivity. *Neuroimage*, 54(2):1262–1279, 2011.
- [26] Ross ED. Sensory-specific amnesia and hypoemotionality in humans and monkeys: gateway for developing a hodology of memory. *Cortex*, 44:1010–22, 2008.
- [27] Yeterian EH, Pandya DN, Tomaiuolo F, and Petrides M. The cortical connectivity of the prefrontal cortex in the monkey brain. *Cortex*, 48:58–81, 2012.
- [28] Latini F. New insights in the limbic modulation of visual inputs: The role of the inferior longitudinal fasciculus and the li-am bundle. *Neurosurgical Review*, 38:179–189, 2015.
- [29] Juan C. Fernandez-Miranda, Yibao Wang, Sudhir Pathak, Lucia Stefaneau, Timothy Verstynen, and Fang-Cheng Yeh. Asymmetry, connectivity, and segmentation of the arcuate fascicle in the human brain. *Brain structure and function*, 2014.
- [30] Parker GJ. Analysis of mr diffusion weighted images. *The British Journal of Radiology*, 77:S176–S185, 2004.
- [31] William R. Gray, John A. Bogovic, Joshua T. Vogelstein, Bennett A. Landman, Jerry L. Prince, and R. Jacob Vogelstein. Magnetic resonance connectome automated pipeline. *Arxiv preprint arXiv:1111.2660*, page 5, 2011.
- [32] Patric Hagmann, Leila Cammoun, Xavier Gigandet, Reto Meuli, Christopher J Honey, Van J Wedeen, and Olaf Sporns. Mapping the structural core of human cerebral cortex. *PLoS computational biology*, 6:e159, 2008.
- [33] Hahn H.K. and Peitgen H.-O. The skull stripping problem in mri solved by a single 3d watershed transform. *MICCAI 2000*, pages 134–143, 2000.
- [34] Tournier JD, Calamante F, and Connelly A. Robust determination of the fibre orientation distribution in diffusion mri: non-negativity constrained super-resolved spherical deconvolution. *Neuroimage*, 35(4):1459–1472, 2007.
- [35] Tournier JD, Calamante F, and Connelly A. Mrtrix: diffusion tractography in crossing fibre regions. *International Journal of Imaging Systems and Technology*, page DOI: 10.1002/ima.22005, 2012.
- [36] Tournier JD, Calamante F, Gadian DG, and Connelly A. Direct estimation of the fiber orientation density function from diffusion-weighted mri data using spherical deconvolution. *Neuroimage*, 23(3):1176–1185, 2004.
- [37] M. Jenkinson, P.R. Bannister, J.M. Brady, and S.M. Smith. Improved optimisation for the robust and accurate linear registration and motion correction of brain images. *NeuroImage*, 17(2):825–841, 2002.
- [38] M. Jenkinson and S.M. Smith. A global optimisation method for robust affine registration of brain images. *Medical Image Analysis*, 5(2):143–156, 2001.

- [39] B. Jeurissen, A. Leemans, J-D. Tournier, D. K. Jones, and J. Sijbers. Estimating the number of fiber orientations in diffusion mri voxels: a constrained spherical deconvolution study. *Processing of the International Society for Magnetic Resonance in Medicine, Stockholm, Sweden,,* pp.573, 2010.
- [40] B. Jeurissen, A. Leemans, J-D. Tournier, and J. Sijbers. Estimation of uncertainty in constrained spherical deconvolution fiber orientations. *IEEE*, 5:907–910, 2008.
- [41] White JG, Southgate E, Thomson JN, and Brenner S. The structure of the nervous system of the nematode *caenorhabditis elegans*. *Philos Trans R Soc Lond B Biol Sc*, 314:1–340, 1986.
- [42] Hangyi Jiang, Peter C.M. van Zijl, Jinsuh Kim, Godfrey D. Pearlson, and Susumu Mori. Dtistudio: Resource program for diffusion tensor computation and fiber bundle tracking. *Computer Methods and Programs in Biomedicine*, 81:106–116, 2006.
- [43] Marcus Kaiser. A tutorial in connectome analysis:topological and spatial features of brain networks. *NeuroImage*, 57:892–907, 2011.
- [44] PETER B. KINGSLEY. Introduction to diffusion tensor imaging mathematics: Part iii. tensor calculation, noise, simulations, and optimization. *Concepts in Magnetic Resonance Part A*, 28A(2):155–179, 2006.
- [45] Hayworth KJ, Morgan JL, Schalek R, Berger DR, Hildebrand DG, and Lichtman JW2. maging atum ultrathin section libraries with wafermapper: a multi-scale approach to em reconstruction of neural circuits. *Front Neural Circuits*, 8:68, 2014.
- [46] Cammoun L, Gigandet X, Meskaldji D, Thiran JP, Sporns O, Do KQ, Maeder P, Meuli R, and Hagmann P. Mapping the human connectome at multiple scales with diffusion spectrum mri. *Journal of neuroscience methods*, 203(2):386–97, 2012.
- [47] Xiaozheng Liu, Wei Liu, Guang Yang, Weidong Chen, Junming Zhu, Yongdi Zhou, Bradley S. Peterson, and Dongrong Xu. A locally linear least squares method for simultaneously smoothing dwi data and estimating diffusion tensors. *Journal of Medical and Biological Engineering*, 33:3, 2013.
- [48] Varshney LR, Chen BL, Paniagua E, Hall DH, and Chklovskii DB. Structural properties of the *caenorhabditis elegans* neuronal network. *PLoS Computational Biology*, 7:e1001066, 2011.
- [49] Bastiani M, Shah NJ, Goebel R, and Roebroeck A. Human cortical connectome reconstruction from diffusion weighted mri: the effect of tractography algorithm. *Neuroimage*, 62(3):1732–49, 2012.
- [50] Catani M, Dellacqua F, and Thiebaut de Schotten M. A revised limbic system model for memory, emotion and behaviour. *Neuroscience and Biobehavioral Reviews*, 37:1724–1737, 2013.

- [51] Descoteaux M, Angelino E, Fitzgibbons S, and Deriche R. Apparent diffusion coefficients from high angular resolution diffusion imaging: estimation and applications. *Magnetic Resonance in Medicine*, 56(2):395–410, 2006.
- [52] Juan Martino, Christian Brogna, Santiago G. Robles, Francesco Vergani, , and Hugues Duffau. Anatomic dissection of the inferior fronto-occipital fasciculus revisited in the lights of brain stimulation data. *Cortex*, 46:691–699, 2010.
- [53] Juan Martino, Philip C. De Witt Hamer, Francesco Vergani, Christian Brogna, Enrique Marco de Lucas, Alfonso Vazquez-Barquero, Juan A. Garcia-Porrero, and Hugues Duffau. Cortex-sparing fiber dissection: an improved method for the study of white matter anatomy in the human brain. *Journal of Anatomy*, 219:531–541, 2011.
- [54] Marco Catani MD, Derek K. Jones PhD, and Dominic H. ffytche MD. Perisylvian language networks of the human brain. *Ann Neurol*, 57:8–16, 2005.
- [55] Susumu Mori and Peter B. Barker. Diffusion magnetic resonance imaging: Its principle and applications. *The Anatomical Record*, 257:102–109, 1999.
- [56] Makris N, Papadimitriou GM, Kaiser JR, Sorg S, Kennedy DN, and Pandya DN. Delineation of the middle longitudinal fascicle in humans: A quantitative, in vivo, dt-mri study. *Cerebral Cortex*, 19:777–785, 2009.
- [57] Sporns O, Tononi G, and Kötter R. The human connectome: A structural description of the human brain. *PLoS computational biology*, 1:e42, 2005.
- [58] Rodrigues P, Prats-Galino A, Gallardo-Pujol D, Villoslada P, Falcon C, and Prckovska V. Evaluating structural connectomics in relation to different q-space sampling techniques. *Med Image Comput Comput Assist Interv*, 16(1):671–678, 2013.
- [59] Hagmann Patric. From diffusion mri to brain connectomics. *Dissertation*, 2005.
- [60] Jean Philibert. One and a half century of diffusion: Fick, einstein, before and beyond. *Diffusion-fundamentals*, 4, 2005.
- [61] Wang R, Benner T, Sorensen AG, and Wedeen VJ. Diffusion toolkit: A software package for diffusion imaging data processing and tractography. *Proc. Intl. Soc. Mag. Reson. Med.*, 15:3720, 2007.
- [62] William Gray Roncal, Zachary H. Koterba, Disa Mhembere, Dean M. Kleissas, Joshua T. Vogelstein, Randal Burns, Anita R. Bowles, Dimitrios K. Donavos, Sephira Ryman, Rex E. Jung, Lei Wu, Vince Calhoun, and R. Jacob Vogelstein. Migraine: Mri graph reliability analysis and inference for connectomics. *IEEE Global Conference on Signal and Information Processing, IEEE*, 2013.
- [63] Mikail Rubinov and Olaf Sporns. Complex network measures of brain connectivity: Uses and interpretations. *NeuroImage*, 52:1059–1069, 2010.

- [64] Epelbaum S, Pinel P, Gaillard R, Delmaire C, Perrin M, Dupont S, Dehaene S, and Cohen L. Pure alexia as a disconnection syndrome: new diffusion imaging evidence for an old concept. *Cortex*, 44:962–974, 2008.
- [65] Mori S1, Crain BJ, Chacko VP, and van Zijl PC. Three-dimensional tracking of axonal projections in the brain by magnetic resonance imaging. *Annals of Neurology*, 45:265–269, 1999.
- [66] F. Segonne, A.M. Dale, E. Busa, M. Glessner, D. Salat, H.K. Hahn, and B. Fischl. A hybrid approach to the skull stripping problem in mri. *NeuroImage*, 22:1060–1075, 2004.
- [67] Sebastian Seung. Das konnektom: Erklärt der schaltplan des gehirns unser ich? *SpringerSpektrum*, 2013.
- [68] Sarubbo Silvio, De Benedictis Alessandro, Maldonado Igor L., Basso Gianpaolo, and Duffau Hugues. Frontal terminations for the inferior fronto-occipital fascicle: anatomical dissection, dti study and functional considerations on a multi-component bundle. *Brain structure and function*, 218:21–37, 2013.
- [69] J. G. Sled, A. P. Zijdenbos, and A. C. Evans. A non-parametric method for automatic correction of intensity non-uniformity in mri data. *IEEE Transactions on Medical Imaging*, 17:87–97, 1998.
- [70] Peter-Pike Sloan. Stupid spherical harmonics (sh) tricks. *Microsoft Corporation*, 2008.
- [71] Talairach and Tournoux. Co-planar stereotaxic atlas of the human brain. *Thieme Medical Publishers, New York*, 1988.
- [72] S. C. Turaga, J. F. Murray, V. Jain, F. Roth, M. Helmstaedter, K. Briggman, W. Denk, and H. S. Seung. Convolutional networks can learn to generate affinity graphs for image segmentation. *Neural Computation*, 22:511–538, 2010.
- [73] S. van de Geer. Least squares estimation. *Encyclopedia Statistics in The Behavioral Sciences*, 2:1041–1045, 2005.
- [74] Zhang Y, Zhang J, Oishi K, Faria AV, Jiang H, Li X, Akhter K, Rosa-Neto P, Pike GB, Evans A, Toga AW, Woods R, Mazziotta JC, Miller MI, van Zijl PC, and Mori S. Atlas-guided tract reconstruction for automated and comprehensive examination of the white matter anatomy. *Neuroimage*, 52:1289–1301, 2010.
- [75] Paul A. Young, Paul Henry Young, and Daniel Lee Tolbert. Basic clinical neuroscience. *Lippincott Williams and Wilkins*, 2008.

Appendices

A. White matter pathways and the corresponding cortical areas in Freesurfer

Table 5: Three primary fiber bundles of the superior longitudinal fasciculus and the connected cortical areas. The number in the bracket characterize the cortical-region in the left hemisphere of the Desikan-Killiany atlas

Fiber tract	Cortical Area1	Cortical Area2
Posterior indirect fiber tract	Posterior middle temporal gyrus(71)	Angular gyrus (60)
	Superior temporal gyrus(73)	Angular gyrus(60)
Anterior indirect fiber tract	Inferior parietal cortex(60)	inferior frontal gyrus(43,46,47)
	Inferior parietal cortex(60)	Ventral precentral gyrus(51)
Supplementary Long direct fiber tract	Inferior temporal gyrus(70)	Ventral precentral gyrus(51)
	Inferior temporal gyrus(70)	Caudal middle gyrus(50)
	Inferior temporal gyrus(70)	Pars triangularis(46)
	Middle temporal gyrus(71)	Ventral precentral gyrus(51)
	Middle temporal gyrus(71)	Caudal middle gyrus(50)
	Middle temporal gyrus(71)	Pars triangularis(46)
Primary Long direct fiber tract	Middle temporal gyrus(71)	Ventral precentral gyrus(51)
	Middle temporal gyrus(71)	Pars opercularis(47)
	Superior temporal gyrus(73)	Ventral precentral gyrus(51)
	Superior temporal gyrus(73)	Pars opercularis(47)

Table 6: The connected cortical areas of the Uncinate Fasciculus. The first number in the bracket characterize the cortical-region in the right hemisphere and the second number the cortical-region in the left hemisphere of the Desikan-Killiany atlas

Cortical Area1	Cortical Area2
Temporal Pole(28,69)	Medial orbitofrontal cortex(4,45)
	Lateral orbitofrontal cortex(1,42)
Anterior portion of the superior temporal gyri (32,73)	Medial orbitofrontal cortex(4,45)
	Lateral orbitofrontal cortex(1,42)
Anterior portion of the middle temporal gyri (30,71)	Medial orbitofrontal cortex(4,45)
	Lateral orbitofrontal cortex(1,42)

Table 7: The connected cortical areas of the Inferior fronto-occipital fasciculus. The first number in the bracket characterizes the cortical-region in the right hemisphere and the second number the cortical-region in the left hemisphere of the Desikan-Killiany atlas

Component	Cortical Area1	Cortical Area2
superficial and dorsal subcomponent	Pars Triangularis(5,46)	Superior parietal lobule(18,59)
		occipital extrastriate cortex (21,23,24,62,64,65)
		Superior temporal gyrus (32,73)
		Fusa (25,66)
	Pars Opercularis(6,47)	Superior parietal lobule(18,59)
		occipital extrastriate cortex (21,23,24,62,64,65)
		Superior temporal gyrus (32,73)
		Fusa (25,66)
Posterior Component	Middle frontal gyrus(7,9,48,50)	Superior parietal lobule(18,59)
		occipital extrastriate cortex (21,23,24,62,64,65)
	Dorsolateral-prefrontal cortex(6,7)	Fusa (25,66)
		Superior parietal lobule(18,59)
Middle Component	Superior parietal lobule(18,59)	occipital extrastriate cortex (21,23,24,62,64,65)
		Fusa (25,66)
Middle Component	Superior parietal lobule(18,59)	middle frontal gyrus(7,9,48,50)
		lateral orbitofrontal cortex(1,42)
Anterior Component	Basal orbito-frontal cortex(4,45)	Fusa (25,66)
		occipital extrastriate cortex (21,23,24,62,64,65)

Table 8: The connected cortical areas of the Inferior Longitudinal Fasciculus. The first number in the bracket characterize the cortical-region in the right hemisphere and the second number the cortical-region in the left hemisphere of the Desikan-Killiany atlas

Component	Cortical Area1	Cortical Area2
dorsal component	Lateral occipital cortex(23,64)	Temporal pole(28,69)
	Medial cuneal cortex(21,62)	Temporal pole(28,69)
ventral component	Posterior fusiform area(25,66)	Temporal pole(28,69)
	parahippocampal gyrus(26,67)	Temporal pole(28,69)
Li-Am component	Mesial posterior lingual cortex(24,65)	Amygdala(41,82)

Table 9: The cortical areas connected by the short association fasciculus. The first number in the bracket characterize the cortical-region in the right hemisphere and the second number the cortical-region in the left hemisphere of the Desikan-Killiany atlas

Cortical Area1	Cortical Area2
superior parietal gyrus(18,59)	Postcentraler gyrus(16,57)
	Angular gyrus(19,60)
	Pre-cuneus(20,61)
	Superior occipital gyrus(23,64)
	Middle occipital gyrus(23,64)
	Supramarginal gyrus(17,58)
Cingulate gyrus(15,56)	Pre-cuneus(20,61)
	Superior frontal gyrus(8,49)
Superior frontal gyrus(8,49)	Precentral gyrus(10,51)
	Inferior frontal gyrus(2,5,6,43,46,47)
	Middle frontal gyrus(7,9,48,50)
Middle frontal gyrus(7,9,48,50)	Inferior frontal gyrus(2,5,6,43,46,47)
	Precentral gyrus(10,51)
Inferior frontal gyrus(2,5,6,43,46,47)	Precentral gyrus(10,51)
Precentraler gyrus(10,51)	Postcentraler gyrus(16,57)
Postcentraler gyrus(16,57)	Supramarginal gyrus(17,58)
Angular gyrus(19,60)	Middle occipital gyrus(23,64)
	Supramarginal gyrus(17,58)
Cuneus(21,62)	Lingual gyrus(24,65)
	Superior occipital gyrus(23,64)
	Middle occipital gyrus(23,64)
Fusiform gyrus(25,66)	Inferior occipital gyrus(22,63)
	Middle occipital gyrus(23,64)
Superior occipital gyrus(23,64)	Middle occipital gyrus(23,64)
Inferior occipital gyrus(22,63)	Middle occipital gyrus(23,64)
Superior temporal gyrus(32,73)	Middle temporal gyrus(30,71)
	Supramarginal gyrus(17,58)
Inferior temporal gyrus(29,70)	Middle temporal gyrus(30,71)
Lateral fronto-orbital gyrus(1,42)	Middle fronto-orbital gyrus(4,45)

Table 10: The cortical areas connected by the Fornix. The first number in the bracket characterize the cortical-region in the right hemisphere and the second number the cortical-region in the left hemisphere of the Desikan-Killiany atlas

Cortical Area 1	Cortical Area 2
Hippocampus(40,81)	Mammillary body (35,76)
	Hypothalamus (not labeled)
	Anterior thalamic nucleus (35,76)
Entorhinaler cortex(27,68)	Mammillary body (35,76)
	Hypothalamus (not labeled)
	Anterior thalamic nucleus (35,76)

Table 11: The cortical areas connected by the Middle Longitudinal Fasciculus (MLF). The first number in the bracket characterize the cortical-region in the right hemisphere and the second number the cortical-region in the left hemisphere of the Desikan-Killiany atlas

Cortical Area 1	Cortical Area 2
Temporal pole (28,69)	Angular Gyrus (19,69)

Table 12: Cortical areas of the left and right hemisphere connected by the corpus callosum. The number in the bracket characterize the cortical-region in the Desikan-Killiany atlas

Cortical Area left hemisphere	Cortical Area right hemisphere
superior parietal gyrus(59)	superior parietal gyrus(18)
cingulate gyrus(53-56)	cingulate gyrus(12-15)
superior frontal gyrus(49)	superior frontal gyrus(8)
medial frontal gyrus(48,50)	medial frontal gyrus(7,9)
precentral gyrus(51)	precentral gyrus(10)
postcentral gyrus(57)	postcentral gyrus(16)
pre-cuneus(61)	pre-cuneus(20)
cuneus(62)	cuneus(21)
lingual gyrus(65)	lingual gyrus(24)
superior occipital gyrus(62)	superior occipital gyrus(21)
medial occipital gyrus(64)	medial occipital gyrus(23)